

Diss. ETH No. 13128

MAGNETIC CORRELATIONS IN  
THE ONE-DIMENSIONAL QUANTUM MAGNETS  
 $\text{Sr}_{0.73}\text{CuO}_2$  AND  $\text{Ca}_{0.83}\text{CuO}_2$   
AND THE MOTT-HUBBARD SYSTEM  $\text{LaTiO}_3$

A dissertation submitted to the



SWISS FEDERAL INSTITUTE OF TECHNOLOGY ZURICH

for the degree of  
Doctor of Natural Sciences

presented by  
GERHARD INGMAR MEIJER  
Master of Science (University of Groningen)  
born 26th September 1972  
from the Kingdom of the Netherlands

accepted on the recommendation of  
Prof. Dr. P. Wachter, examiner  
Dr. C. Rossel, co-examiner  
Dr. J. Karpinski, co-examiner  
Prof. Dr. A. Furrer, co-examiner

1999

# Preface

This manuscript gives an account of my research activities in the period from the autumn of 1995 to the spring of 1999. They were performed in the course of a joint research project of the Swiss Federal Institute of Technology Zurich (ETH) in conjunction with IBM Research Division, Zurich Research Laboratory, with support from the Swiss National Science Foundation.

I thank many colleagues, coworkers, and friends, who have directly and indirectly contributed to this manuscript. I wish to express my gratitude to my advisor Prof. Dr. P. Wachter for giving me the support and the opportunity to do research in this exciting field of physics. I am indebted to Dr. C. Rossel for sharing his knowledge of physics and giving me inspiration and unflagging support whenever needed. Moreover, I am obliged to colleagues, who in the course of this project provided me with high-quality samples. None more so than Dr. J. Karpinski, who skilfully and competently synthesised most of the compounds studied in this thesis. I am grateful to Prof. Dr. A. Furrer for supplying useful comments on a preliminary version of this manuscript and for agreeing to act as co-examiner of this work.

I am particularly indebted to Dr. W. Henggeler, a colleague of long standing, who introduced me to the neutron scattering technique and with whom I had many enlightening discussions.

I thank the International Business Machines Corporation for the excellent support I received during my three years with the IBM Zurich Research Laboratory in Rüschlikon, Switzerland. I wish to take the opportunity to thank Dr. J. Brown, Dr. R. S. Eccleston, Dr. F. Fauth, Dr. L. Keller, and Dr. H. Mutka for their vigorous and competent assistance with the various neutron scattering experiments performed at the Institute Laue Langevin, Grenoble, France, at the Rutherford Appleton Laboratory, Chilton, United Kingdom, and at the Paul Scherrer Institute, Villigen, Switzerland.

In addition, it is a pleasure to acknowledge fruitful and stimulating discussions with Dr. R. Allenspach, Dr. T. Barnes, Dr. J. G. Bednorz, Dr. H.-B. Braun, Dr. J. Fompeyrine, Dr. B. Frischmuth, Dr. J.-P. Locquet, Prof. Dr. T.

M. Rice, Dr. A. Shengelaya, and Dr. M. Willemin. Moreover, I am also very grateful for the sample preparation by Mr. O.-S. Becker, Dr. J. G. Bednorz, Dr. K. Conder, Dr. S. Kazakov, Dr. E. M. Kopnin, and Dr. H. Schwer. To all them my thanks.

I also thank Dr. H. W. M. Salemink and Dr. A. P. J. Engbersen for offering me a position as summer student at the Zurich Research Laboratory in 1994 and for their guidance in the course of my stay in Rüslikon.

The skilful assistance with manuscript preparation of Ms. L.-M. Pavka and Mr. U. Bitterli is gratefully acknowledged. I am very thankful to all my colleagues in Rüslikon and Zurich for most pleasurable working conditions.

And last but not least, I am deeply indebted to my parents and my brother, who, over the years, contributed indirectly but nevertheless significantly to this manuscript by means of their unflagging support.

Rüslikon, March 1999

G. I. Meijer

# Contents

<b>Abstract</b>	<b>vii</b>
<b>Zusammenfassung (German)</b>	<b>ix</b>
<b>1 Introduction</b>	<b>1</b>
<b>2 Experimental methods</b>	<b>9</b>
2.1 Torque magnetometry . . . . .	9
2.1.1 Torque magnetometers . . . . .	10
2.2 Neutron scattering . . . . .	11
2.2.1 Nuclear scattering . . . . .	12
2.2.2 Magnetic scattering . . . . .	13
2.2.3 Neutron scattering instruments . . . . .	15
<b>3 Quasi-1D Sr<sub>0.73</sub>CuO<sub>2</sub></b>	<b>17</b>
3.1 Introduction . . . . .	17
3.2 Low-temperature magnetic order . . . . .	20
3.3 Paramagnetic regime . . . . .	23
<b>4 Quasi-1D Ca<sub>0.83</sub>CuO<sub>2</sub></b>	<b>31</b>
4.1 Introduction . . . . .	31
4.2 Magnetism vs. oxygen vacancies . . . . .	33
4.3 Magnetic order: a torque investigation . . . . .	42
<b>5 Long-range magnetic order Ca<sub>0.83</sub>CuO<sub>2</sub> and Sr<sub>0.73</sub>CuO<sub>2</sub></b>	<b>47</b>
5.1 Introduction . . . . .	47
5.2 Specific heat . . . . .	48
5.3 Neutron diffraction . . . . .	51
5.4 Torque Sr <sub>0.73</sub> CuO <sub>2</sub> . . . . .	55
5.5 Discussion . . . . .	57

<b>6</b>	<b>Spin dynamics <math>\text{Sr}_{0.73}\text{CuO}_2</math></b>	<b>61</b>
6.1	Introduction . . . . .	61
6.2	Excitation spectrum . . . . .	62
6.3	Wave-vector dependence scattering intensity . . . . .	68
6.4	Low-temperature spectrum . . . . .	71
6.5	Appendix: Structure factor of dimers . . . . .	75
6.5.1	Isolated dimers . . . . .	75
6.5.2	Coupled dimers . . . . .	77
<b>7</b>	<b><math>\text{LaTiO}_{3+\delta}</math> upon band filling</b>	<b>81</b>
7.1	Introduction . . . . .	81
7.2	Structure of ordered moment . . . . .	84
7.3	Temperature dependence of the ordered moment . . . . .	85
7.4	Magnetisation of $\text{LaTiO}_{3.07(1)}$ . . . . .	90
<b>8</b>	<b>Conclusions</b>	<b>93</b>

# List of Figures

1.1	Crystallographic structure of $\text{CuGeO}_3$ . . . . .	2
1.2	Crystallographic structure of $(\text{Sr,Ca})_{14}\text{Cu}_{24}\text{O}_{41}$ . . . . .	4
2.1	Cantilever for torque magnetometer . . . . .	10
3.1	Crystallographic structure of $\text{Sr}_{0.73}\text{CuO}_2$ . . . . .	19
3.2	Low-temperature magnetic susceptibility of $\text{Sr}_{0.73}\text{CuO}_2$ . . .	20
3.3	Magnetisation of $\text{Sr}_{0.73}\text{CuO}_2$ versus applied magnetic field . .	21
3.4	Temperature dependence of weak-ferromagnetic saturation moment in $\text{Sr}_{0.73}\text{CuO}_2$ . . . . .	22
3.5	High-temperature susceptibility of $\text{Sr}_{0.73}\text{CuO}_2$ fitted with various 1D models . . . . .	24
3.6	Temperature dependence of susceptibility in alternating chain Heisenberg model $\mathcal{H} = J \sum_i (\mathbf{S}_{2i} \cdot \mathbf{S}_{2i+1} + \alpha \mathbf{S}_{2i} \cdot \mathbf{S}_{2i-1})$ . . .	26
4.1	Crystallographic structure of $\text{Ca}_{0.83}\text{CuO}_2$ . . . . .	32
4.2	Magnetic susceptibility of $\text{Ca}_{0.83}\text{CuO}_{2.009}$ . . . . .	34
4.3	Susceptibility of $\text{Ca}_{0.83}\text{CuO}_{2-\delta}$ ( $-0.009 \leq \delta \lesssim 0.04$ ) . . . . .	35
4.4	Magnetisation of $\text{Ca}_{0.83}\text{CuO}_{2.009}$ versus applied magnetic field	36
4.5	Susceptibility of $\text{Ca}_{0.83}\text{CuO}_{2-\delta}$ fitted with alternating chain Heisenberg model . . . . .	37
4.6	Susceptibility of $\text{Ca}_{0.83}\text{CuO}_{2-\delta}$ fitted with model of coupled quantum spin chains . . . . .	39
4.7	Model for distribution of $\text{Cu}^{2+}$ and holes in $\text{Ca}_{0.83}\text{CuO}_2$ . . .	40
4.8	Angle-dependent torque on $\text{Ca}_{0.83}\text{CuO}_2$ . . . . .	43
4.9	Temperature dependence of torque amplitude in $\text{Ca}_{0.83}\text{CuO}_2$	44
5.1	Specific heat of $\text{Ca}_{0.83}\text{CuO}_2$ and $\text{Sr}_{0.73}\text{CuO}_2$ . . . . .	49
5.2	Low-temperature neutron diffraction pattern of $\text{Ca}_{0.83}\text{CuO}_2$ and $\text{Sr}_{0.73}\text{CuO}_2$ . . . . .	52

5.3	Crystallographic structure of $\text{CuO}_2$ sublattice in $\text{Ca}_{0.83}\text{CuO}_2$ and $\text{Sr}_{0.73}\text{CuO}_2$ . . . . .	53
5.4	(a) Temperature dependence of $\text{Ca}_{0.83}\text{CuO}_2$ (0 1/2 1) neutron peak intensity. (b) Temperature dependence of torque amplitude	54
5.5	(a) Angular-dependent torque on $\text{Sr}_{0.73}\text{CuO}_2$ . (b) Temperature dependence of torque amplitude . . . . .	56
5.6	Model for ordering of $\text{Cu}^{2+}$ and holes in the $\text{CuO}_2$ chains of $\text{Sr}_{14}\text{Cu}_{24}\text{O}_{41}$ . . . . .	58
6.1	Contour plot of neutron scattering intensity from $\text{Sr}_{0.73}\text{CuO}_2$	63
6.2	Excitation spectrum of $\text{Sr}_{0.73}\text{CuO}_2$ . . . . .	64
6.3	Spin excitation spectrum for alternating Heisenberg chain . .	66
6.4	Intensity of the excitation continuum . . . . .	67
6.5	$Q$ dependence of the scattering intensity from $\text{Sr}_{0.73}\text{CuO}_2$ . .	69
6.6	Ground state of chain with nearest- and next-nearest-neighbour exchange couplings upon hole doping . . . . .	70
6.7	Scattering from $\text{Sr}_{0.73}\text{CuO}_2$ at $T = 1.5, 20,$ and $30$ K . . . . .	72
6.8	Effect of doping on spin structure of $\text{CuGeO}_3$ and $\text{Sr}_{0.73}\text{CuO}_2$	73
6.9	Geometry of alternating chain . . . . .	77
6.10	Powder average of dimer structure factor . . . . .	79
7.1	Crystallographic structure of $\text{LaTiO}_3$ . . . . .	83
7.2	Temperature dependence of ordered moment in $\text{LaTiO}_{3+\delta}$ . .	87
7.3	Néel temperature versus AF ordered moment in $\text{LaTiO}_{3+\delta}$ . .	89
7.4	Magnetisation of $\text{LaTiO}_{3.07(1)}$ versus applied field . . . . .	91

# Abstract

This is a study of the magnetic properties of the novel quasi-one-dimensional (1D) quantum magnets  $\text{Sr}_{0.73}\text{CuO}_2$  and  $\text{Ca}_{0.83}\text{CuO}_2$  and the Mott–Hubbard system  $\text{LaTiO}_3$ . Magnetic susceptibility, magnetic torque, specific heat, neutron diffraction, and inelastic neutron scattering techniques have been used successfully to resolve the magnetic properties of these compounds.

First, the static magnetic susceptibility of quasi-1D  $\text{Sr}_{0.73}\text{CuO}_2$  was investigated. This cuprate comprises Cu spin chains ( $\text{Cu}^{2+}$  has  $S = 1/2$ ). The spin chains are highly diluted with nonmagnetic holes, i.e.,  $\sim 0.6$  holes per Cu are present. The holes are localised. The susceptibility reveals that  $\text{Sr}_{0.73}\text{CuO}_2$  develops antiferromagnetic (AF) order at  $T \sim 10$  K.  $\text{Sr}_{0.73}\text{CuO}_2$  exhibits a small spontaneous ferromagnetic moment  $M_s \sim 4 \times 10^{-3} \mu_B/\text{Cu}$  due to canting of the spins away from the direction of the staggered magnetisation. Magnetic order in Cu spin systems doped with such a substantial hole doping has never been observed before. At  $T > 10$  K, the susceptibility can be described by the 1D Heisenberg Hamiltonian with alternating exchange coupling. This is the first indication of dimerisation of the Cu spins.

The static magnetic susceptibility and torque anisotropy were measured on the cuprate  $\text{Ca}_{0.83}\text{CuO}_{2-\delta}$ . This compound is nearly isomorphous to  $\text{Sr}_{0.73}\text{CuO}_2$ . Hole doping of between 0.27 and 0.36 holes per Cu can be achieved by changing the oxygen stoichiometry. The magnetic properties of  $\text{Ca}_{0.83}\text{CuO}_{2-\delta}$  are similar to those of  $\text{Sr}_{0.73}\text{CuO}_2$ : a transition into an AF ordered state was observed at  $T \sim 12$  K, and at higher temperatures  $\text{Ca}_{0.83}\text{CuO}_{2-\delta}$  behaves as an alternating Heisenberg chain. By torque analysis the existence of an easy axis in the ordered state was clearly demonstrated and its orientation determined.

Next, the AF ordered phase of  $\text{Sr}_{0.73}\text{CuO}_2$  and  $\text{Ca}_{0.83}\text{CuO}_2$  below  $T \sim 10$  K was investigated further. Specific heat, neutron diffraction, and torque measurements were performed. In both compounds a peak of the specific heat was observed at  $T \sim 10$  K, which is attributed to a static magnetic transition. Magnetic Bragg peaks were identified in the neutron diffraction



patterns. This proves rigorously that the AF ordered state in  $\text{Ca}_{0.83}\text{CuO}_2$  and  $\text{Sr}_{0.73}\text{CuO}_2$  is of long-range 3D character.

Spin dynamics in  $\text{Sr}_{0.73}\text{CuO}_2$  were measured by inelastic neutron scattering. Well-defined excitations at  $E = 10$  and  $17.5$  meV were observed in the spectrum. Additional magnetic scattering remains present up to  $E \sim 25$  meV. These features are due to excitations of dimerised AF chains; the two peaks are associated with the dispersion of the lowest-lying magnon branch, whereas the scattering in the region up to  $E \sim 25$  meV is consistent with an excitation continuum. The wave-vector dependence of the scattering intensity gives convincing evidence that the dimers are formed between next-nearest-neighbour Cu atoms. The spin excitation gap of  $\Delta \sim 10$  meV remains present below the long-range magnetic ordering temperature  $T \sim 10$  K, which corroborates the coexistence of the quantum-mechanical singlet ground state and the classical Néel ordered state. These two different ground states are generally mutually exclusive with only one exception known up to now: the doped spin–Peierls compound  $\text{CuGeO}_3$ . The current finding shows that such a fascinating coexistence is not restricted to a spin–Peierls system.

At the end of the manuscript, neutron diffraction and static magnetic susceptibility experiments on single crystals of the doped Mott–Hubbard insulator  $\text{LaTiO}_{3+\delta}$  (distorted Perovskite structure) are reported. The magnetic properties of this three-dimensional correlated system were investigated upon hole doping. The size of the ordered moment of  $\text{Ti}^{3+}$  in the canted AF ordered phase reaches a maximum of  $0.46(2)\mu_B$  for  $\text{LaTiO}_3$ . Upon increasing the band filling, i.e., upon increasing the amount of nonstoichiometric oxygen  $\delta$  from 0 to  $\sim 0.08$ , the ordered moment on  $\text{Ti}^{3+}$  is shown to decrease rapidly. The magnetic order is suppressed for doping levels exceeding  $\sim 0.16$  holes per Ti. The weak-ferromagnetic saturation moment of  $\text{LaTiO}_{3.07(1)}$ , on the verge of the insulator–to–metal transition, is reached via a series of steps in the magnetisation curve.

# Zusammenfassung

In dieser Arbeit werden die magnetischen Eigenschaften der neuen quasi-eindimensionalen (1D) Quantenmagneten  $\text{Sr}_{0.73}\text{CuO}_2$  und  $\text{Ca}_{0.83}\text{CuO}_2$  sowie der Mott–Hubbard Substanz  $\text{LaTiO}_3$  dargestellt. Suszeptibilitätsmessungen, Bestimmung des magnetischen Drehmoments, Messung der spezifischen Wärme, Neutronenbeugung sowie inelastische Neutronenstreuung dienten als experimentelle Hilfsmittel, um ihre magnetischen Eigenschaften zu studieren.

Zuerst wurde die statische magnetische Suszeptibilität von quasi-1D  $\text{Sr}_{0.73}\text{CuO}_2$  untersucht. Dieses Kuprat besitzt Cu-Spinketten ( $\text{Cu}^{2+}$  ist ein Spin  $S = 1/2$  Ion). Die Spinketten sind hochgradig dotiert mit  $\sim 0.6$  nicht-magnetischen Löchern pro Cu-Atom. Alle Löcher sind lokalisiert. Die Suszeptibilität zeigt, daß sich  $\text{Sr}_{0.73}\text{CuO}_2$  antiferromagnetisch (AF) ordnet bei  $T \sim 10$  K.  $\text{Sr}_{0.73}\text{CuO}_2$  hat ein kleines ferromagnetisches Moment  $M_s \sim 4 \times 10^{-3} \mu_B/\text{Cu}$  infolge einer Verkantung des AF-geordneten Gitters. Magnetische Ordnung in Kuprat-Materialien bei so großer Löcherdotierung ist einzigartig. Die Suszeptibilität oberhalb  $T \sim 10$  K kann mit einem 1D Heisenberg Hamiltonian mit alternierender Austauschwechselwirkung beschrieben werden. Dies ist eine erste Hinweis für eine Dimerisierung der Cu-Spins.

Die statische magnetische Suszeptibilität und die Drehmomentanisotropie wurden an dem Kuprat  $\text{Ca}_{0.83}\text{CuO}_{2-\delta}$  gemessen. In dieser Substanz kann eine Löcherdotierung zwischen 0.27 und 0.36 Löcher pro Cu durch Änderung der Sauerstoffstöchiometrie erzielt werden. Die magnetischen Eigenschaften sind ähnlich wie die von  $\text{Sr}_{0.73}\text{CuO}_2$ : eine AF Ordnung wurde bei  $T \sim 12$  K gefunden. Bei höheren Temperaturen verhält sich auch  $\text{Ca}_{0.83}\text{CuO}_{2-\delta}$  wie eine alternierende Heisenberg-Kette. Mit der Drehmomentanalyse wurde die Richtung der *easy*-Achse bestimmt.

Anschließend wurde die AF-geordnete Phase von  $\text{Sr}_{0.73}\text{CuO}_2$  und  $\text{Ca}_{0.83}\text{CuO}_2$  unterhalb  $T \sim 10$  K weiter untersucht. Messungen der spezifischen Wärme sowie des Drehmomentes und Neutronenbeugungsexperimente wurden durchgeführt. In beiden Materialien wurde ein Übergang in der spezifischen Wärme bei  $T \sim 10$  K gefunden. Dieser wurde als Anzeichen für

eine statische magnetische Ordnung interpretiert. Magnetische Bragg-Peaks wurden in den Neutronenbeugungsdiagrammen identifiziert. Dies beweist eindeutig, daß der AF-geordnete Zustand einen langreichweitigen dreidimensionalen Charakter hat.

Als nächstes werden die Spinanregungen von  $\text{Sr}_{0.73}\text{CuO}_2$  behandelt, die mittels inelastischer Neutronenstreuung gemessen wurden. Im Spektrum wurden gut definierte Anregungen bei  $E = 10$  und  $17.5$  meV beobachtet. Zusätzliche Streuung bleibt bis  $E \sim 25$  meV meßbar. Dieses Verhalten wird anhand von Anregungen von dimerisierten AF Spinketten erklärt; die zwei Anregungen sind mit der Dispersion des niederenergetischen Magnonbandes assoziiert. Die Streuung in der Region bis  $E \sim 25$  meV ist konsistent mit einem Anregungskontinuum. Die Wellenvektorabhängigkeit der Streuintensität ist ein sehr überzeugender Beweis dafür, daß die Dimere zwischen übernächsten Cu-Nachbarn geformt werden. Die Spinanregungslücke von  $\Delta \sim 10$  meV bleibt unterhalb der langreichweitigen Ordnungstemperatur  $T \sim 10$  K erhalten. Dies beweist, daß der quantenmechanische singlet-Zustand und die klassische langreichweitige Ordnung koexistieren. Diese zwei unterschiedlichen Grundzustände schließen sich normalerweise aus. Bislang war nur eine einzige Ausnahme bekannt: die leichtdotierte spin-Peierls Substanz  $\text{CuGeO}_3$ . Unser Ergebnis zeigt jetzt eindeutig, daß ein solches, faszinierendes Verhalten nicht ausschließlich in einem spin-Peierls Material vorkommt.

Im letzten Teil der vorliegenden Arbeit werden Neutronendiffraktion und Messungen der magnetischen Suszeptibilität an Einkristallen des dotierten Mott-Hubbard Isolators  $\text{LaTiO}_{3+\delta}$  vorgestellt welcher eine verzerrte Perovskit-Struktur aufweist. Die magnetischen Eigenschaften dieses dreidimensional-korrelierten Elektronensystems wurden in Abhängigkeit der Löcherdotierung untersucht. Die Größe des geordneten Momentes von  $\text{Ti}^{3+}$  in der verkanteten, AF-geordneten Phase hat ein Maximum von  $0.46(2)\mu_B$  für  $\text{LaTiO}_3$ . Die Größe des geordneten Momentes nimmt bei zunehmender Füllung des Bandes (bei zunehmendem nichtstöchiometrischem Sauerstoffgehalt  $\delta$  von 0 bis  $\sim 0.08$ ) schnell ab. Die magnetische Ordnung wird unterdrückt, wenn die Löcherdotierung den Wert von  $\sim 0.16$  Löcher/Ti überschreitet. Der schwach-ferromagnetische Sättigungswert des Momentes von  $\text{LaTiO}_{3.07(1)}$ , nahe des Metall-Isolator Überganges, wird über eine Reihe von Stufen in der Magnetisierungskurve erreicht.

# Chapter 1

## Introduction

Low-dimensional magnets have attracted considerable interest owing to the quantum mechanical nature of their ground state. Because of the increased importance of quantum fluctuations, i.e., the tendency of spins to flip spontaneously, these systems exhibit many distinctive collective properties at low temperatures, which have no counterpart in higher dimensions. Arguably the most prominent examples in this context are the pseudo two-dimensional (2D) layered copper oxides, which in their undoped states are isotropic Heisenberg antiferromagnetic Mott insulators. The remarkable discovery of high- $T_c$  superconductivity upon doping in these layered cuprates by J. G. Bednorz and K. A. Müller in 1986 [1] sparked an effort to explore these and related materials. In fact, this particular discovery stimulated the profound interest in the properties of correlated electron systems in low-dimensional transition metal oxides.

Whereas in 2D spin systems long-range antiferromagnetic (AF) order is stabilised at low temperatures [2], the properties of one-dimensional (1D) spin  $S = 1/2$  materials are drastically different. Bethe demonstrated in the 1930s that 1D Heisenberg spin systems cannot sustain a spontaneous magnetisation as the magnetic order is suppressed by quantum fluctuations [3, 4, 5]. Instead, these systems exhibit a disordered critical ground state characterised by a slow decay of spin correlations and gapless spin excitations [6], that is, there is no cost in energy to create an excitation with  $S = 1$ . A particular interesting phenomenon of quantum mechanical origin that can occur in homogeneous Heisenberg chains is the spin–Peierls transition. Analogous to the Peierls instability towards dimerisation in quasi-1D metals [7], the energy of spin chains is lowered by dimerising into an alternating pattern of weak and strong exchange couplings. This transition is therefore driven

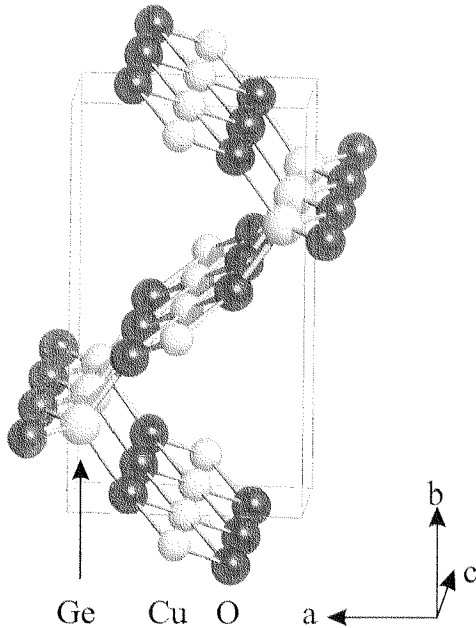


Figure 1.1: Perspective view of the crystallographic structure of CuGeO<sub>3</sub> showing GeO<sub>4</sub> tetrahedrons and CuO<sub>2</sub> chains running along the  $c$  axis. The view is parallel to the  $c$  axis.

by the magnetic energy gain, which overcompensates the lattice deformation energy [8]. The Peierls transition also naturally involves the lattice degrees of freedom due to the alternating distortion of atomic positions. A thoroughly investigated inorganic compound in which the spin-Peierls spin model is firmly established is CuGeO<sub>3</sub> ( $T_{\text{SP}} \sim 14$  K), shown in Fig. 1.1. In the spin-Peierls phase of CuGeO<sub>3</sub>, the copper moments along the chains form dimers, and it takes a finite amount of energy to excite each pair to a spin triplet. Simultaneously with the opening of the spin gap, the lattice undergoes a structural change characterised by a small distortion along the chains direction [9]. Another more recently discovered inorganic substance undergoing a spin-Peierls transition is  $\alpha'$ -NaV<sub>2</sub>O<sub>5</sub> ( $T_{\text{SP}} \sim 34$  K) [10].

For a spin  $S = 1$  homogeneous 1D Heisenberg antiferromagnet a singlet ground state with finite spin excitation gap was conjectured in the pioneering work of Haldane [11]. He investigated the effects of quantum fluctuations on the dynamics of the isotropic 1D Heisenberg Hamiltonian. Haldane found that the physical properties of AF quantum spin chains depend crucially on whether the spin is an integer ( $S = 1, 2, \dots$ ) or a half-odd-integer ( $S =$

$1/2, 3/2, \dots$ ). This challenged the conventional wisdom that the properties of these chains were generically given by the Bethe ansatz solution of the spin  $S = 1/2$  chain, which has a gapless excitation spectrum and an infinite correlation length. Integer spin chains, however, were shown to have a singlet ground state separated from the excited states by an energy gap. Examples of compounds that possess a Haldane gap include  $\text{Ni}(\text{C}_2\text{H}_2\text{N}_2)_2\text{NO}_2\text{ClO}_4$  [12],  $\text{Y}_2\text{BaNiO}_5$  [13], and  $\text{CsNiCl}_3$  [14].

Among the recent challenging fields of low-dimensional quantum magnetism, which have emerged from the wealth of activity directed at improving the understanding of high- $T_c$  superconductors, is that of arrays of coupled quantum spin chains, the so-called spin ladder systems [15]. They are obtained by assembling chains to each other. These magnetic systems are thus situated between the 1D and 2D quantum magnets. Neither of these two extremes has a spin gap. The dimensional crossover from the slowly decaying AF correlations of the 1D  $S = 1/2$  chain to the long-range AF order of the square lattice is surprising complex. Ladders consisting of an even number of chains have purely short-range correlations, a spin singlet ground state, and concomitantly a finite spin gap to the lowest excitations. They resemble to a certain degree the integer spin chain discussed by Haldane [11]. This contrasts with a ladder made of an odd number of chains that belong to the same universality class as the single chains. They have gapless spin excitations and a power-law decay of the spin correlations. These two types of quantum ground states lead to fundamentally different thermal properties for even- and odd-leg ladders. Good experimental realisations of these systems confirming the theoretical predictions are  $\text{SrCu}_2\text{O}_3$  (two-leg),  $\text{Sr}_2\text{Cu}_3\text{O}_5$  (three-leg), and  $\text{La}_2\text{Cu}_2\text{O}_5$  (two-leg) [15, 16]. Interestingly enough,  $(\text{VO})_2\text{P}_2\text{O}_7$  initially recognised as an early prototype of a two-leg ladder turned out to be misinterpreted.

An important issue is the effect of hole doping on these spin ladder systems. The presence of holes essentially transforms some of the copper  $\text{Cu}^{2+}$  ( $S = 1/2$ ) to  $\text{Cu}^{3+}$  (Zhang-Rice singlet  $S = 0$  [17, 18]) sites. Theoretical studies of doped ladders suggested that the spin gap in even-leg ladders survives the presence of holes, and that the spin-gap phase is favourable for superconductivity as there is an attractive interaction between the holes [19]. Ever since this first hint, a significant effort was made to synthesise ladder compounds in search of superconductivity. These endeavours established superconductivity under high pressure in  $\text{Sr}_{0.4}\text{Ca}_{13.6}\text{Cu}_{24}\text{O}_{41.84}$  ( $T_c \sim 12$  K at a pressure of 3 GPa) [20, 21]. This compound consists of two distinct Cu-O subcells as shown in Fig. 1.2(a). One contains the two-leg ladders [Fig. 1.2(b)], the other consists of 1D spin chains [Fig. 1.2(c)]. The complicated

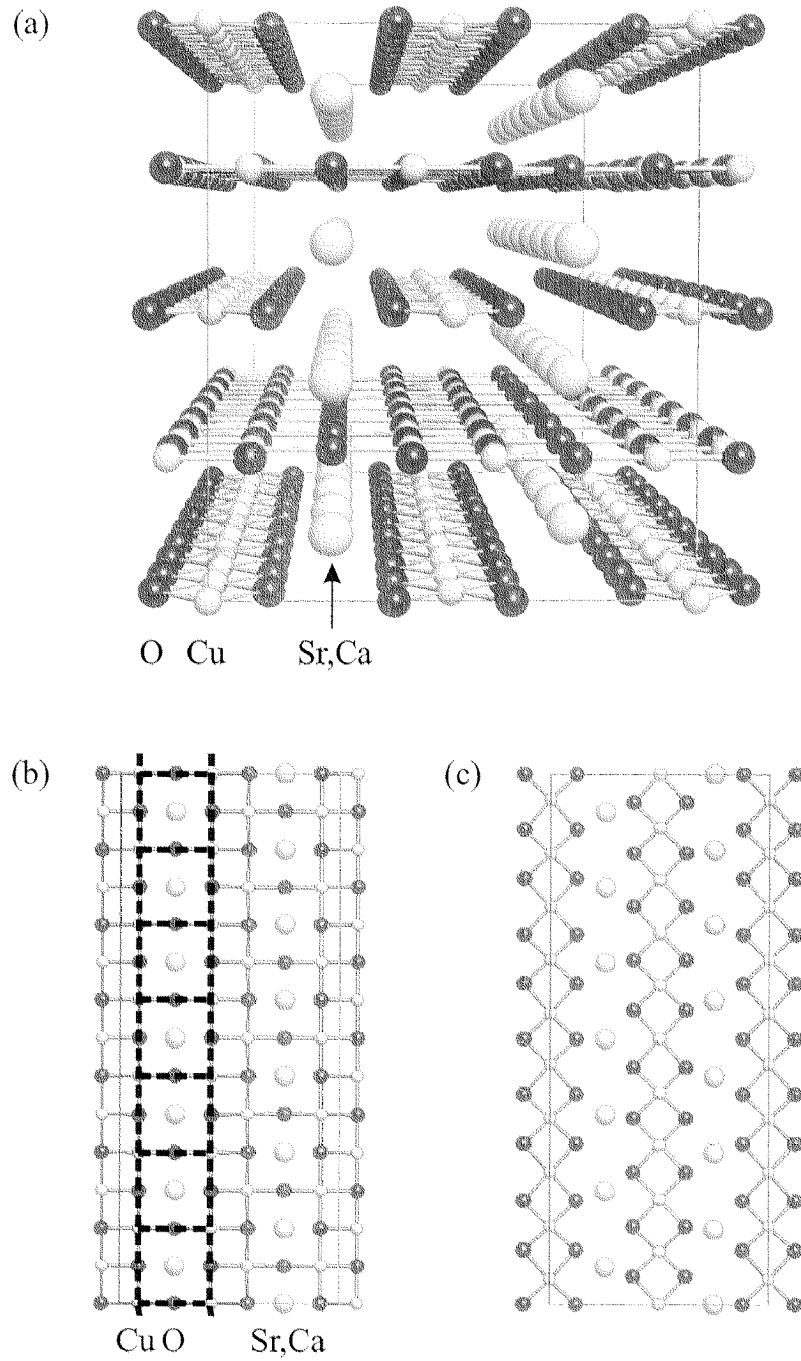


Figure 1.2: (a) Perspective view of the crystal structure of  $(\text{Sr,Ca})_{14}\text{Cu}_{24}\text{O}_{41}$  along the chain/ladder direction. Schematic representation of the two building blocks, (b) a  $\text{Cu}_2\text{O}_3$  two-leg ladder plane and (c) a  $\text{CuO}_2$  chain. The two-leg ladder is indicated by the dashed lines in (b).

crystal structure renders it controversial whether the superconductivity in this material can be simply attributed to the ladders.

A surprising experimental discovery in conjunction with the spin–Peierls compounds has been that the introduction of nonmagnetic sites in  $\text{CuGeO}_3$  leads to the enhancement of the propensity of spins to show long-range order, rather than to a diminution of the correlations due to disorder as one might expect intuitively [22]. The Néel temperature increases upon doping and, more surprisingly, the long-range ordered and the spin–Peierls states coexist in a considerably large range of doping. This is observed for various dopants such as Zn, Mg, and Ni at the Cu site and also by replacing a small amount of Ge by Si [22]. The phenomenon is highly unusual because the spin-ordered state is generated by randomly replacing spins by vacancies, which is an apparently disordering procedure. Moreover, the fascinating coexistence of the spin–Peierls state with the classical Néel state has attracted much interest as these two different ground states were generally believed to be mutually exclusive. In theoretical studies, it was reasoned that random depletion of spins might lead to a local enhancement of classical AF correlations [23, 24, 25, 26]. It was conjectured that this may trigger the long-range order. However, the explicit pathway by which dilution promotes 3D Néel order remains elusive.

The above examples are representative illustrations of the rich mine of physics that rule low-dimensional quantum magnets. Most of the remarkable features, most of which are not at all intuitive, observed in these systems are pure quantum effects due uniquely to their low dimensionality. This is why magnetism in low-dimensional spin systems is a perennially attractive subject. Doping low-dimensional transition metal oxides in general and cuprates in particular has drawn significant attention in recent years. An important aspect in this context are studies of the magnetic properties of these transition metal oxides. It is hoped that from such studies new insight into the intriguing properties of these highly correlated materials, among them high- $T_c$  superconductors, will emerge. This is the reason I concentrated in this manuscript on various aspects of magnetic correlations in transition metal oxides. The main part of this work illustrates in some detail a number of experimental studies of two novel quasi-1D quantum magnets:  $\text{Sr}_{0.73}\text{CuO}_2$  and  $\text{Ca}_{0.83}\text{CuO}_2$ . These two cuprates are isomorphic with the chain subcell of  $\text{Sr}_{0.4}\text{Ca}_{13.6}\text{Cu}_{24}\text{O}_{41.84}$  displayed in Fig. 1.2(c) [27].<sup>1</sup> Note that no ambiguity can arise from the presence of a ladder subcell. The chains of cop-

---

<sup>1</sup>In this series also “ $\text{Ba}_{0.67}\text{CuO}_2$ ” can be synthesised. Susceptibility measurements indicate that the one-dimensionality of the magnetic lattice of this compound is less apparent. The measurements on  $\text{Ba}_{0.67}\text{CuO}_2$  are too preliminary to be included in this manuscript.



per spins, although chemically imbedded in a 3D crystal structure, are only loosely linked among each other in terms of magnetic couplings.  $\text{Sr}_{0.73}\text{CuO}_2$  and  $\text{Ca}_{0.83}\text{CuO}_2$  are highly hole-doped, i.e., there are inherently 0.54 and 0.34 holes, respectively, per Cu present (copper valency is 2.54+ and 2.34+, respectively). As the holes are strongly localised, the compounds can be described by Hamiltonians where the relevant degrees of freedom are localised spins. Their magnetic properties appear to be truly unique. The excitement surrounding these compounds was triggered by the finding that they exhibit long-range AF order at  $T \sim 10$  K. This observed Néel order is counterintuitive, because based on classical intuition one would have expected a diminution of correlations due to huge dilution, and hence a reduced tendency to order.

This is not all. The spin system in  $\text{Sr}_{0.73}\text{CuO}_2$  will be shown to dimerise, not due to a spin–Peierls transition as in  $\text{CuGeO}_3$  but due to hole ordering (resulting in a combined spin-charge density wave). Moreover, it will be shown that the spin dimer phase coexists with long-range AF order below  $T \sim 10$  K. This finding shows that such coexistence is not restricted to the doped spin–Peierls system  $\text{CuGeO}_3$ .

Finally, we will briefly leave the field of quasi-1D compounds to examine doping effects in the three-dimensional Mott insulator  $\text{LaTiO}_3$ . This transition metal oxide, apart from the fact that it is also a strongly correlated Mott insulator, is not directly related to the previously discussed quasi-1D quantum magnets. I felt nonetheless that it might be instructive to include a rather intuitive comparison from the 3D “world” in this manuscript. We will mainly examine the reduction of the ordered moment upon hole doping. It might serve as a useful reference and will show once more how remarkable the observed magnetic properties of the highly doped quasi-1D cuprates  $\text{Sr}_{0.73}\text{CuO}_2$  and  $\text{Ca}_{0.83}\text{CuO}_2$  are.

Most of the experiments on  $\text{Sr}_{0.73}\text{CuO}_2$  and  $\text{Ca}_{0.83}\text{CuO}_2$  described in this thesis have been performed on polycrystals [27]. As these compounds are synthesised at high oxygen pressure, it is only possible to grow relatively small single crystals. Several experimental techniques were employed to reveal the unique magnetic properties of these cuprates. The thermodynamics have been studied with superconducting quantum interference device (SQUID) magnetometry and specific heat measurements. To obtain information on the magnetic properties of the single crystals the ultimately sensitive torque magnetometers were used [28, 29, 30]. Moreover, elastic and inelastic neutron scattering techniques were applied because unique information on the physics of materials is provided that cannot be obtained by other means. Units are a troublesome issue in discussing experiments on magnetism [31],

as the SI conventions have not yet been adopted in this field. To allow direct comparison with literature, I will adhere to the electro-magnetic units (emu) in the discussion of the magnetic susceptibility throughout this thesis.

The layout of this thesis is as follows. Chapter 2 briefly discusses the background of torque magnetometry and neutron scattering as they relate to the scope of this thesis. In Chapter 3 the static magnetic susceptibility of polycrystalline  $\text{Sr}_{0.73}\text{CuO}_2$  is investigated. The measurements presented will serve as a guide and stimulus for other experiments discussed in this thesis. We will see evidence of magnetic ordering at  $T \sim 10$  K and get a first indication that the spin chains of  $\text{Sr}_{0.73}\text{CuO}_2$  dimerise at low temperatures. Chapter 4 continues the discussion of low-dimensional magnetism with the susceptibility of  $\text{Ca}_{0.83}\text{CuO}_2$ . This compound has certain magnetic properties that are similar to those of  $\text{Sr}_{0.73}\text{CuO}_2$ . To provide convincing evidence that also this compound exhibits magnetic order, torque measurements on a single crystal will be presented.

Chapter 5 is devoted to a further investigation of the magnetically ordered phase at low temperatures, to a discussion of specific heat and neutron diffraction of polycrystalline  $\text{Ca}_{0.83}\text{CuO}_2$  and  $\text{Sr}_{0.73}\text{CuO}_2$ , and to magnetic torque measurements on single crystals. These measurements corroborate that both materials exhibit long-range 3D AF order at  $T \sim 10$  K.

Chapter 6 reports on spin dynamics of polycrystalline  $\text{Sr}_{0.73}\text{CuO}_2$  measured by inelastic neutron scattering. These measurements provide convincing evidence that  $\text{Sr}_{0.73}\text{CuO}_2$  exhibits a spin gap in its excitation spectrum. Our measurements will show that this gap is due to dimerisation of next-nearest-neighbour copper ions separated by a nonmagnetic hole. Moreover, we will prove that the excitation gap remains present below the Néel ordering temperature. In reading Chapter 6, hopefully the reader will share the joy of seeing how nicely the measurements discussed in Chapters 3, 5, and 6 fit together to produce a consistent picture of the unique magnetic properties of this quasi-1D magnet.

Finally, in Chapter 7 the magnetic properties of the three-dimensional correlated electron system  $\text{LaTiO}_{3+\delta}$  ( $0 < \delta \lesssim 0.1$ ) are examined with reference to neutron-diffraction and magnetic-susceptibility measurements on a series of large single crystals grown by floating zone melting. A brief comparison with the quasi-1D cuprates will be drawn.

The work presented in this thesis has been published in part as Refs. [31, 32, 33, 34, 35, 36].

Seite Leer /  
Blank leaf

# Chapter 2

## Experimental methods

### 2.1 Torque magnetometry

In this section we will briefly examine some of the principles of the torque magnetometry technique as they relate to the scope of this thesis. The interested reader may also consult Willemin, Ref. [37], which includes an elucidating discussion of the application of torque magnetometry to high- $T_c$  superconductors.

The preparation of high-quality single crystals of suitable size is not always straightforward, especially for compounds with a complex chemical structure. Moreover, the fact that the best single crystals are usually the smallest ones places stringent conditions on the sensitivity of the measuring device. One of the tools typically used to measure the magnetic properties of small samples is the superconducting quantum interference device (SQUID). Commercial SQUID magnetometers are indeed very sensitive for measuring small magnetic moments, but the investigation of microcrystals with a magnetic moment of the order of  $\sim 10^{-7}$  emu is typically the lower bound for this technique to be useful.

Torque magnetometry is complimentary to the SQUID magnetometry for measuring the magnetisation as a function of temperature or applied magnetic field. In this thesis the torque magnetometer is used because of its greater sensitivity than that of a commercial SQUID magnetometer.

A magnetic dipole in an external magnetic field experiences a torque. The torque generated by a field  $\mathbf{B}$  on a sample with magnetic moment  $\mathbf{m}$  is given by

$$\boldsymbol{\tau} = \mathbf{m} \times \mathbf{B}. \tag{2.1}$$

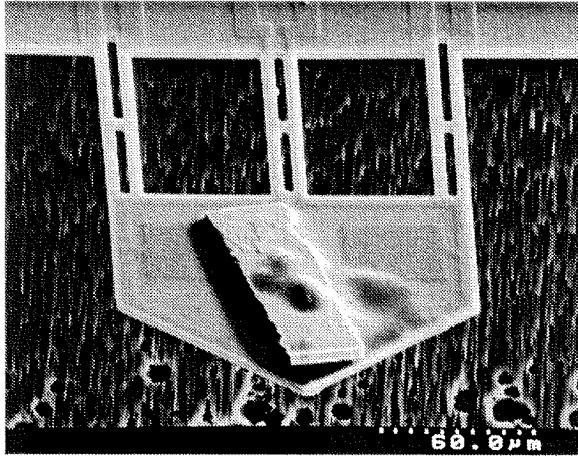


Figure 2.1: Scanning electron microscope image of the piezoresistive cantilever for torque magnetometer with crystal [28, 29].

The magnetic moment  $\mathbf{m}$  of crystals can thus be measured via the torque  $\boldsymbol{\tau} = \mathbf{m} \times \mathbf{B}$  produced on them by a homogeneous magnetic field  $\mathbf{B}$ . This naturally requires the sample to be (slightly) anisotropic, otherwise  $\boldsymbol{\tau}$  would be zero. Moreover, only in the magnetically ordered state is a torque expected because in the paramagnetic state each magnetic ion is, naively speaking, equipped with freely swivelling magnetic moments  $\mathbf{m}$ , which in a field  $\mathbf{B}$  would be found pointing in the direction of the field (with  $\boldsymbol{\tau} = \mathbf{m} \times \mathbf{B} = 0$  as the consequence). Consequently, measuring the temperature dependence of the torque yields direct information about the magnetic ordering temperature.

### 2.1.1 Torque magnetometers

Several types of torque magnetometers were used previously. After the earlier versions of torque magnetometers based on the the torsion pendulum [38], much progress was made to render this technique more sensitive. Recent improvements in the design of torque sensors and detection electronics have led to a sensitivity of the torque signal of typically  $\Delta\tau \lesssim 10^{-13}$  Nm [28, 29, 30]. Advanced versions are, for example, capacitance torque magnetometers, in which a flexible beam holding the sample is symmetrically positioned between two capacitor plates [30]. The induced rotation of the sample fixed on the cantilever generates a deflection, which causes a change in the capacity that can be measured.

Pursuing the goal of miniaturisation, ultrasensitive torque magnetometers have been developed based on microfabricated silicon piezoresistive can-

tilevers such as those used in atomic force microscopy, see Fig. 2.1 [28, 29]. The sample is mounted at the extremity of the cantilever, and the deflection produced by the torque is measured by the change in piezoresistance. The small size and mass of these devices in addition to their ultrahigh sensitivity allow very short response times.

With the piezoresistive cantilever, a sensitivity of the torque signal of typically  $\Delta\tau \lesssim 10^{-13}$  Nm is reached. This allows the measurement of magnetic moments of  $\Delta m \sim 10^{-13}$  Am<sup>2</sup> in a field of  $B = 1$  T. For comparison, a commercial SQUID magnetometer has a typical sensitivity of  $\Delta m \sim 10^{-7}$  emu, which corresponds to  $\Delta m \sim 10^{-10}$  Am<sup>2</sup>, i.e., about 3 orders of magnitude less sensitive than the miniaturised torque magnetometer. This was essential for the investigation of crystals of Sr<sub>0.73</sub>CuO<sub>2</sub> and Ca<sub>0.83</sub>CuO<sub>2</sub>. Of these compounds only microcrystals are available (volume order of  $V \sim 1 \times 10^{-3}$  mm<sup>3</sup>), so one can scarcely hope to be able to measure a meaningful signal on the most sensitive commercial SQUID magnetometers.

## 2.2 Neutron scattering

In neutron scattering experiments, monochromatised neutrons with initial wave-vector  $\mathbf{k}_i$  and energy  $E_i = \hbar^2 k_i^2 / 2m$  ( $m$  is the mass of a neutron) are typically scattered from condensed matter into a state with final wave-vector  $\mathbf{k}_f$  and energy  $E_f$ . Each scattering event is characterised, therefore, by the momentum  $\hbar\mathbf{Q} = \hbar\mathbf{k}_i - \hbar\mathbf{k}_f$  and the energy  $\hbar\omega = E_i - E_f$  transferred to the sample. These scattering processes can be caused by two interactions: (i) the neutron-nuclear interaction via nuclear forces, and (ii) the interaction of the neutron's magnetic dipole moment with the local magnetic field of an atomic magnetic moment.

In general, the partial differential cross section for scattering of neutrons by a potential  $\hat{\mathcal{V}}$  is given by

$$\frac{d^2\sigma}{d\Omega_f dE_f} = \frac{k_f}{k_i} \sum_{\lambda_i} p_{\lambda_i} \sum_{\lambda_f} |\langle \mathbf{k}_f \lambda_f | \hat{\mathcal{V}} | \mathbf{k}_i \lambda_i \rangle|^2 \delta(\hbar\omega + E_{\lambda_i} - E_{\lambda_f}), \quad (2.2)$$

where  $\lambda_i$  and  $\lambda_f$  are the initial and final quantum states of the scattering system, respectively, and  $p_{\lambda_i}$  is the probability that the scattering system is in the state  $\lambda_i$  [39, 40]. This scattering cross section yields the number of neutrons scattered per second into a solid angle  $d\Omega_f$  with a final energy between  $E_f$  and  $E_f + dE_f$ , normalised by the incident neutron flux.

### 2.2.1 Nuclear scattering

The interaction of a neutron with the nuclei in the scattering system is represented by the Fermi pseudopotential, which, for a single nucleus, is given by

$$\hat{\mathcal{V}}(\mathbf{r}) = \frac{2\pi\hbar^2}{m} b_i \delta(\mathbf{r} - \mathbf{r}_i), \quad (2.3)$$

where  $b_i$  is the scattering length of a nucleus  $i$  located at position  $\mathbf{r}_i$ . The scattering length  $b_i$  is a measure of the strength of the interaction between the neutron and the nucleus. As the range of the nuclear potential is small compared to the wavelength  $\lambda$  of the neutron, i.e.,  $b_i \sim 10^{-14}$  m vs.  $\lambda \sim 10^{-10}$  m, the nucleus effectively acts as a point scatterer causing isotropic ( $S$ -wave) scattering. For an assembly of nuclei the potential  $\hat{\mathcal{V}}(\mathbf{r})$  is the sum of individual neutron-nucleus interactions:

$$\hat{\mathcal{V}}(\mathbf{r}) = \frac{2\pi\hbar^2}{m} \sum_i b_i \delta(\mathbf{r} - \mathbf{r}_i), \quad (2.4)$$

where the sum is taken over all the sites in the sample. Inserting  $\hat{\mathcal{V}}$  into Eq. (2.2) yields the neutron cross section due to nuclear scattering.

In the case of a neutron diffraction experiment, neutrons scattered into a solid angle  $d\Omega$  are counted without analysing their final energy. Thus even though diffraction is predominantly an elastic process ( $\hbar\omega = 0$ ) diffractometers integrate over the energies of scattered neutrons  $E_f$ . One can derive the following expression for the differential cross section of coherent elastic neutron scattering

$$\left. \frac{d\sigma}{d\Omega} \right|_{\text{el}}^{\text{coh}} = \int_0^\infty \frac{d^2\sigma}{d\Omega_f dE_f} dE_f = N \frac{(2\pi)^3}{v_0} \sum_{\boldsymbol{\tau}} |F_N(\mathbf{Q})|^2 \delta(\mathbf{Q} - \boldsymbol{\tau}), \quad (2.5)$$

where  $N$  is the number of unit cells of volume  $v_0$  in the sample and  $\boldsymbol{\tau}$  are the reciprocal-lattice vectors [39, 40].  $F_N(\mathbf{Q})$  is the nuclear unit cell structure factor defined by

$$F_N(\mathbf{Q}) = \sum_d b_d e^{-W_d} \exp(i\mathbf{Q} \cdot \mathbf{d}), \quad (2.6)$$

where the sum is taken over the atoms in the unit cell. The temperature-dependent Debye–Waller factor  $\exp(-W_d)$  takes account of the oscillation of the atoms about their equilibrium positions.

### 2.2.2 Magnetic scattering

So far we have examined only the interaction between neutrons and atomic nuclei. Now we consider the magnetic scattering due to the interaction between the neutron's magnetic dipole moment and dipole moments of unpaired electrons in the atoms of the sample. Owing to the dipolar nature of magnetic interaction, magnetic scattering, unlike its nuclear counterpart, is not isotropic. Only the component of the sample's magnetic moment that is perpendicular to the scattering vector  $\mathbf{Q}$  is effective in scattering neutrons. Neutron scattering is therefore not only sensitive to the spatial distribution of the magnetic moments but also to their orientation.

Neutrons have a magnetic dipole moment

$$\boldsymbol{\mu}_n = -\gamma\mu_N\boldsymbol{\sigma}, \quad (2.7)$$

where  $\mu_N$  is the nuclear magneton  $e\hbar/2m_p$  ( $e$  is the elementary charge and  $m_p$  is the mass of the proton),  $\boldsymbol{\sigma}$  is the Pauli spin operator (the magnitude of  $\boldsymbol{\sigma}$  is 1), and  $\gamma$  is a constant  $\sim 1.913$ . The potential  $\hat{V}$  of a neutron in the magnetic field arising from an electron dipole moment  $\boldsymbol{\mu}_e$  positioned at  $\mathbf{r}$  is

$$\begin{aligned} \hat{V}(\mathbf{r}) &= -\mu_n[\mathbf{B}_S(\mathbf{r}) + \mathbf{B}_L(\mathbf{r})] \\ &= -\mu_n \frac{\mu_0}{4\pi} \left[ \nabla \times \left( \frac{\boldsymbol{\mu}_e \times \mathbf{r}}{r^3} \right) - \frac{2\mu_B}{\hbar} \frac{\mathbf{p} \times \mathbf{r}}{r^3} \right], \end{aligned} \quad (2.8)$$

where  $\boldsymbol{\mu}_e$  is the electrons's dipole moment  $-2\mu_B\mathbf{s}$ ,  $\mu_B$  is the Bohr magneton  $e\hbar/2m_e$ , and  $\mathbf{p}$  is the momentum of the electron. Two terms contribute to this potential:  $\mu_n\mathbf{B}_S(\mathbf{r})$  arises from the interaction with the spin of the electron and  $\mu_n\mathbf{B}_L(\mathbf{r})$  from the interaction with its orbital motion. Inserting this potential into Eq. (2.2) yields an expression for the neutron cross section due to magnetic scattering.

For a system with long-range magnetic order, the magnetic moments of the unpaired electrons tend to align spontaneously. Such materials behave as if a small magnetic moment were located at each atomic site with all the moments ordered in space. These moments give rise to Bragg diffraction of neutrons in the same manner as the nuclear interaction. A formula for the differential cross section, closely resembling the situation for nuclear scattering, can be derived for magnetic Bragg scattering

$$\left. \frac{d\sigma}{d\Omega} \right|_{\text{el}} = (\gamma r_0)^2 N_m \frac{(2\pi)^3}{v_{0m}} \sum_{\boldsymbol{\tau}_m} |F_M(\mathbf{Q})|^2 [1 - (\hat{\boldsymbol{\tau}}_m \cdot \hat{\boldsymbol{\eta}})_{\text{av}}^2] \delta(\mathbf{Q} - \boldsymbol{\tau}_m), \quad (2.9)$$

where  $r_0 = \mu_0 e^2 / 4\pi m_e$  is the classical radius of an electron,  $N_m$  is the number of magnetic unit cells with volume  $v_{0m}$  in the sample,  $\boldsymbol{\tau}_m$  is a vector in the



reciprocal magnetic lattice, and  $\hat{\boldsymbol{\eta}}$  is the unit vector in the mean direction of the spins.  $F_M$  is the magnetic structure factor given by

$$F_M(\mathbf{Q}) = \frac{1}{2}g \langle S^\eta \rangle F(\mathbf{Q}) \sum_d \sigma_d e^{-W_d} \exp(i\mathbf{Q} \cdot \mathbf{d}), \quad (2.10)$$

where  $g$  is the Landé splitting factor,  $\langle S^\eta \rangle$  is the staggered mean spin,  $F(\mathbf{Q})$  is the magnetic form factor, and  $\sigma_d$  gives the direction of the spins in the magnetic unit cell. The terms  $\langle S^\eta \rangle$  and  $1 - (\hat{\boldsymbol{\tau}}_m \cdot \hat{\boldsymbol{\eta}})_{\text{av}}^2$  enable one to determine the ordered moment size and the orientation of the ordered spin, respectively. The magnetic equivalent to the nuclear scattering length  $b$  is implicitly defined in Eqs. (2.9) and (2.10), i.e., the magnetic scattering amplitude of an atomic spin  $\langle S^\eta \rangle$  is

$$p = \frac{1}{2}g(\gamma r_0)^2 \langle S^\eta \rangle F(\mathbf{Q}) \sim 0.54 \langle S^\eta \rangle F(\mathbf{Q}) \times 10^{-14} \text{ m}, \quad (2.11)$$

which is of the same order of magnitude as the nuclear scattering length.

It is instructive to express the magnetic cross section [Eq. (2.2)] in terms of time-dependent spin operators, especially for the discussion of magnetic excitations. The partial differential cross section for scattering of the neutrons by electrons is

$$\frac{d^2\sigma}{d\Omega_f dE_f} = r_0^2 \frac{k_f}{k_i} S(\mathbf{Q}, \omega), \quad (2.12)$$

where the response function  $S(\mathbf{Q}, \omega)$  is

$$S(\mathbf{Q}, \omega) = \sum_{\lambda_i, \lambda_f} p_{\lambda_i} \langle \lambda_i | \hat{\mathbf{Q}}_\perp^\dagger | \lambda_f \rangle \langle \lambda_f | \hat{\mathbf{Q}}_\perp | \lambda_i \rangle \delta(\hbar\omega + E_{\lambda_i} - E_{\lambda_f}). \quad (2.13)$$

Here the operator  $\hat{\mathbf{Q}}_\perp$ , which describes the neutron-matter interaction, is defined by

$$\hat{\mathbf{Q}}_\perp(\mathbf{Q}) = \sum_i \exp(i\mathbf{Q} \cdot \mathbf{r}_i) \left( \frac{\mathbf{Q} \times (\mathbf{s}_i \times \mathbf{Q})}{Q^2} - \frac{i}{\hbar} \frac{\mathbf{Q} \times \mathbf{p}_i}{Q^2} \right), \quad (2.14)$$

where the sum includes all unpaired electrons (not to be confused with  $\mathbf{Q} = \mathbf{k}_i - \mathbf{k}_f$ ). The two terms in  $\hat{\mathbf{Q}}_\perp$  are the spin and orbital contribution to the magnetic scattering [compare with Eq. (2.8)]. Writing the delta function in Eq. (2.13) in terms of an integral representation results in the response function  $S(\mathbf{Q}, \omega)$  reduced to the Fourier transform of the correlation function  $\langle \hat{\mathbf{Q}}_\perp^\dagger(0) \cdot \hat{\mathbf{Q}}_\perp(t) \rangle$  [40]:

$$S(\mathbf{Q}, \omega) = \frac{1}{2\pi\hbar} \int_{-\infty}^{\infty} dt \exp(-i\omega t) \langle \hat{\mathbf{Q}}_\perp^\dagger(0) \cdot \hat{\mathbf{Q}}_\perp(t) \rangle. \quad (2.15)$$

In the case of spin-only scattering the second part of Eq. (2.14) is zero. The response function for the scattering of neutrons is then

$$S(\mathbf{Q}, \omega) = \left[ \frac{1}{2} g F(\mathbf{Q}) \right]^2 \sum_{\alpha, \beta} \left( \delta_{\alpha\beta} - \frac{Q_\alpha Q_\beta}{Q^2} \right) S^{\alpha\beta}(\mathbf{Q}, \omega), \quad (2.16)$$

where

$$S^{\alpha\beta}(\mathbf{Q}, \omega) = \frac{1}{2\pi\hbar} \int_{-\infty}^{+\infty} dt \sum_{\mathbf{r}} \exp[i(\mathbf{Q} \cdot \mathbf{r} - \omega t)] \langle \hat{S}^\alpha(0, 0) \hat{S}^\beta(\mathbf{r}, t) \rangle. \quad (2.17)$$

Here  $\alpha$  and  $\beta$  refer to the Cartesian coordinates  $x$ ,  $y$ , and  $z$  of the spin polarisation vector. The response function  $S(\mathbf{Q}, \omega)$ , often referred to as the dynamic structure factor, is the Fourier transform in both space and time of the spin-spin correlation function  $\langle \hat{S}^\alpha(0, 0) \hat{S}^\beta(\mathbf{r}, t) \rangle$ .

### 2.2.3 Neutron scattering instruments

In the course of our investigation several instruments were employed to reveal the magnetic properties of  $\text{Ca}_{0.83}\text{CuO}_2$ ,  $\text{Sr}_{0.73}\text{CuO}_2$ , and  $\text{LaTiO}_3$ .

Concerning neutron diffraction of  $\text{Ca}_{0.83}\text{CuO}_2$  and  $\text{Sr}_{0.73}\text{CuO}_2$ , experiments were performed on three different powder diffractometers: on the cold neutron powder diffractometer DMC installed at the neutron spallation source SINQ of the Paul Scherrer Institute, Villigen, Switzerland [41], on the high-resolution diffractometer D1A [42], and on the diffractometer D1B [43], both at the high-neutron-flux reactor of the Institute Laue Langevin, Grenoble, France.

The cold neutron diffractometer DMC is particularly useful to search for magnetic Bragg peaks, expected to be most dominant at small  $Q$  values, as it allows the use of high-wavelength neutrons (typically  $\lambda \sim 4 \text{ \AA}$ ). Moreover, this instrument has an extremely low background because of an oscillating radial collimator. D1B installed at the ILL is a spectrometer dedicated to diffraction experiments that call for a high neutron flux. This was essential for the determination of the temperature dependence of the small magnetic Bragg peaks with good statistics in a reasonable time frame.

For the inelastic neutron scattering experiments we made use of two time-of-flight instruments. Scattering data were collected using the high-energy transfer chopper spectrometer (HET) at the ISIS pulsed neutron facility at the Rutherford Appleton Laboratory, Chilton, Oxfordshire, United Kingdom [44]. Additional experiments have been performed at the cold neutron multi-chopper spectrometer IN5 installed at the Institute Laue Langevin, Grenoble, France [45].

We used time-of-flight instruments for our investigation because they allow a large region of the  $Q$ - $E$  space to be imaged simultaneously. The HET spectrometer is one of the best instruments available for this experiment. The arrangement of the detectors is optimised for the investigation of magnetic scattering. Moreover, the high incident energies available ( $E_i = 15$  to 2000 meV) allow the measurement of a wide kinematic range. The cold neutron instrument IN5 is a general-purpose time-of-flight spectrometer with an upper limit of the incident energy of  $E_i \sim 15$  meV.

Neutron diffraction of  $\text{LaTiO}_3$  was performed at the thermal neutron single-crystal diffractometer D15 at the Institute Laue Langevin, Grenoble, France [46].

# Chapter 3

## Quasi-1D $\text{Sr}_{0.73}\text{CuO}_2$

### 3.1 Introduction

One-dimensional (1D) spin  $S = 1/2$  systems with antiferromagnetic (AF) interactions have attracted considerable interest owing to the quantum mechanical nature of their ground state. Because of their enhanced quantum fluctuations in 1D, these systems exhibit many distinctive magnetic phenomena, which have no counterpart at higher dimensions. Examples are the Haldane gap in Heisenberg chains with integer spins [11], the spin–Peierls transition in Cu spin chains of  $\text{CuGeO}_3$  [47], and the energy gap in the spin excitation spectrum of two-leg ladders (pairs of  $\text{CuO}_2$  chains linked by oxygen atoms) [15, 48]. An important issue in the discussion of all these quasi-1D systems is the effect of hole doping. It was predicted, for example, that charge carriers doped into the two-leg ladders may lead to a superconducting or charge density wave state [49].

Recently, hole doping of Cu spin chains was achieved in  $\text{Sr}_{14}\text{Cu}_{24}\text{O}_{41}$  [50, 51]. The structure of  $\text{Sr}_{14}\text{Cu}_{24}\text{O}_{41}$  consists of two distinct Cu–O subcells (Fig. 1.2) [52, 53]. One contains  $\text{CuO}_2$  chains in which the copper ions are coupled by nearly  $90^\circ$  Cu–O–Cu bonds, the other consists of  $\text{Cu}_2\text{O}_3$  two-leg ladders. Superconductivity associated with these ladders was found under high pressure in  $\text{Sr}_{0.4}\text{Ca}_{13.6}\text{Cu}_{24}\text{O}_{41.84}$  ( $T_c \sim 12$  K) [20, 21]. Magnetic susceptibility measurements indicated that the holes are most probably located in the chains ( $\sim 0.6$  holes/Cu) [51]. Each hole causes approximately one  $\text{CuO}_2$  unit to become nonmagnetic due to Zhang–Rice singlet formation [17, 18]. These highly doped spin chains showed an energy gap in the spin excitation spectrum, which was attributed to dimerisation of the AF chain [54]. However, the presence of both ladders and chains in  $\text{Sr}_{14}\text{Cu}_{24}\text{O}_{41}$

was found to complicate an unambiguous interpretation of the experimental data. Whereas holes seemed more likely to go into the chains [51], it is still controversial how many of them move onto the ladders [55]. The respective role of ladders and chains could be understood better if one would be able to study their properties separately.

It is the aim of this chapter to serve as a stimulus and guide for other experiments discussed in this thesis and, more generally, for the discussion of the magnetic correlations of  $\text{Cu}^{2+}$   $S = 1/2$  spins in highly hole-doped  $\text{CuO}_2$  chains. Measurements of the static magnetic susceptibility of the quasi-1D cuprate  $\text{Sr}_{0.73}\text{CuO}_2$  are reported. The structure of this cuprate comprises  $\text{CuO}_2$  chains (average Cu valency 2.54+), inherently doped with  $\sim 0.6$  holes per Cu, alternating with Sr layers. The  $\text{CuO}_2$  chains with approximately  $90^\circ$  Cu–O–Cu bonds closely resemble the chains in  $\text{Sr}_{14}\text{Cu}_{24}\text{O}_{41}$ . Thus,  $\text{Sr}_{0.73}\text{CuO}_2$  provides a unique opportunity to study the properties of hole-doped spin chains without complications arising from the presence of spin ladders.

Our  $\text{Sr}_{0.73}\text{CuO}_2$  samples were prepared from a precursor containing a mixture of  $\text{SrCuO}_2$  and  $\text{CuO}$ . The polycrystalline samples are sintered at high oxygen pressure,  $P_{\text{O}_2} \sim 2000$  bar, and  $T = 1020^\circ\text{C}$  for 36 h [27, 56]. The structure of  $\text{Sr}_{0.73}\text{CuO}_2$  is shown in Fig. 3.1.  $\text{Sr}_{0.73}\text{CuO}_2$  consists of two almost independent sublattices: (i) an orthorhombic C-centred sublattice of Sr atoms with  $a = 3.7343(5)$  Å,  $b = 6.817(1)$  Å,  $c = 5.509(1)$  Å, and (ii) an F-centred sublattice of Cu and O atoms forming infinite 1D edge-sharing chains with  $a = 2.7246(3)$  Å,  $b = 6.817(1)$  Å, and  $c = 11.017(2)$  Å. The lattice is incommensurate in the  $a$ -direction because the translation period of the Sr sublattice does not match that of the Cu–O sublattice. The copper and oxygen atom positions are wave-modulated in the  $a$ -direction, with a wavelength of about 10 Å and an amplitude of 0.35 Å. The Cu ions are coupled by  $93.2(5)^\circ$  Cu–O–Cu bonds [Fig. 3.1(b)]. Under the assumption that the cation sites are fully occupied, the Sr content is given by the ratio of the  $a$  lattice parameters of the Sr and Cu–O subcells. The Sr content in this case is 0.73, but ranges in ceramic material from 0.72 to 0.74 depending on the exact growth conditions. Assuming a strontium content of 0.73, the oxygen content was measured to be 1.996(2) by the volumetric determination method [57]. Bearing these issues in mind, we will henceforth adhere to “ $\text{Sr}_{0.73}\text{CuO}_2$ ” as the composition under investigation in this thesis. More details of the synthesis and structural analysis of  $\text{Sr}_{0.73}\text{CuO}_2$  are given in Ref. [27]. The magnetisation was measured with a superconducting quantum interference device (SQUID) magnetometer (Biomagnetic Technologies Inc).

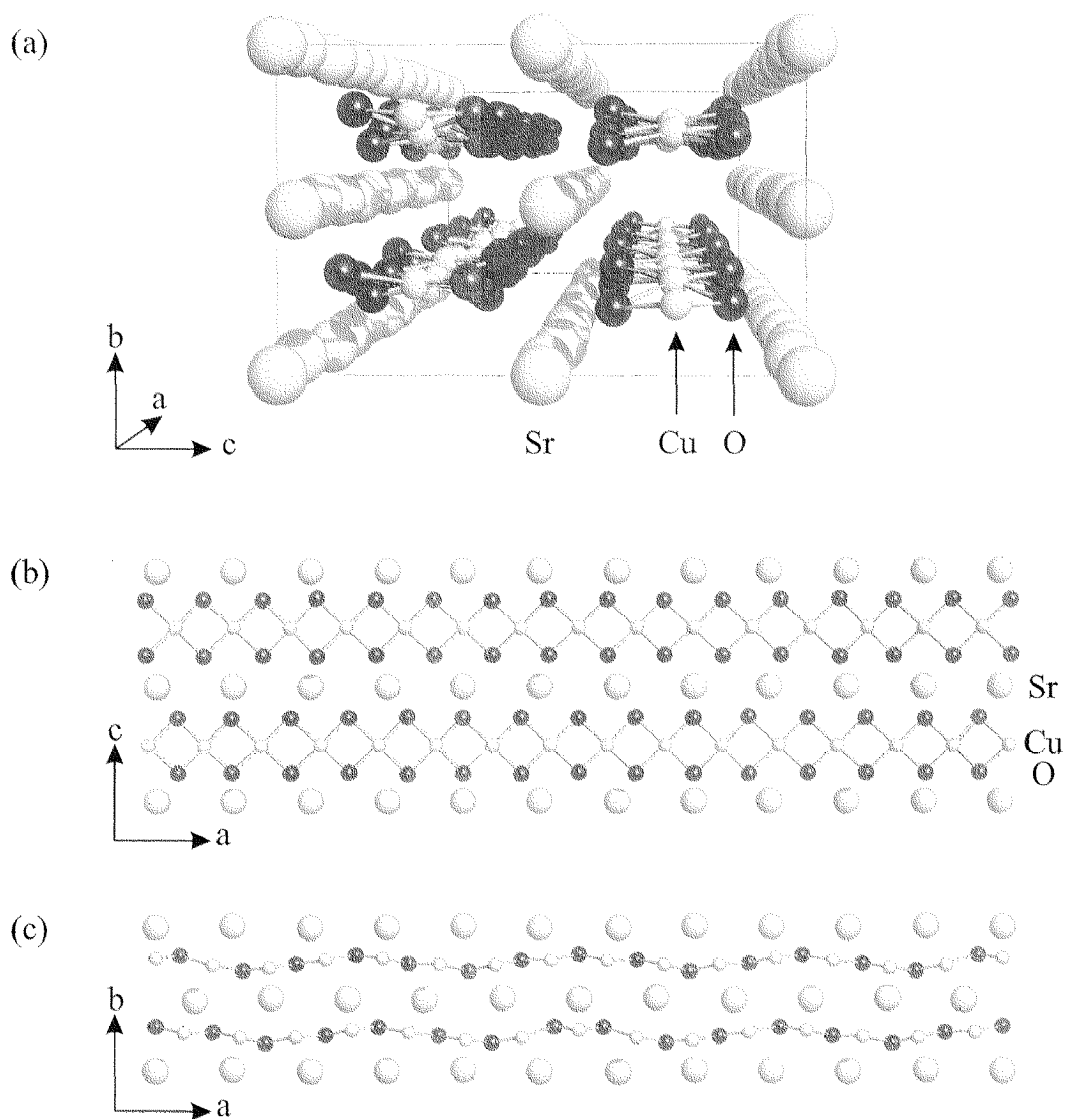


Figure 3.1: (a) Crystallographic structure of  $\text{Sr}_{0.73}\text{CuO}_2$  viewed in perspective along the  $\text{CuO}_2$  chains. Views along the  $b$  and  $c$  axes are shown separately in (b) and (c), respectively. For clarity only one anion and cation layer is displayed in (b) and (c).

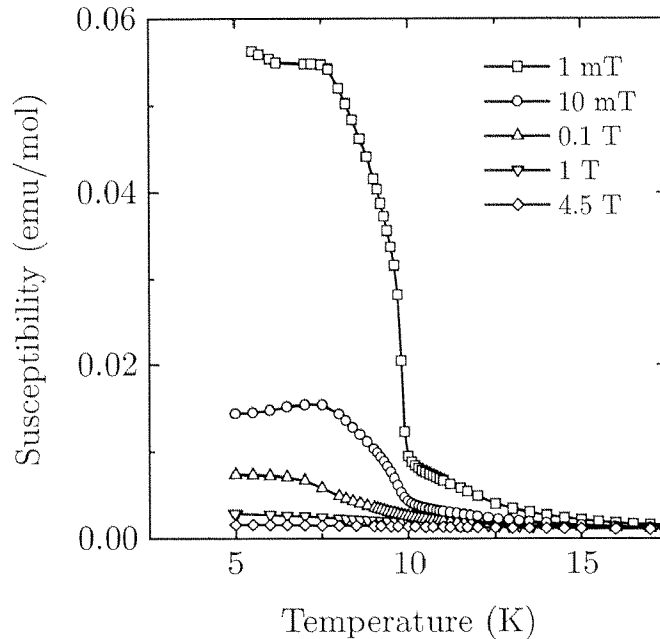


Figure 3.2: Field-cooled susceptibility of  $\text{Sr}_{0.73}\text{CuO}_2$  measured in different magnetic fields  $\mu_0 H$ .

## 3.2 Low-temperature magnetic order

Perhaps the most peculiar feature of  $\text{Sr}_{0.73}\text{CuO}_2$  is the small spontaneous ferromagnetic moment observed at low temperatures. Figure 3.2 displays the field-cooled susceptibility  $\chi(T)$  of polycrystalline  $\text{Sr}_{0.73}\text{CuO}_2$  at low temperatures measured in different magnetic fields. Below  $T \sim 10$  K, a sudden jump in the magnetisation is observed, indicating magnetic order. The transition is sharp at low fields and becomes broader and less pronounced at higher fields. The field dependence of the magnetisation is shown in Fig. 3.3. Above  $T \sim 20$  K,  $M(H)$  is linear, passes through the origin, and is reversible within experimental uncertainty. At lower temperatures,  $M(H)$  acquires a distinctly different character, exhibiting a very large derivative of the magnetisation  $dM/dH$  at low fields and a linear increase at higher fields. Moreover, the magnetisation shows a small hysteresis at low fields. The extrapolation of the linear behaviour observed at high field to  $\mu_0 H = 0$  T results in a ferromagnetic component  $M_s$  contributing to the magnetisation with a magnitude, which is strongly temperature dependent:  $M(T, H) = M_s(T, 0) + \chi H$ . Figure 3.4(a) illustrates the extrapolation of the high field magnetisation for the temperatures indicated. The temperature dependence of the ferromagnetic component  $M_s(T, 0)$  is presented in Fig. 3.4(b). With decreasing tempera-

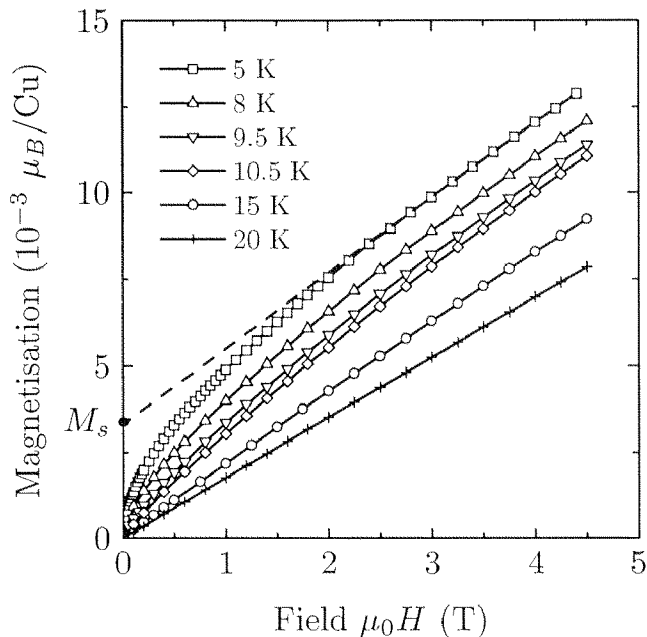


Figure 3.3: Magnetisation versus applied magnetic field at various temperatures. The ferromagnetic component to the magnetisation  $M_s$  is indicated for  $T = 5$  K.

ture  $M_s$  gradually appears below  $T \sim 20$  K, followed by a broad step-like increase of the saturation moment at  $T \sim 10$  K. Even at the lowest temperatures no saturation of  $M_s$  is observed. This suggests a spatial inhomogeneity of the moment size [58]. At  $T = 2$  K,  $M_s$  corresponds to a ferromagnetic moment of  $4.0(2) \times 10^{-3} \mu_B/\text{Cu}$ .

The magnetic susceptibility measurements presented above provide evidence that a magnetically ordered state with a small spontaneous ferromagnetic moment  $M_s \sim 4.0(2) \times 10^{-3} \mu_B/\text{Cu}$  is formed in  $\text{Sr}_{0.73}\text{CuO}_2$  below  $T_{\text{AF}} \sim 10$  K. It is only a weak but finite magnetic coupling between adjacent chains that can be held responsible for the occurrence of magnetic order because in all strictly 1D spin systems, magnetic order would be suppressed by quantum fluctuations [3]. At this point it is worth noting that a weak-ferromagnetic moment with  $M_s \sim 10^{-3} \mu_B/\text{Cu}$  was observed in the 2D AF copper oxides  $\text{La}_2\text{CuO}_4$  [59] and  $\text{Gd}_2\text{CuO}_4$  [60] too. In these compounds, and presumably also in  $\text{Sr}_{0.73}\text{CuO}_2$ , the weak-ferromagnetic moments arise from spin-canted antiferromagnetism, which requires a Dzyaloshinski–Moriya



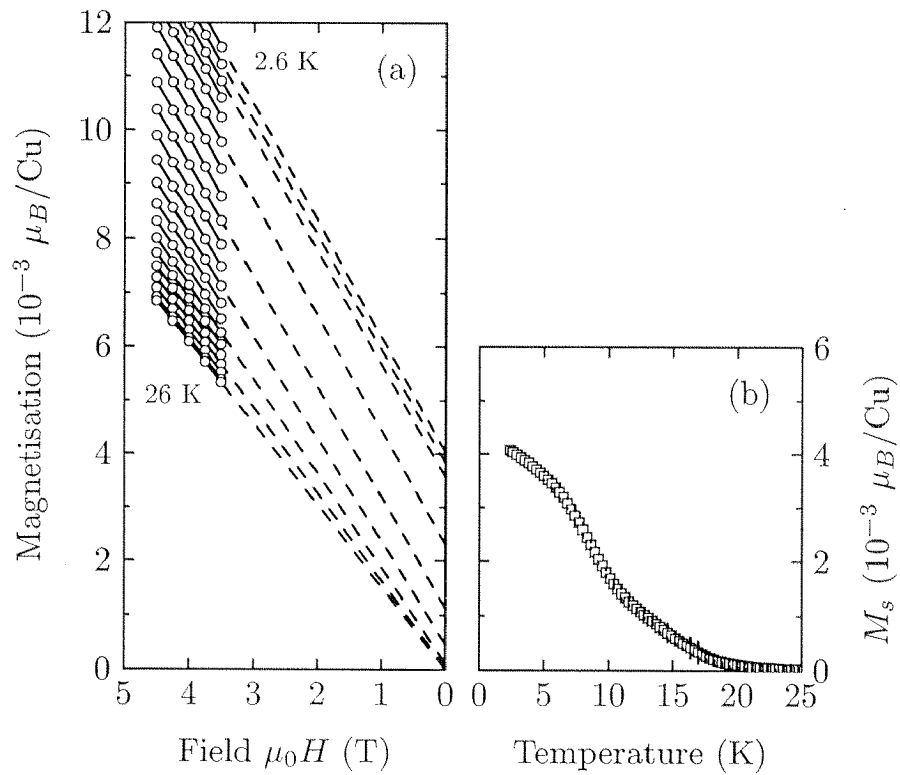


Figure 3.4: (a) High-field magnetisation of  $\text{Sr}_{0.73}\text{CuO}_2$  for  $T = 2.6$  K to  $T = 26$  K in steps of  $\Delta T = 1.2$  K. The dashed lines represent extrapolations of the high-field data for the determination of the weak-ferromagnetic saturation moment  $M_s(H = 0)$ . (b) Temperature dependence of  $M_s$ .

antisymmetric exchange interaction

$$\mathcal{H}_{\text{DM}} = \sum_{\langle i,j \rangle} \mathbf{D}_{ij} \cdot (\mathbf{S}_i \times \mathbf{S}_j) \quad (3.1)$$

in the spin Hamiltonian [61, 62]. Here  $\langle i, j \rangle$  denote the nearest-neighbour sites. It is known that the leading-order magnetic anisotropy in several cuprates arises from this interaction. The Dzyaloshinski–Moriya interaction causes the spins on the two sublattices that are aligned antiparallel to each other due to an AF exchange interaction  $\langle J \rangle_{\text{av}}$  to cant by a small angle  $\theta = D/\langle J \rangle_{\text{av}}$ , i.e., they possess a spontaneous weak ferromagnetic component. This is because the antisymmetric coupling energy is minimized when the two adjacent spins  $\mathbf{S}_i$  and  $\mathbf{S}_j$  are perpendicular to each other. The Dzyaloshinski–Moriya term is only allowed in asymmetric crystal structures. The essential requirement for this anisotropic exchange term is the absence of a centre of symmetry between the magnetic sites  $\mathbf{S}_i$  and  $\mathbf{S}_j$ . If such a centre existed,  $\mathbf{S}_i$  and  $\mathbf{S}_j$  would interchange in the symmetry operation of inversion and  $\mathbf{S}_i \times \mathbf{S}_j$  would change sign (with  $\mathbf{D}_{ij} = 0$  as the consequence). As mentioned above, the  $\text{CuO}_2$  chains in  $\text{Sr}_{0.73}\text{CuO}_2$  are wave modulated along the  $a$  axis, forming infinite corrugated ribbons. This causes the crystal symmetry to be low enough to contribute to the magnetic anisotropy by allowing an antisymmetric exchange to occur. The order of magnitude of the spin canting angle  $\theta$  in  $\text{Sr}_{0.73}\text{CuO}_2$  can be estimated from the moment  $M_s$ . If we assume that the order moment of  $\text{Cu}^{2+}$   $\langle S^\eta \rangle$  is reduced from  $1 \mu_B/\text{Cu}$  by a factor of  $\sim 5$  for quantum renormalisation (anticipating discussion in Chapter 5), the canting angle at  $T = 2$  K is

$$\theta = \frac{M_s}{\langle S^\eta \rangle} \sim 1^\circ. \quad (3.2)$$

### 3.3 Paramagnetic regime

Let us now continue with the temperature dependence of magnetic susceptibility  $\chi(T)$  in the paramagnetic regime. Figure 3.5 displays  $\chi(T)$  data of  $\text{Sr}_{0.73}\text{CuO}_2$  above  $T = 15$  K measured in an applied field of  $\mu_0 H = 1$  T. The susceptibility shows a broad plateau near  $T \sim 80$  K, followed by a strong enhancement of the susceptibility below  $T \sim 50$  K presumably originating from a Curie–Weiss-like component. This plateau resembles the rounded maximum observed in  $\text{Sr}_{14}\text{Cu}_{24}\text{O}_{41}$ , which was ascribed to dimer formation of  $\text{Cu}^{2+}$  spins [50, 51]. In  $\text{Sr}_{0.73}\text{CuO}_2$ , the gap-like behaviour is significantly smeared and a large Curie component masks the low-temperature behaviour

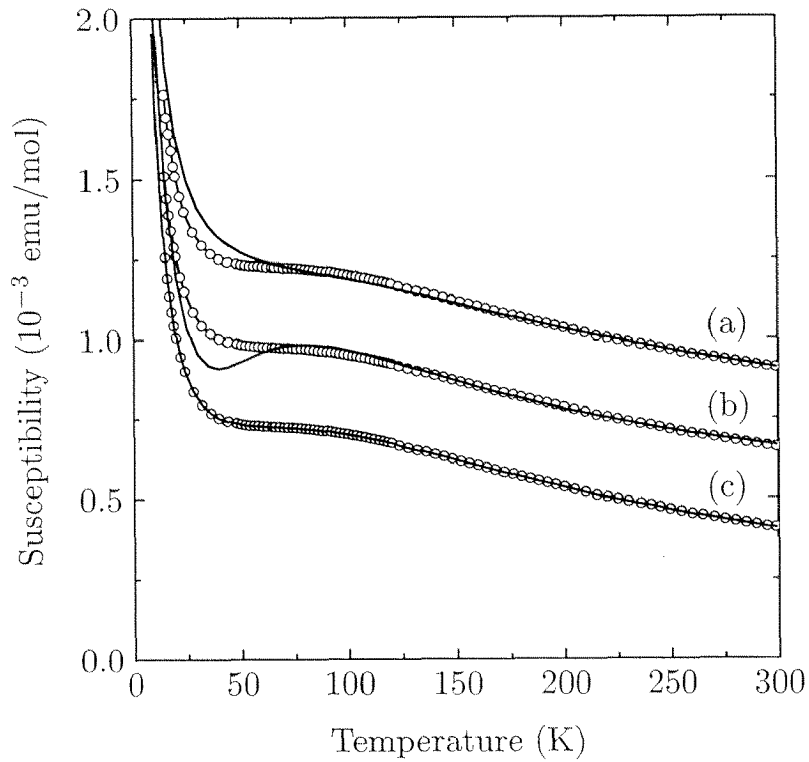


Figure 3.5: Temperature dependence of the magnetic susceptibility of  $\text{Sr}_{0.73}\text{CuO}_2$  at  $\mu_0 H = 1$  T. The solid lines represent fits of the susceptibility data to (a) homogeneous Heisenberg chain  $\mathcal{H} = J \sum_i \mathbf{S}_i \cdot \mathbf{S}_{i+1}$ , (b) isolated dimer chain  $\mathcal{H} = J \sum_i \mathbf{S}_{2i} \cdot \mathbf{S}_{2i+1}$ , and (c) alternating Heisenberg chain  $\mathcal{H} = J \sum_i (\mathbf{S}_{2i} \cdot \mathbf{S}_{2i+1} + \alpha \mathbf{S}_{2i} \cdot \mathbf{S}_{2i-1})$ . The data for (a) and (b) are offset by  $0.5 \times 10^{-3}$  emu/mol and  $0.25 \times 10^{-3}$  emu/mol, respectively.

instead. Such smearing was also observed in  $\text{Sr}_{14}\text{Cu}_{24}\text{O}_{41}$  with oxygen non-stoichiometry [63] or when doped with Ca [55]. Whereas the broad peak is characteristic for a 1D Heisenberg antiferromagnet [64, 65, 66], the Curie-like increase at low temperatures may arise from finite length chains with an odd number of spins [64], isolated spins, and/or other paramagnetic impurities.

To analyse the susceptibility data  $\chi(T)$  of  $\text{Sr}_{0.73}\text{CuO}_2$  quantitatively, taking into account possible singlet correlations below  $T \sim 100$  K, we consider the 1D Heisenberg antiferromagnet with alternating exchange couplings. The Hamiltonian for this model in which dimerisation can occur is given by

$$\mathcal{H} = J \sum_i (\mathbf{S}_{2i} \cdot \mathbf{S}_{2i+1} + \alpha \mathbf{S}_{2i} \cdot \mathbf{S}_{2i-1}), \quad (3.3)$$

where  $J$  is the exchange interaction between a spin and its right neighbour ( $J > 0$  for AF exchange) and  $\alpha J$  is the exchange interaction between a spin and its left neighbour [65, 66]. The parameter  $\alpha$  is a measure of the degree of alternation. For  $\alpha = 1$ , Eq. (3.3) represents a homogeneous chain  $\mathcal{H} = J \sum_i \mathbf{S}_i \cdot \mathbf{S}_{i+1}$  [67]. In the limit  $\alpha = 0$ , the system breaks up into an assembly of noninteracting spin pairs (dimers) with an exchange interaction  $J$  between the two spins forming the dimer,  $\mathcal{H} = J \sum_i \mathbf{S}_{2i} \cdot \mathbf{S}_{2i+1}$ . In Fig. 3.6 the normalised theoretical susceptibility  $\chi J / N g^2 \mu_B^2$  versus  $k_B T / J$  for different  $\alpha$  is reproduced, where  $N$  is the number of spins per site ( $N = 1$  if chains are undoped),  $g$  is the Landé  $g$ -factor, and  $k_B$  is the Boltzmann constant. These curves have been taken from the references cited in the figure caption. The position in temperature of the maximum in  $\chi$  depends on the exchange constant  $J$  only, i.e., is independent of  $\alpha$ . This allows us to fix the energy scale of the experimental system. For the alternating chains ( $\alpha < 1$ ), an excitation gap always exists in the excitation spectrum. In this case, the spins will populate the nonmagnetic ground state with decreasing temperature, which causes an exponential decrease of magnetic susceptibility. At absolute zero, therefore, the susceptibility vanishes for any  $\alpha < 1$ . The uniform chain, however, has a finite density of low-lying excited states arbitrarily close to the ground state, and correspondingly a non-zero susceptibility.

It is worthwhile spending a moment to justify the use of the Heisenberg model Eq. (3.3). The assumption that the insulator  $\text{Sr}_{0.73}\text{CuO}_2$  is to a large extent a one-dimensional magnetic system can be perceived “at first glance” at the structure of this material (Fig. 3.1). We should bear in mind, though, that strictly speaking it is a 3D assembly of loosely coupled chains. The isotropic Heisenberg character of the exchange in  $\text{Sr}_{0.73}\text{CuO}_2$  can be inferred by the temperature dependence of the  $g$ -factor. The  $g$ -factor  $g = 2.08$  measured by electron paramagnetic resonance (EPR) was found to be temperature independent in the region  $15 < T < 300$  K [32]. If anisotropic

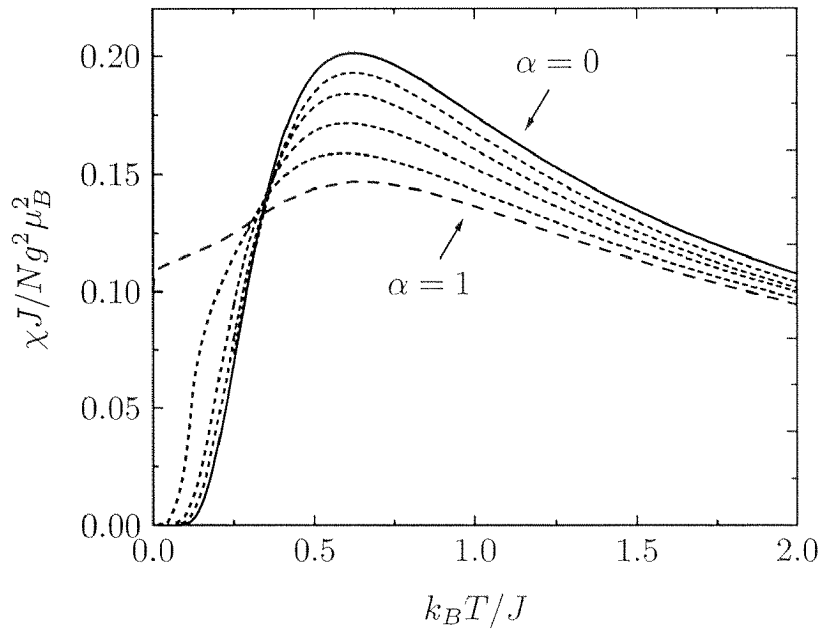


Figure 3.6: Temperature dependence of the normalised magnetic susceptibility  $\chi J / N g^2 \mu_B^2$  versus  $k_B T / J$  for the alternating chain Heisenberg model  $\mathcal{H} = J \sum_i (\mathbf{S}_{2i} \cdot \mathbf{S}_{2i+1} + \alpha \mathbf{S}_{2i} \cdot \mathbf{S}_{2i-1})$ . The solid line is the exact result for the susceptibility of isolated dimers ( $\alpha = 0$ ). The dotted lines represent the susceptibility for coupled dimers, with  $\alpha = 0.2, 0.4, 0.6,$  and  $0.8$  [65, 66]. The dashed line is the homogeneous chain ( $\alpha = 1$ ) [68, 69].

components would exist in the spin-spin coupling of  $\text{Sr}_{0.73}\text{CuO}_2$  (exchange and/or dipole), a shift in the  $g$ -factor would have occurred to reflect the onset of long- or short-range order [70]. Furthermore, no single-ion anisotropy is expected as  $\text{Cu}^{2+}$  is a spin  $S = 1/2$  ion. The Dzyaloshinski–Moriya interaction [Eq. (3.1)], introduced in Section 3.2 to explain the weak-ferromagnetic moment below  $T \sim 10$  K, constitutes another mechanism that may introduce anisotropy but is negligible in this context. A meaningful approximation of the order of magnitude of this interaction is  $\mathcal{H}_{\text{DM}} \sim \theta J \sim 0.02J$ , where  $\theta$  is the canting angle [Eq. (3.2)] of the AF lattice in the ordered state. Alternatively, the bound imposed on the anisotropic components of the exchange estimated from the  $g$ -factor is  $\mathcal{H} \lesssim J(g - 2)/g \sim 0.04J$ . As a consequence, the applicability of the Heisenberg chain model is justified.

To separate the susceptibility expected for the idealised alternating Heisenberg chains from the Curie–Weiss term observed at low temperatures, we will use

$$\chi(T) = \chi_0 + \chi_{\text{CW}}(T) + \chi_{\text{chain}}(T), \quad (3.4)$$

where  $\chi_0$  is the sum of the temperature-independent core diamagnetic and Van Vleck terms,  $\chi_{\text{CW}}(T)$  is the Curie–Weiss term

$$\chi_{\text{CW}} = \frac{N_f g^2 \mu_B^2 S(S+1)}{3k_B(T - \Theta)}, \quad (3.5)$$

where  $N_f$  is the number of “free”  $\text{Cu}^{2+}$   $S = 1/2$  spins,  $g = 2.08$  [32],  $\mu_B$  is the Bohr magneton,  $k_B$  is the Boltzmann constant, and  $\chi_{\text{chain}}(T)$  is the susceptibility of the 1D Heisenberg antiferromagnet.

A logical first step to analyse the susceptibility data of  $\text{Sr}_{0.73}\text{CuO}_2$  is a fit taking for  $\chi_{\text{chain}}(T)$  the susceptibility for a  $S = 1/2$  infinite isotropic Heisenberg chain [ $\alpha = 1$  in Eq. (3.3)]. As yet there are no analytical solutions for the magnetic susceptibility of this model due to insurmountable mathematical problems associated with cooperative phenomena. Therefore, we must take recourse to a numerical approximation. A useful closed-form approximation to the numerical result of Bonner and Fisher [64] has been suggested to be

$$\chi_{\text{BF}}(T) = \frac{N_c g^2 \mu_B^2}{k_B T} \frac{0.25 + 0.07498x + 0.07524x^2}{1 + 0.99310x + 0.17214x^2 + 0.75783x^3}, \quad (3.6)$$

where  $N_c$  is the number of  $\text{Cu}^{2+}$  sites and  $x = J/k_B T$  [71]. A fit using this model is shown superimposed on the data as the line (a) in Fig. 3.5. The Bonner–Fisher curve could reproduce the data at high temperatures well

	Homogeneous Chain	Dimer Chain	Alternating Chain
$N_f$	0.048(1)	0.048(1)	0.048(1)
$\Theta(\text{K})$	0.42(2)	0.42(2)	0.42(2)
$N_c$	0.40(1)	0.32(2)	0.37(2)
$J/k_B(\text{K})$	173(8)	184(7)	174(8)
$\alpha$	1	0	0.5(1)
$\chi_0(\text{emu/mol})$	$0(2) \times 10^{-5}$	$0(1) \times 10^{-5}$	$3(1) \times 10^{-5}$

Table 3.1: Parameters obtained by fitting the susceptibility to the homogeneous Heisenberg chain [Eq. (3.6)], the dimer chain [Eq. (3.7)], and the alternating Heisenberg chain [Eq. (3.8)] (fitting curves in Fig. 3.5).  $N_f$  is the number of spins per f.u. with Weiss temperature  $\Theta$  contributing to the Curie–Weiss susceptibility  $\chi_{CW}$ .  $N_c$ ,  $J/k_B$ , and  $\alpha$  are determined from the fit to the three Heisenberg chain models.  $\chi_0$  is the temperature-independent term.

with parameters summarised in Table 3.1. However, the low-temperature data could not be fitted with the simple chain model.

The susceptibility data for Sr<sub>14</sub>Cu<sub>24</sub>O<sub>41</sub> [50, 51] was successfully described by taking for  $\chi_{\text{chain}}$  the susceptibility of isolated dimers [ $\alpha = 0$  in Eq. (3.3)] given by

$$\chi_d(T) = \frac{N_c g^2 \mu_B^2}{k_B T} \frac{1}{3 + \exp(J/k_B T)}, \quad (3.7)$$

where  $N_c$  is the number of spins forming a dimer (equals twice the number of dimers) and  $J$  is the exchange coupling between the spins forming the dimer. (Note that this is the susceptibility of the familiar singlet-triplet model.) Applied to our case, this model also provides a rather poor fit at low temperatures, as shown in Fig. 3.5(b) (fitting parameters in Table 3.1).

Then a coupling between dimers, i.e., a non-zero  $\alpha$  in Eq. (3.3), is taken into account. The polynomial function deduced in order to interpolate the numerical results of Bonner *et al.* [66] was used to reproduce  $\chi_{\text{chain}}(T)$  [72, 73]:

$$\chi_{\text{AHC}} = \frac{N_c g^2 \mu_B^2}{k_B T} \frac{A + Bx + Cx^2}{1 + Dx + Ex^2 + Fx^3}, \quad (3.8)$$

where  $x = J/k_B T$  and  $N_c$  is the number of Cu<sup>2+</sup> spins contributing to the chain susceptibility. The values of parameters  $A(\alpha)$ ,  $B(\alpha)$ ,  $\dots$ ,  $F(\alpha)$  were

calculated numerically [72]. A fit to the data using this alternating chain Heisenberg model is shown as line (c) in Fig. 3.5. Now the results of fitting are excellent over a wide temperature range for the parameters  $J/k_B = 174(8)$  K,  $\alpha = 0.5(1)$ ,  $N_c = 0.37(2)$  spins per formula unit (f.u.),  $N_f = 0.048(1)$  spins per f.u., and  $\Theta = 0.42(2)$  K, and  $\chi_0 = 3(1) \times 10^{-5}$  emu/mol. For these calculations,  $g = 2.08$  determined from electron paramagnetic resonance measurements was used [32].

The total spin density,  $N_c + N_f = 0.42(3)$  per f.u., is close to the expected  $\text{Cu}^{2+}$  concentration, which is 0.46 as derived from the formal valence of Cu ( $\text{Cu}^{2.54+}$ ). This means that each hole in the spin chain renders approximately one  $\text{CuO}_2$  unit nonmagnetic. This is consistent with assigning an effective  $\text{Cu}^{3+}$  ion in the low-spin  $S = 0$  state, and reflects the same microscopic physics as in hole-doped  $\text{CuO}_2$  layers [17]: The extra hole sits mainly on the O ions but is tightly bound in a Zhang–Rice singlet so that the  $\text{Cu}^{3+}$  ion is in a low-spin singlet state. Because one expects about two spins per five Cu atoms in the chain, a plausible explanation for the alternating Heisenberg chain behaviour is the pairing of dimers, which align periodically with a five-times interatomic spacing.

As mentioned above, the Curie–Weiss-type term can originate from several possible sources, including nearly isolated  $\text{Cu}^{2+}$  ions, some kind of lattice defects, or magnetic impurities. However, an equally plausible explanation is that the Curie-like behaviour originates from  $\text{CuO}_2$  1D chains, which are randomly terminated by oxygen defects (note that the oxygen content in “ $\text{Sr}_{0.73}\text{CuO}_2$ ” deviates slightly from 2; it was measured to be 1.996(2) [27]). If the resulting chain segments have an even number of  $\text{Cu}^{2+}$  spins, then the total spin on the chain in the ground state is zero at  $T = 0$ . If, however, the chains have an odd number of  $\text{Cu}^{2+}$  spins, then the net spin on the chain is 1/2 at low temperatures [64]. Such chains of odd length will make a contribution to the susceptibility, which are Curie–Weiss-like, although the amplitude of the susceptibility divergence is suppressed with increasing length by  $\text{Cu}^{2+}$ – $\text{Cu}^{2+}$  interactions [74].

It is very unusual that a highly diluted compound, where only about 40% of the Cu ions are magnetic, exhibits magnetic order at  $T_{\text{AF}} \sim 10$  K. This striking result will be discussed in more detail in Chapter 5. At this point it should be stressed the fact that, for example in the 2D Cu–O layers present in high- $T_c$  cuprates, no Néel order nor a static stripe phase yielding long-range magnetic order is found for doping levels exceeding  $\sim 0.04(2)$  and  $\sim 0.125$  holes/Cu, respectively [75]. Another interesting question could arise when describing the susceptibility data  $\chi(T)$  with the alternating chains Heisenberg model. Has  $\text{Sr}_{0.73}\text{CuO}_2$  indeed an energy gap in its spin excitation



spectrum? Within the context of the alternating Heisenberg chain model above discussed, a spin gap of  $\Delta \sim J(1 - \alpha/2 - 3\alpha^2/8) \sim 10$  meV would be predicted for the values  $J/k_B = 174$  K and  $\alpha = 0.5$  [76]. Clearly more information is needed to put this claim on a sure footing. In fact, it can only be verified by an elaborate study of the magnetic excitations by inelastic neutron scattering. We will discuss this in Chapter 6.

To summarise this chapter, we have examined the static magnetic properties of the hole-doped quasi-1D cuprate  $\text{Sr}_{0.73}\text{CuO}_2$  measured by magnetic susceptibility measurements. In contrast to  $\text{Sr}_{14}\text{Cu}_{24}\text{O}_{41}$ , this compound exhibits magnetic order with a small spontaneous ferromagnetic moment below  $T_{\text{AF}} \sim 10$  K [32]. This is surprising considering the fact that the spin system is highly diluted with nonmagnetic holes. To the best of my knowledge, this is the first example of a cuprate to show magnetic order when a substantial number of holes is introduced in the system. At higher temperatures,  $\text{Sr}_{0.73}\text{CuO}_2$  and  $\text{Sr}_{14}\text{Cu}_{24}\text{O}_{41}$  show similar magnetic properties. The magnetic susceptibility data are well described by the alternating chain Heisenberg model, which is the first indication of dimerisation of the Cu spins in the  $\text{CuO}_2$  chains.

# Chapter 4

## Quasi-1D $\text{Ca}_{0.83}\text{CuO}_2$

### 4.1 Introduction

This chapter will present the magnetic susceptibility of a series of polycrystalline  $\text{Ca}_{0.83}\text{CuO}_{2-\delta}$  samples with controlled oxygen content and on magnetic torque measurements taken on a single crystal [33]. This compound is to a certain degree isomorphous with  $\text{Sr}_{0.73}\text{CuO}_2$ . Both these compounds are based on two sublattices, which are incompatible along one crystallographic direction, resulting in essentially 1D incommensurate structures. The resemblance with  $\text{Sr}_{0.73}\text{CuO}_2$  is not complete however, because, although Sr and Ca are isovalent, the difference in ionic radii causes a change in all lattice parameters and displacement of O ions as well. Therefore, the cation/anion ratio in  $\text{Ca}_{0.83}\text{CuO}_2$  differs from that in  $\text{Sr}_{0.73}\text{CuO}_2$ . This causes a pronounced change in their physical properties as the spin density is changed drastically. One of the unique features of the compound under discussion in this chapter is that the hole doping in the chains can be varied with the oxygen content. As the holes are almost localised owing to large charge transfer gaps and small transfer integrals, only spin degrees of freedom survive at low temperatures. This raises the interesting question of how magnetic correlations in  $\text{Ca}_{0.83}\text{CuO}_{2-\delta}$  evolve as spins are extracted successively from  $\text{CuO}_2$  spin chains.

The structure of  $\text{Ca}_{0.83}\text{CuO}_2$  is shown in Fig. 4.1 [77, 78].  $\text{Ca}_{0.83}\text{CuO}_2$  consists of two almost independent sublattices: (i) an orthorhombic C-centred sublattice of Ca atoms with  $a = 3.3812(3)$  Å,  $b = 6.3217(7)$  Å,  $c = 5.295(1)$  Å, and (ii) an F-centred sublattice of Cu and O atoms with  $a = 2.7895(3)$  Å,  $b = 6.3207(8)$  Å, and  $c = 10.590(1)$  Å. The lattice is incommensurate in the  $a$ -direction because the translation period of the Ca sublattice

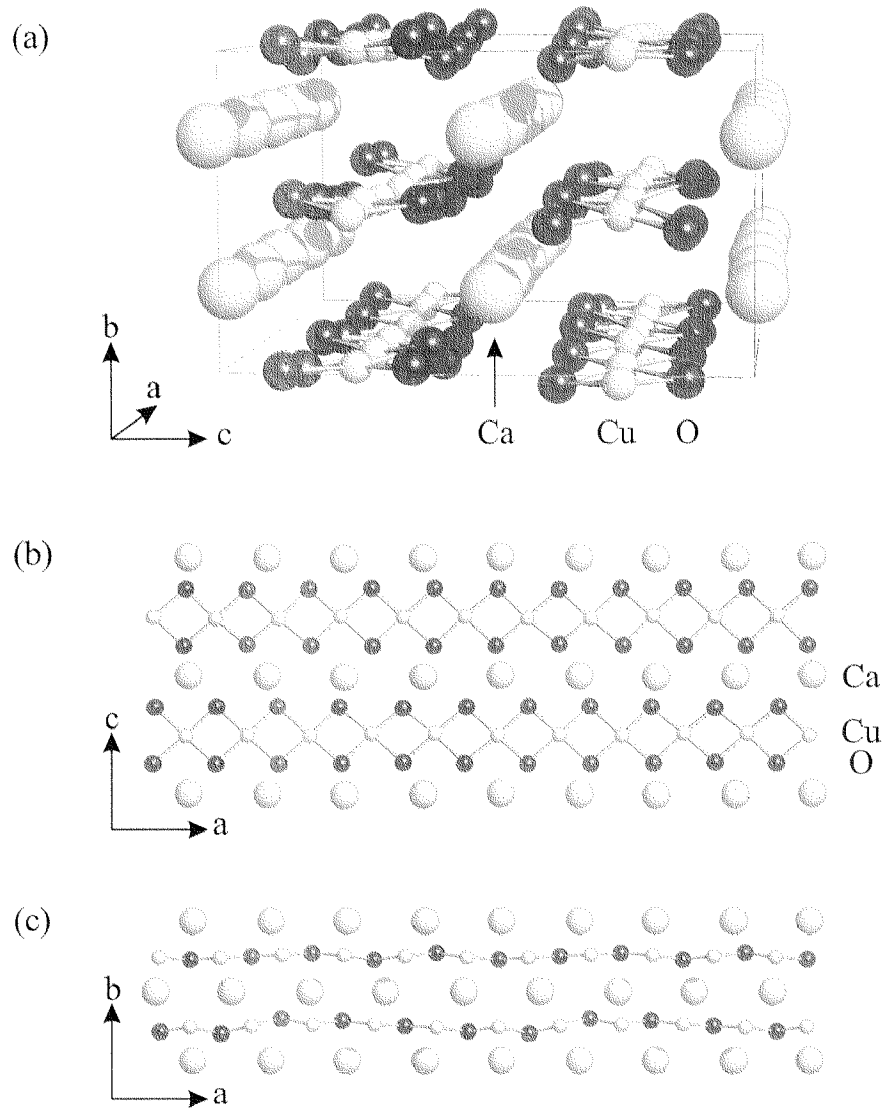


Figure 4.1: (a) Crystallographic structure of  $\text{Ca}_{0.83}\text{CuO}_2$  viewed in perspective along the  $\text{CuO}_2$  chains. Views along the  $b$  and  $c$  axes are shown separately in (b) and (c), respectively. For clarity only one anion and cation layer is displayed in (b) and (c).

Sample	Composition	$\delta$	Cu valence	$N$
A	$\text{Ca}_{0.83}\text{CuO}_{2.009}$	$-0.009(2)$	$\text{Cu}^{2.358(4)+}$	$0.64(1)$
B	$\text{Ca}_{0.83}\text{CuO}_{1.980}$	$0.020(4)$	$\text{Cu}^{2.300(8)+}$	$0.70(1)$
C	$\text{Ca}_{0.83}\text{CuO}_{1.965}$	$0.035(4)$	$\text{Cu}^{2.270(8)+}$	$0.73(1)$

Table 4.1: Composition of  $\text{Ca}_{0.83}\text{CuO}_{2-\delta}$  samples.  $\delta$  denotes the oxygen nonstoichiometry and  $N$  the nominal spin density per formula unit.

does not match that of the Cu–O sublattice. Therefore, the metal composition is uniquely related to the magnitude of the misfit.

The  $\text{Ca}_{0.83}\text{CuO}_2$  specimens used in this work were prepared from a precursor containing an appropriate mixture of  $\text{Ca}_2\text{CuO}_3$  and  $\text{CuO}$ . The single-phase polycrystalline samples are sintered at high oxygen pressure,  $P_{\text{O}_2} = 1740$  bar, and  $T = 1020^\circ\text{C}$  for 36 h. For single-crystal growth, a eutectic composition  $\text{BaCuO}_2 + \text{CuO}$  is used as a flux. Small single crystals grow from the melt at high argon pressure,  $P_{\text{Ar}} = 10$  kbar, and  $T = 1060^\circ\text{C}$  [56]. Volumetric oxygen content measurements [57] determined the exact O stoichiometry to be 2.009(2).

In addition, two  $\text{Ca}_{0.83}\text{CuO}_{2-\delta}$  samples with controlled oxygen content were prepared by annealing the as-prepared compound  $\text{Ca}_{0.83}\text{CuO}_{2.009}$  for 60 h in a 1-bar oxygen atmosphere at  $T = 650^\circ\text{C}$  and  $850^\circ\text{C}$ , respectively, in order to reduce their oxygen content. The oxygen nonstoichiometry is measured to be  $\delta = 0.020(4)$  and  $\delta = 0.035(4)$  using a highly sensitive thermogravimetric analyser and is confirmed by independent volumetric oxygen content determination. Assuming a formal valence of  $\text{Ca}^{2+}$  and  $\text{O}^{2-}$ , the average Cu valence in  $\text{Ca}_{0.83}\text{CuO}_{2-\delta}$  can be varied from  $\text{Cu}^{2.36+}$  [ $\delta = -0.009(2)$ ] to  $\text{Cu}^{2.27+}$  [ $\delta = 0.035(4)$ ], i.e., with increasing  $\delta$ , the number of spins in the chain is increased. The composition of the three samples investigated in this chapter is summarised in Table 4.1.

## 4.2 Magnetism vs. oxygen vacancies

The susceptibility  $\chi(T)$  of an as-prepared polycrystalline  $\text{Ca}_{0.83}\text{CuO}_{2.009}$  sample is shown in Fig. 4.2 for applied magnetic fields between  $\mu_0 H = 10$  mT and 4.5 T. In Fig. 4.3,  $\chi(T)$  of this sample is compared with the two other  $\text{Ca}_{0.83}\text{CuO}_{2-\delta}$  samples with  $\delta = 0.020(4)$  and  $\delta = 0.035(4)$ , respectively. The overall behaviour of  $\chi(T)$  is similar in the three  $\text{Ca}_{0.83}\text{CuO}_{2-\delta}$  compounds, in spite of the large change in their spin density. The suscepti-

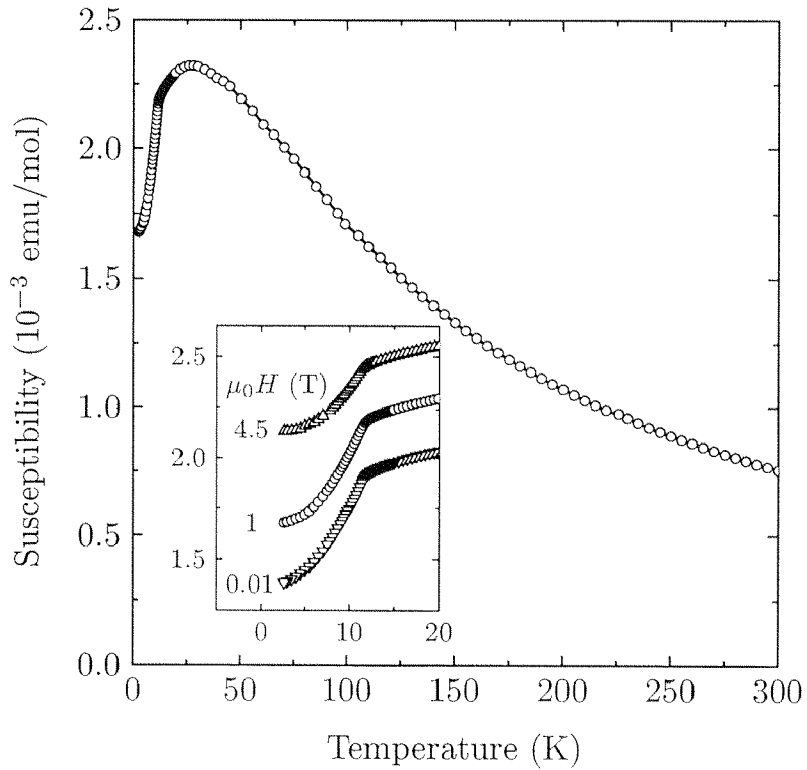


Figure 4.2: Susceptibility of as-prepared polycrystalline  $\text{Ca}_{0.83}\text{CuO}_{2.009}$  at  $\mu_0 H = 1$  T. Inset:  $\chi(T)$  for low temperatures at  $\mu_0 H = 10$  mT, 1 T, and 4.5 T. The  $\chi(T)$  curves at  $\mu_0 H = 10$  mT and 4.5 T are offset by  $-0.25 \times 10^{-3}$  emu/mol and  $0.25 \times 10^{-3}$  emu/mol, respectively. The value of  $\chi(T > 15$  K) is independent of the applied field.

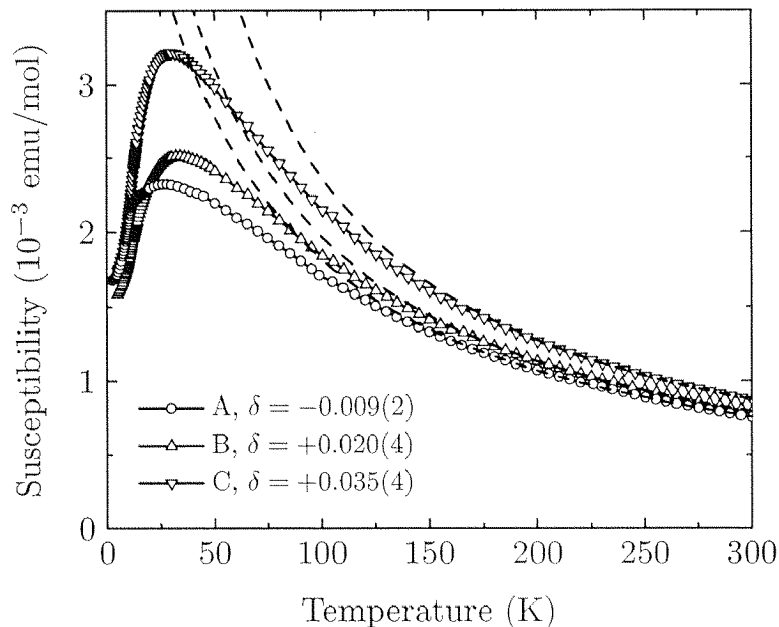


Figure 4.3: Susceptibility  $\chi(T)$  for  $\text{Ca}_{0.83}\text{CuO}_{2-\delta}$  at  $\mu_0 H = 1$  T versus doping. The dashed lines are fits of the Curie–Weiss law to the high temperature data.

bility increases with decreasing temperature towards a broad maximum at  $T \sim 30$  K, followed by a large decrease at low temperatures. The broad maximum indicates short-range AF correlations characteristic of low-dimensional Heisenberg antiferromagnets. The large decrease of  $\chi(T)$  between  $T = 30$  and 12 K suggests dominant singlet pairing at low temperatures. As the spin density  $N$  increases, the maximum in  $\chi(T)$  increases monotonically. Moreover, the temperature corresponding to the maximum in  $\chi(T)$  does not shift appreciably. At  $T = 12.2(1)$  K an abrupt drop in  $\chi(T)$  is observed, illustrated in the inset of Fig. 4.2, but  $\chi(T)$  remains finite at lower values of  $T$  [For  $\text{Ca}_{0.83}\text{CuO}_{2.009}$ ,  $\chi(2 \text{ K}) \sim 0.7 \chi(12 \text{ K})$ ]. Together with the field dependence of the magnetisation shown in Fig. 4.4, this observation indicates AF order rather than a spin–Peierls transition, below which  $\chi(T)$  would drop to zero (the large residual susceptibility at  $T \sim 2$  K cannot be attributed to a small Curie-like contribution). A spin-glass state can be ruled out because no hysteresis between the zero-field cooled and field cooled magnetisation is observed. Weak-ferromagnetism found in  $\text{Sr}_{0.73}\text{CuO}_2$  is also at odds with our data, as it would lead to an increase of  $\chi(T)$  below the transition. The unambiguous proof of AF order is obtained from the magnetic torque measurements described below and neutron diffraction experiments presented in

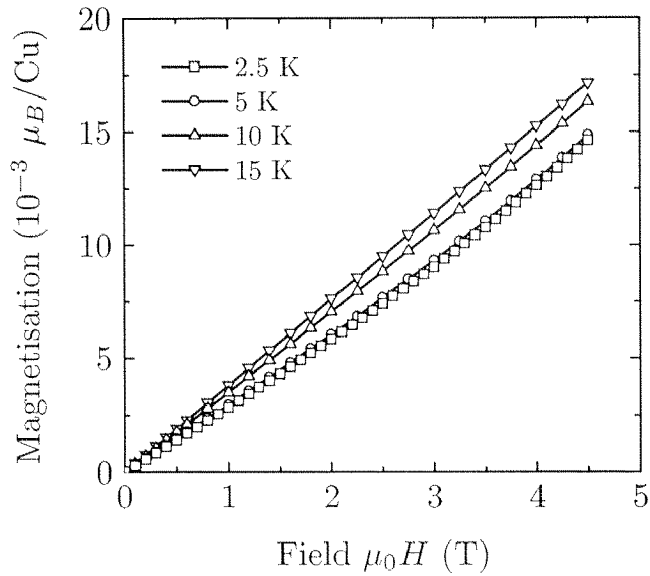


Figure 4.4: Magnetisation of  $\text{Ca}_{0.83}\text{CuO}_{2.009}$  versus applied magnetic field at indicated temperatures.

Chapter 5. The AF ordering temperature remains at  $T_{\text{AF}} = 12.2(1)$  K for all three samples. The interchain coupling is apparently not changed by introducing a different spin configuration in the chains; it depends mainly on the interchain distance. This statement is supported by the fact that the isomorphous materials,  $\text{Sr}_{0.73}\text{CuO}_2$  and  $\text{Ba}_{0.67}\text{CuO}_2$  [79], with larger cations and consequently larger lattice parameters have lower magnetic ordering temperatures,  $T \sim 10$  K [32] and  $T \sim 5$  K, respectively.

To extract the total spin density in  $\text{Ca}_{0.83}\text{CuO}_{2-\delta}$  from this data, the high-temperature susceptibility data  $\chi(T > 175$  K) is fitted with the Curie-Weiss law

$$\chi(T) = \frac{Ng^2\mu_B^2S(S+1)}{3k_B(T-\Theta)}, \quad (4.1)$$

where  $N$  is the total number of spins  $S = 1/2$  per formula unit (f.u.),  $g = 2.08$  [80],  $\mu_B$  is the Bohr magneton,  $k_B$  is the Boltzmann constant, and  $\Theta$  is the Weiss temperature. The fits for the three samples are indicated in Fig. 4.3 by dashed lines.  $N$  (noted as  $N_{\text{CW}}$  in Table 4.2) is found to be in good agreement with the hole doping expected from the chemical formula (noted as  $N$  in Table 4.2). This means that each hole in the  $\text{CuO}_2$  chain renders one  $\text{CuO}_2$  unit nonmagnetic, consistent with Zhang-Rice singlet formation.

Let us now examine the behaviour of  $\chi(T)$  for  $T < 175$  K. The data were fitted assuming two models taking into account possible singlet corre-

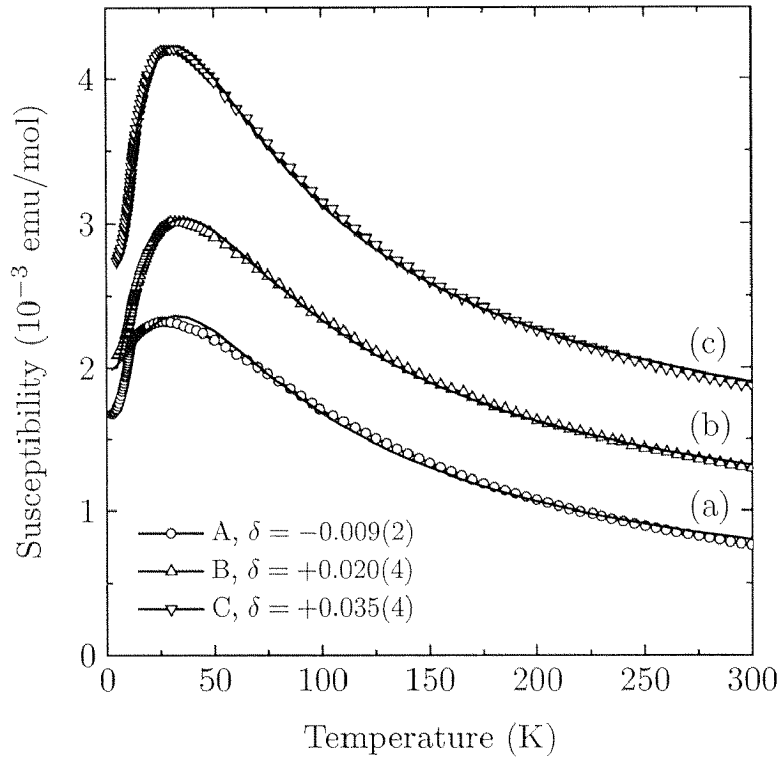


Figure 4.5: First approach; fit of the susceptibility  $\chi(T)$  for  $\text{Ca}_{0.83}\text{CuO}_{2-\delta}$  with alternating chain Heisenberg model [Eq. (4.2)]. (a)  $\text{Ca}_{0.83}\text{CuO}_{2.009}$ , (b)  $\text{Ca}_{0.83}\text{CuO}_{1.980}$ , and (c)  $\text{Ca}_{0.83}\text{CuO}_{1.965}$ . Curves for (b) and (c) are offset by  $0.5 \times 10^{-3}$  emu/mol and  $1 \times 10^{-3}$  emu/mol, respectively.

Sample	$N$	$N_{\text{CW}}$	$N_{\text{AC}}$	$J(\text{K})$	$\alpha$	$\chi_0(\text{emu/mol})$
A	0.64(1)	0.66(1)	0.54(2)	52(1)	0.98(5)	$1.8(5) \times 10^{-4}$
B	0.70(1)	0.69(1)	0.65(2)	57(2)	0.97(4)	$8(1) \times 10^{-5}$
C	0.73(1)	0.72(1)	0.78(2)	52(2)	0.90(2)	$6(1) \times 10^{-5}$

Table 4.2: Parameters for  $\text{Ca}_{0.83}\text{CuO}_{2-\delta}$ : the average number of spins per formula unit  $N$  is derived from the formal Cu valence.  $N_{\text{CW}}$  is obtained from a fit of  $\chi(T > 175 \text{ K})$  to the Curie-Weiss law.  $N_{\text{AC}}$ ,  $J/k_B$ ,  $\alpha$ , and  $\chi_0$  are parameters for the fit (Fig. 4.5) to the alternating chain Heisenberg model [Eq. (4.2)].



lations at low temperatures. Let us first consider, as in the analysis of the susceptibility data of  $\text{Sr}_{0.73}\text{CuO}_2$  in Chapter 3, the Heisenberg model that interpolates between isolated dimers ( $\alpha = 0$ ) and a uniform chain ( $\alpha = 1$ ). The corresponding Hamiltonian for the spin degrees of freedom may be written

$$\mathcal{H} = J \sum_i (\mathbf{S}_{2i} \cdot \mathbf{S}_{2i+1} + \alpha \mathbf{S}_{2i} \cdot \mathbf{S}_{2i-1}), \quad (4.2)$$

representing a chain where pairs of spins are alternately coupled by strong  $J$  and weak  $\alpha J$  bonds. The range of the interactions is confined to nearest neighbours. This Hamiltonian stands for a wide class of systems in which dimerisation occurs [65, 66]. The same procedure to analyse  $\chi(T)$  as described in Section 3.3 can be applied to obtain an estimate of the exchange couplings in  $\text{Ca}_{0.83}\text{CuO}_{2-\delta}$ . As no signature for a low-temperature Curie–Weiss term is observed down to  $T = 2$  K, let us use

$$\chi(T) = \chi_0 + \chi_{\text{chain}}(T), \quad (4.3)$$

where  $\chi_0$  is the sum of the temperature-independent core diamagnetic and Van Vleck terms, and the  $\chi_{\text{chain}}(T)$  is approximated by Eq. (3.8). The fits are shown in Fig. 4.5 for the parameters summarised in Table 4.2. Although the results of the fitting appear to be satisfactory,  $N_{\text{AC}}$  shows large deviations from the expected spin density obtained from either the formal valency of Cu  $N$  or the Curie–Weiss fit at high temperatures  $N_{\text{CW}}$ .

Alternatively, a more reasonable fit was possible taking into account the fact that  $\text{Ca}_{0.83}\text{CuO}_{2-\delta}$  has a finite coupling  $J_{\perp}$  between the chains, reflected by the AF order at  $T_{\text{AF}}$  [33]. The spatially anisotropic Heisenberg model for parallel chains forming a square 3D lattice is then

$$\mathcal{H} = J \sum_i (\mathbf{S}_{2i} \cdot \mathbf{S}_{2i+1} + \alpha \mathbf{S}_{2i} \cdot \mathbf{S}_{2i-1}) + J_{\perp} \sum_{i,\delta} \mathbf{S}_i \cdot \mathbf{S}_{i,\delta}, \quad (4.4)$$

where  $i$  denotes lattice sites along the chain, and  $\delta$  is summed over the nearest-neighbour sites in the transverse directions. The exchange constants parallel and perpendicular to the chain are  $J$  and  $J_{\perp}$ , respectively. Using a mean-field treatment for the interchain coupling  $J_{\perp}$ , the magnitude of  $J_{\perp}$  in coupled quantum spin  $S = 1/2$  chains was determined by Schulz from  $J$  and the ordering temperature  $T_N$  to be

$$J_{\perp} = \frac{k_B T_N}{4A \sqrt{\ln(\Lambda J/k_B T_N)}}, \quad (4.5)$$

where  $A = 0.32$  and  $\Lambda = 5.8$  were determined numerically [81]. This yields  $J_{\perp}/k_B \sim 5$  K for  $\text{Ca}_{0.83}\text{CuO}_{2-\delta}$  with  $J/k_B \sim 50 - 60$  K. A first-order

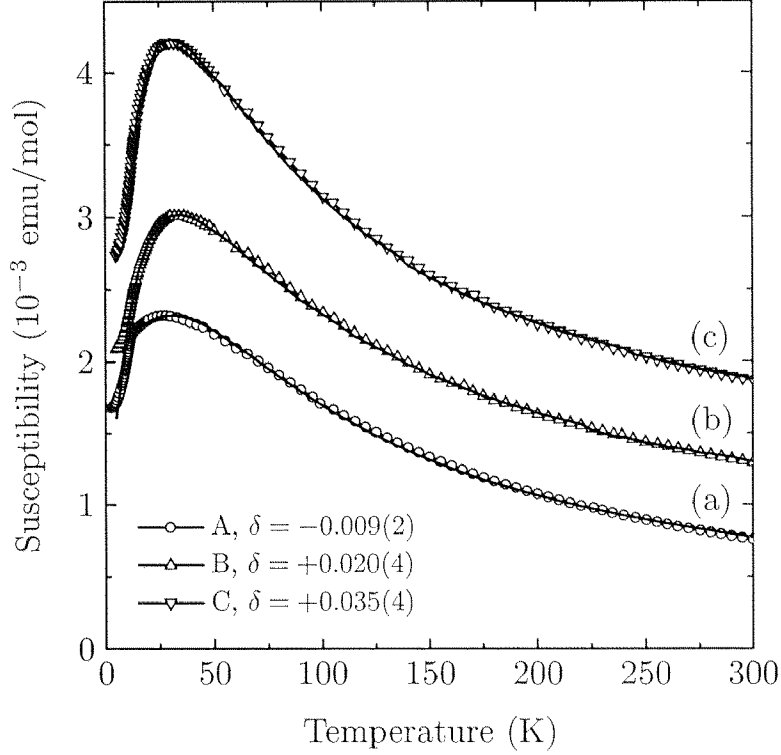


Figure 4.6: Second approach; fit of the susceptibility  $\chi(T)$  for  $\text{Ca}_{0.83}\text{CuO}_{2-\delta}$  with model of coupled quantum spin chain [Eq. (4.4)]. (a)  $\text{Ca}_{0.83}\text{CuO}_{2.009}$ , (b)  $\text{Ca}_{0.83}\text{CuO}_{1.980}$ , and (c)  $\text{Ca}_{0.83}\text{CuO}_{1.965}$ . Curves for (b) and (c) are offset by  $0.5 \times 10^{-3}$  emu/mol and  $1 \times 10^{-3}$  emu/mol, respectively.

Sample	$N$	$N_{\text{AC}}$	$J_{\perp}(\text{K})$	$J(\text{K})$	$\alpha$	$\chi_0(\text{emu/mol})$
A	0.64(1)	0.64(1)	5	58(2)	0.92(5)	$6(1) \times 10^{-5}$
B	0.70(1)	0.71(1)	5	64(2)	0.81(7)	$4(1) \times 10^{-5}$
C	0.73(1)	0.75(1)	5	61(2)	0.64(5)	$4(1) \times 10^{-5}$

Table 4.3: Parameters for  $\text{Ca}_{0.83}\text{CuO}_{2-\delta}$ : the average number of spins per formula unit  $N$  is derived from the formal Cu valence.  $N_{\text{AC}}$ ,  $J/k_B$ , and  $\alpha$  are determined from the fit (Fig. 4.6) taking the interchain interaction into account [Eq. (4.4)].  $J_{\perp}/k_B = 5$  K was fixed during fitting.

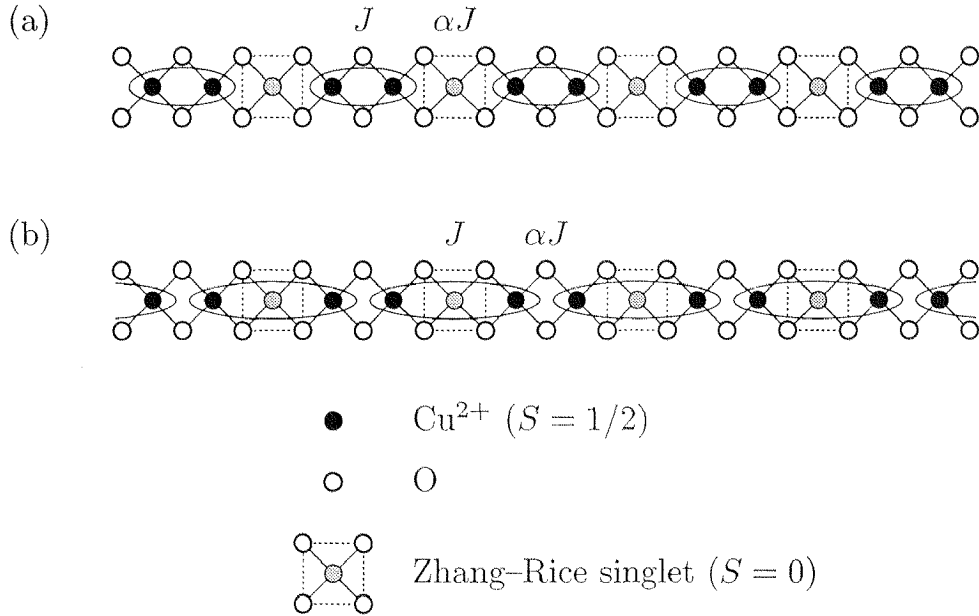


Figure 4.7: Model for distribution of  $\text{Cu}^{2+}$  and holes in the  $\text{CuO}_2$  chains of  $\text{Ca}_{0.83}\text{CuO}_2$ . If the exchange coupling over the  $\text{Cu-O-Cu}$  bond is stronger than along the  $\text{Cu-O-O-Cu}$  path, dimers are formed as indicated in (a). Otherwise as in (b).

approximation to remove the effect of the interchain interaction is to translate the energy scale of the susceptibility of the alternating chain Heisenberg model by  $J_{\perp}$  ( $\ll J$ ) similar to the introduction of  $\Theta$  in the Curie law [81]. The results of fitting, taking into account a transverse exchange  $J_{\perp}/k_B = 5$  K, are displayed in Fig. 4.6. The experimental data can be reproduced well over the wide temperature range from 15 to 300 K. The best fit to the data for the as-prepared  $\text{Ca}_{0.83}\text{CuO}_{2.009}$  sample using this “modified” alternating chain Heisenberg model yields the parameters  $N = 0.64(1)$  spins per f.u.,  $J/k_B = 58(2)$  K,  $\alpha = 0.92(5)$ , and  $\chi_0 = 6(1) \times 10^{-5}$  emu/mol. The  $\chi(T)$  data for the other two samples shown in Fig. 4.3 were analysed with the same model. The parameters obtained by the fitting procedure are collected in Table 4.3. The spin density (noted as  $N_{\text{AC}}$  in Table 4.3) is now in excellent agreement with the expected values. With increasing  $\delta$ ,  $J$  remains unchanged to the first order and  $\alpha$  decreases, on average corresponding to a reduction of coupling between the dimers in the chain. A possible origin of this will be discussed later on in this chapter.

The arrangement of holes is a key to resolve the physical background of the alternating Heisenberg chain behaviour in case the of  $\text{Ca}_{0.83}\text{CuO}_2$ . As

Zhang–Rice singlets are known to repel each other strongly [82], the density of holes is expected to have a uniform modulation along the chains. An idealised distribution of holes in the  $\text{CuO}_2$  chains of  $\text{Ca}_{0.83}\text{CuO}_2$  (about one holes in three Cu sites) is presented in Figs. 4.7(a) and (b). In both cases, the proposed spin/charge order would give rise to a modulated exchange coupling, which is a prerequisite for dimerisation. This dimerisation is different from the one found in spin–Peierls compounds in that it is associated with charge ordering of nonmagnetic holes resulting in a spin/charge density wave and not with a progressive temperature-dependent lattice distortion. Depending on the relative strength of the exchange interaction along the Cu–O–Cu and Cu–O–O–Cu path, the dimers are formed as indicated in Fig. 4.7(a) or (b). Although intuition might lead us to expect that a nearest-neighbour coupling is stronger than a next-nearest neighbour coupling, this is probably not the case in the present compound nor, analogously, in  $\text{Sr}_{0.73}\text{CuO}_2$ . To ascribe the alternating Heisenberg chain behaviour of  $\text{Ca}_{0.83}\text{CuO}_2$  to one of these two models, a comparison with undoped  $\text{La}_6\text{Ca}_8\text{Cu}_{24}\text{O}_{41}$  or  $\text{Li}_2\text{CuO}_2$  might be useful. The electronic states of these compounds comprising  $\text{CuO}_2$  chains with  $91^\circ$  bonds have been studied extensively, see e.g., Refs. [83, 84]. The Hamiltonian that was found to describe the systems accurately is

$$\mathcal{H} = J_1 \sum_i \mathbf{S}_i \cdot \mathbf{S}_{i+1} + J_2 \sum_i \mathbf{S}_i \cdot \mathbf{S}_{i+2}, \quad (4.6)$$

where  $J_1$  and  $J_2$  are the respective nearest- and next-nearest-neighbour couplings. Note that no alternation in exchange coupling is present in Eq. (4.6). This model Hamiltonian essentially introduces an effective frustration in the spin system. In the discussion of  $\text{La}_6\text{Ca}_8\text{Cu}_{24}\text{O}_{41}$  [83],  $\text{Li}_2\text{CuO}_2$  [84], and also  $\text{CuGeO}_3$  [85, 86, 87], a significant next-nearest-neighbour exchange  $J_2$  was indispensable. An important contribution to the theoretical understanding of edge-sharing chains was that the nearest-neighbour coupling  $J_1$  depends sensitively on the Cu–O–Cu bond angle  $\theta$ , whereas the next-nearest-neighbour coupling  $J_2$  does not [83]. The reason is that they occur due to different mechanisms. The leading mechanism for the next-nearest-neighbour exchange is the usual superexchange along the path Cu–O–O–Cu where two holes meet within the same oxygen orbital and the resulting coupling is due to Pauli’s principle AF. On the other hand, the most important process of nearest-neighbour exchange has a virtual state of two holes in different oxygen orbitals. They feel Hund’s rule coupling, which gives rise to a ferromagnetic exchange. If the bond angle deviates from  $90^\circ$  one can find magnitudes of AF contributions similar to the superexchange process for next-nearest-neighbours. In particular, the sign of  $J_1$  changes at  $\sim 94^\circ$  when changing from ferromagnetic (for  $\theta \lesssim 94^\circ$ ) to AF (for  $\theta \gtrsim 94^\circ$ ) with increasing bond

angle. (Note that for the Cu–O–Cu bond angles  $\theta = 90^\circ$  and  $\theta = 180^\circ$  the Goodenough–Kanamori–Anderson rules [88, 89, 90] predict a ferromagnetic and AF exchange, respectively.) This means  $J_1$  becomes negligibly small when the Cu–O–Cu bond angle is  $\theta \sim 94^\circ$ , whereas the next-nearest-neighbour exchange remains at  $J_2/k_B \sim 80$  K for  $\theta$  ranging from  $80^\circ$  to  $100^\circ$  [83]. For the idealised structure of  $\text{Ca}_{0.83}\text{CuO}_2$  shown in Fig. 4.1, a bond angle of  $\theta \sim 95^\circ - 96^\circ$  is expected. As a consequence the most probable scenario for  $\text{Ca}_{0.83}\text{CuO}_2$  is that  $J_2 > J_1$  ( $\gtrsim 0$ ). It follows, accordingly, that one is apt to think that singlet pairing takes place as indicated in Fig. 4.7(b). We shall have occasion to return to this point, as it turns out that in the case of  $\text{Sr}_{0.73}\text{CuO}_2$  the topological dimer structure can be determined experimentally (Chapter 6).

Returning to the dependence of the average exchange coupling  $\alpha J$  on the oxygen deficiency  $\delta$ , a possible explanation for this is that an oxygen vacancy in the  $\text{CuO}_4$  unit is created by omitting only one O atom instead of cutting the chain by omitting two O atoms simultaneously. This O vacancy introduces, aside from the already present charge modulation, an additional contribution to the modulation of the exchange coupling. The reason is that the remaining O atom rearranges itself due to its modified coordination, and thus modifies the angle of the Cu–O–Cu bonds. Because of the strong dependence of the exchange coupling  $J/k_B$  on the bond angle and bond length [83, 91], reaching values of 2000 K and more for  $180^\circ$  bonds. A small variation of the bond angle is sufficient to exert a major effect on the exchange couplings.

### 4.3 Magnetic order: a torque investigation

In the remainder of this chapter let us focus our attention on the AF ordered state below  $T_{\text{AF}}$ . Angle-dependent torque measurements were performed on a single crystal of volume  $V \sim 700 \times 400 \times 50 \mu\text{m}^3$  with a highly sensitive capacitive torquemeter (resolution  $\sim 10^{-12}$  Nm) [30]. The torque is given by  $\boldsymbol{\tau} = \mathbf{m} \times \mathbf{B}$ , where  $\mathbf{m}$  is the sample magnetic moment and  $\mathbf{B}$  the magnetic field. Anisotropic, ordered materials are well suited for torque magnetometry, whereas e.g., a spin-glass or spin–Peierls compound will yield  $\boldsymbol{\tau} \sim 0$ .

The model configuration for an antiferromagnet with easy axis (EA) is depicted in the inset of Fig. 4.8. In the ordered state the spin-up and spin-down sublattice yield the respective macroscopic magnetic moments  $\mathbf{m}_a$  and  $\mathbf{m}_b$ . In a field  $\mathbf{B}$ ,  $\mathbf{m}_a$  and  $\mathbf{m}_b$  are tilted away from the EA towards  $\mathbf{B}$ . The macroscopic torque for this system is given by  $\boldsymbol{\tau} = \mathbf{m}_a \times \mathbf{B} + \mathbf{m}_b \times \mathbf{B}$ . As the respective angles  $\phi_1$  and  $\phi_2$  between  $\mathbf{m}_a$  and EA, and between  $\mathbf{m}_b$  and EA

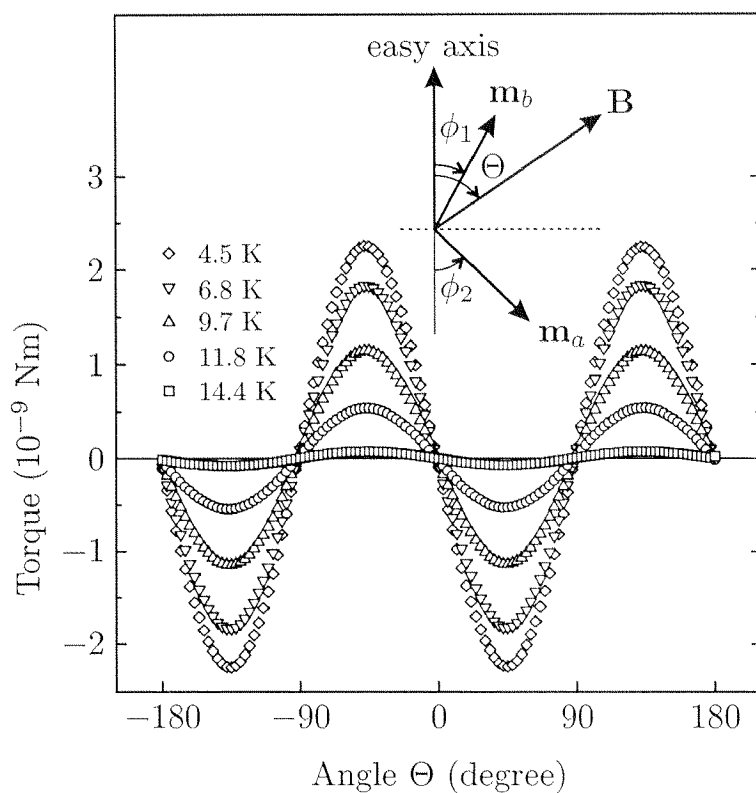


Figure 4.8: Angle-dependent torque  $\tau(\Theta)$  taken on a single crystal at different temperatures upon field rotation  $\mathbf{H} \perp c$ . Angle  $\Theta = 0^\circ$  corresponds to  $\mathbf{H} \parallel b$ . Inset: AF model configuration.

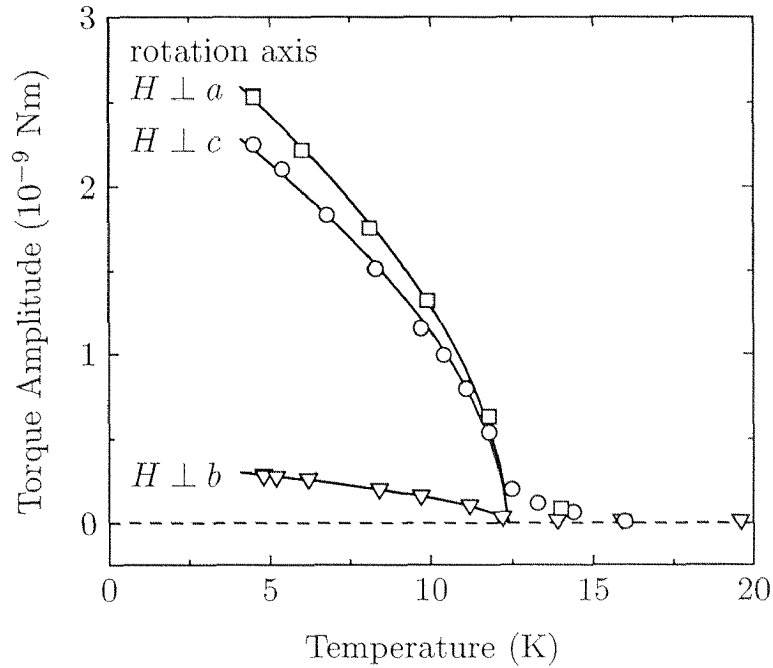


Figure 4.9: Temperature dependence of the torque amplitude  $|\tau(\Theta = 45^\circ)|$  for rotation of  $H$  about the  $a$ ,  $b$ , and  $c$  axes. All three data sets follow the same phenomenological power law  $\tau(T) \propto (1 - T/T_c)^\beta$ , with  $T_c = 12.3(1)$  K and exponent  $\beta = 0.54(2)$ .

are slightly different, a finite but small torque is generated. Assuming small  $\phi$  and only one EA in our system with low symmetry, one can calculate that  $\tau(\Theta) \propto \sin(2\Theta)$ . This also implies that rotation of  $\mathbf{B}$  in the plane perpendicular to EA will yield  $\tau = 0$  for all angles (because  $\Theta = 90^\circ$ ). The torque magnetometer is used for determining (i) the temperature at which the magnetic order starts, derived from the amplitude of  $\tau(T)$ , and (ii) the EA direction using the argument  $\tau = 0$  for all angles when  $\mathbf{B}$  is rotated in the plane perpendicular to the EA.

A series of  $\tau(\Theta)$  curves showing the expected  $\sin(2\Theta)$  behaviour for rotation of the magnetic field ( $\mu_0 H = 1.5$  T) about the crystallographic  $c$  axis measured at different temperatures is presented in Fig. 4.8. It is immediately apparent that with increasing temperature the amplitude of the torque signal is significantly reduced. The temperature dependence of the torque amplitude at  $\Theta = 45^\circ$  is shown in Fig. 4.9 for rotation of the magnetic field about the  $a$ ,  $b$ , and  $c$  axes. The torque amplitude decreases towards zero following the phenomenological power law  $\tau(T) \propto (1 - T/T_{AF})^\beta$  with an exponent of  $\beta = 0.54(2)$  upon approaching  $T_{AF} = 12.3(1)$  K. The drop in  $\chi(T)$  together

with the appearance of torque, both at  $T \sim 12.2$  K, gives conclusive evidence of AF order with the spins aligned along the EA of magnetisation. Whether this ordering is 2D or 3D in nature cannot simply be inferred from the data presented in this chapter and will be discussed in Chapter 5. The exponent  $\beta$  is found to be close to its mean-field value  $\beta = 0.5$ . The small remaining torque above  $T_{\text{AF}}$  might be due to short-range ordered regions that exist before the AF order sets in. Similar behaviour is observed in  $\text{La}_6\text{Ca}_8\text{Cu}_{24}\text{O}_{41}$  [92] and  $\text{Sr}_{0.73}\text{CuO}_2$  [32] by neutron and EPR measurements, respectively. The torque amplitude  $|\tau(\Theta = 45^\circ)|$  is relatively large for rotation about the  $a$  and  $c$  axes and one order of magnitude smaller for rotation about the  $b$  axis. From this fact we can conclude that, within experimental error ( $\sim 5^\circ$ ), the EA is the  $b$  axis. This magnetic anisotropy has been attributed in the case of undoped AF insulating cuprates to either an antisymmetric exchange [93] or the Coulomb exchange interaction [94].

In summary we have seen in this chapter that  $\text{Ca}_{0.83}\text{CuO}_{2-\delta}$  exhibits AF order just as in the case of  $\text{Sr}_{0.73}\text{CuO}_2$  [33]. Contrary to the situation in  $\text{Sr}_{0.73}\text{CuO}_2$ , however, no spin canting resulting in a weak-ferromagnetic moment is found in  $\text{Ca}_{0.83}\text{CuO}_{2-\delta}$ . The ordering temperature  $T_{\text{AF}} = 12.2(1)$  K is independent of the extent of doping from 0.27 to 0.36 holes/Cu. A torque analysis demonstrated the existence of an easy axis in this ordered state. Its orientation is found to be along the crystallographic  $b$  axis. Above  $T \sim 15$  K the static susceptibility can be described with a model of a 3D assembly of loosely coupled alternating Heisenberg chains. This gives evidence of singlet pairing of spins in the  $\text{CuO}_2$  chains of  $\text{Ca}_{0.83}\text{CuO}_{2-\delta}$  similar to the case of  $\text{Sr}_{0.73}\text{CuO}_2$ . The average alternation can be tuned by varying the oxygen content of the chain.



Seite Leer /  
Blank leaf

# Chapter 5

## Long-range magnetic order $\text{Ca}_{0.83}\text{CuO}_2$ and $\text{Sr}_{0.73}\text{CuO}_2$

### 5.1 Introduction

Strictly 1D spin chain systems cannot sustain a spontaneous magnetisation at any finite temperature [4, 5], i.e., magnetic order is suppressed by quantum fluctuations and a nonmagnetic singlet ground state is formed [3]. In fact, the only possible deviation from the ideal 1D behaviour that can have the effect of establishing magnetic ordering is the presence of a weak but finite magnetic coupling between adjacent chains. Particularly interesting is the case where doping leads to competition between the quantum-mechanical singlet ground state and the classical long-range ordered state. This phenomenon was observed in the spin-Peierls compound  $\text{CuGeO}_3$ , which is known to undergo a structural transition at  $T_{\text{SP}} \sim 14$  K, below which the  $\text{CuO}_2$  chains dimerise [95, 96] and the spin gap opens [97, 98]. More recently, doping of this compound, for example with Ni ( $S = 1$ ) or nonmagnetic Zn, led to a long-range 3D AF ordered phase coexisting with the spin-Peierls state at  $T \lesssim 4$  K [22, 58, 99, 100, 101, 102]. This fascinating coexistence of the spin-Peierls state with the classical Néel state has attracted much interest as these two different ground states were generally believed to be mutually exclusive [23, 24, 25, 26].

The dimerised phase found in the highly hole-doped  $\text{CuO}_2$  chains of  $(\text{Sr,Ca})_{14}\text{Cu}_{24}\text{O}_{41}$  is different from the one found in  $\text{CuGeO}_3$  in that it is associated with charge ordering of nonmagnetic holes, and not with a spin-Peierls transition [103, 104, 105, 106]. A long-range ordered state is stabilised only in undoped  $\text{La}_6\text{Ca}_8\text{Cu}_{24}\text{O}_{41}$  (all  $\text{Cu}^{2+}$  oxidation state) [92] and lightly

doped  $\text{La}_5\text{Ca}_9\text{Cu}_{24}\text{O}_{41}$  [107] (in both compounds no dimerisation is found).

Two further examples of quasi-1D cuprates where doping is realised by introducing holes are  $\text{Sr}_{0.73}\text{CuO}_2$  [32] and  $\text{Ca}_{0.83}\text{CuO}_2$  [33], discussed in Chapters 3 and 4, respectively. Recall that the formal valence of Cu is +2.34 and +2.54 for  $\text{Ca}_{0.83}\text{CuO}_2$  and  $\text{Sr}_{0.73}\text{CuO}_2$ , respectively, i.e., there are inherently 0.34 and 0.54 holes/Cu present in the  $\text{CuO}_2$  chains. We have seen that the susceptibility can be described with the alternating chain Heisenberg model like in  $\text{Sr}_{14}\text{Cu}_{24}\text{O}_{41}$ . This gives an indication of singlet pairing of spins. However, in contrast to hole-doped  $(\text{La},\text{Sr},\text{Ca})_{14}\text{Cu}_{24}\text{O}_{41}$  compounds, susceptibility measurements indicated that  $\text{Ca}_{0.83}\text{CuO}_2$  and  $\text{Sr}_{0.73}\text{CuO}_2$  exhibit AF order at  $T \sim 10$  K. In addition, a weak-ferromagnetic component was observed in  $\text{Sr}_{0.73}\text{CuO}_2$ . This observation prompted us to speculate about a coexistence of a magnetically ordered state and a singlet ground state like in doped  $\text{CuGeO}_3$ .  $\text{Ca}_{0.83}\text{CuO}_2$  and  $\text{Sr}_{0.73}\text{CuO}_2$  are particularly interesting because one can study the role of hole doping in quasi-1D spin systems (i) without introducing structural disorder as in doped  $\text{CuGeO}_3$ , and (ii) without controversies raised by the presence of two-leg ladders next to the spin chains in  $(\text{La},\text{Sr},\text{Ca})_{14}\text{Cu}_{24}\text{O}_{41}$  compounds.

The next two chapters will provide convincing evidence that at least in  $\text{Sr}_{0.73}\text{CuO}_2$  a spin dimer phase coexists with long-range AF order below  $T \sim 10$  K. A study of magnetic excitations in  $\text{Sr}_{0.73}\text{CuO}_2$  will be found in the next chapter; this chapter is devoted to a further investigation of the magnetically ordered phase at low temperatures, a discussion of the specific heat and neutron diffraction of polycrystalline  $\text{Ca}_{0.83}\text{CuO}_2$  and  $\text{Sr}_{0.73}\text{CuO}_2$ , and magnetic torque measurements of single crystals. These measurements indicate that the AF ordered state discussed in Chapters 3 and 4 is of long-range 3D character [34]. The specific heat was measured using a commercial microcalorimeter (Quantum Design) [108]. Neutron scattering experiments were performed on three different powder diffractometers: on the cold neutron powder diffractometer DMC installed at the neutron spallation source SINQ of the Paul Scherrer Institute, Villigen, Switzerland [41], on the high-resolution diffractometer D1A [42], and on the diffractometer D1B [43], both at the high-neutron-flux reactor of the Institut Laue Langevin, Grenoble, France.

## 5.2 Specific heat

We have measured the specific heat in order to gain more insight into the unusual magnetism of  $\text{Ca}_{0.83}\text{CuO}_2$  and  $\text{Sr}_{0.73}\text{CuO}_2$ . The temperature dependence of the specific heat  $C/T$  of polycrystalline  $\text{Sr}_{0.73}\text{CuO}_2$  and  $\text{Ca}_{0.83}\text{CuO}_2$

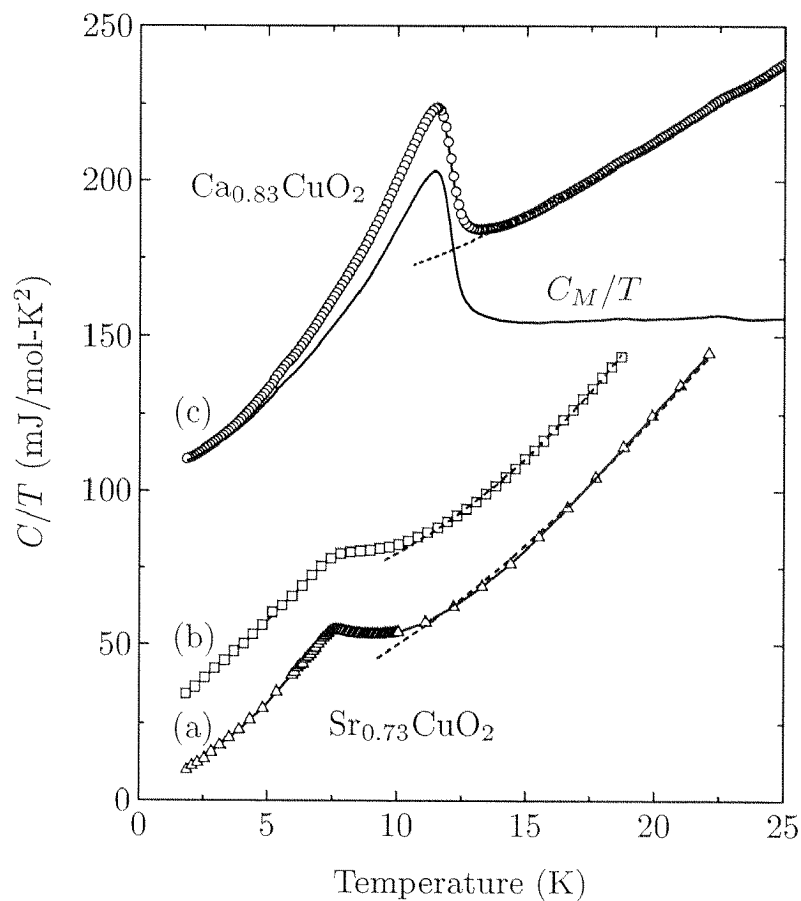


Figure 5.1: Specific heat  $C(T)/T$  of  $\text{Sr}_{0.73}\text{CuO}_2$  in (a)  $\mu_0 H = 0$  T and (b)  $\mu_0 H = 5$  T. (c)  $C(T)/T$  of  $\text{Ca}_{0.83}\text{CuO}_2$  in  $\mu_0 H = 0$  T. Curves for (b) and (c) are offset for clarity by 25 mJ/(mol K<sup>2</sup>) and 100 mJ/(mol K<sup>2</sup>), respectively. The magnetic contribution  $C_M/T$  is shown for  $\text{Ca}_{0.83}\text{CuO}_2$ . Dashed lines are fits of  $(C_M + C_L)/T$  to the high-temperature data.

measured in  $\mu_0 H = 0$  T is shown in Fig. 5.1 as curves (a) and (c), respectively. As the temperature is lowered from  $T = 25$  K, the specific heat decreases as the lattice contribution falls. A sharp peak in the specific heat is observed for  $\text{Ca}_{0.83}\text{CuO}_2$  at  $T \sim 12$  K and for  $\text{Sr}_{0.73}\text{CuO}_2$  at  $T \sim 7.5$  K. This indicates a static magnetic transition, in accordance with what was predicted by susceptibility measurements. The ordering temperature  $T_{\text{AF}}$  obtained for  $\text{Ca}_{0.83}\text{CuO}_2$  coincides with the value determined from the susceptibility measurements presented in Chapter 4. Likewise, for  $\text{Sr}_{0.73}\text{CuO}_2$  the magnetic order appears at  $T_{\text{AF}} \sim 7.5 - 10$  K, though it is less appreciable than in  $\text{Ca}_{0.83}\text{CuO}_2$ . In  $\text{Sr}_{0.73}\text{CuO}_2$  the short-range interactions at  $T \gtrsim T_{\text{AF}}$  reflected in the high-temperature tail of the transition, are more pronounced. The ordering temperature of  $\text{Sr}_{0.73}\text{CuO}_2$  is independent of the external magnetic field as depicted in Fig. 5.1(b), which shows the specific heat measurement at  $\mu_0 H = 5$  T. The magnetic entropy involved in the magnetic ordering at  $T < T_{\text{AF}}$  is estimated to be  $\Delta S \sim 610$  mJ/(mol K) and  $\Delta S \sim 190$  mJ/(mol K) for  $\text{Ca}_{0.83}\text{CuO}_2$  and  $\text{Sr}_{0.73}\text{CuO}_2$ , respectively. This means that for  $\text{Ca}_{0.83}\text{CuO}_2$  11% and for  $\text{Sr}_{0.73}\text{CuO}_2$  only 3.3% of the total magnetic entropy  $S = N_A k_B \ln 2$  is involved in the magnetic ordering. This is not surprising considering that the thermodynamic effect associated with magnetic ordering from short-range correlations within the chain is expected to be small; most of the entropy is involved in the 1D AF correlations above the ordering temperature  $T_{\text{AF}}$ .

As a consequence of the absence of long-range ordering in the ideal 1D system, with decreasing temperature the magnetic entropy has to be removed in short-range order processes. This is reflected by the specific heat and susceptibility, both of which display broad maxima at temperatures of the order of magnitude of the exchange coupling along the chain. Neglecting the inter-chain coupling the specific heat for a 1D  $S = 1/2$  Heisenberg antiferromagnet varies linearly with temperature between  $T_{\text{AF}} \lesssim T \lesssim 0.5 J/k_B$  [109, 110],

$$C_M = \alpha T = \frac{2Nk_B^2}{3J} T, \quad (5.1)$$

where  $N$  is the number of spins in the system (total Cu atoms minus holes),  $k_B$  is the Boltzmann constant, and  $J$  is the exchange interaction in the chain. In order to separate the specific heat of the magnetic excitations  $C_M$  from the lattice contribution  $C_L$ , we have modelled the latter by

$$C_L = \beta_1 T^3 + \beta_2 T^5. \quad (5.2)$$

From the fits of  $(C_M + C_L)/T$  to the data (dashed lines in Fig. 5.1) we obtain for  $\text{Ca}_{0.83}\text{CuO}_2$  the magnetic contribution  $\alpha = 55.0(2)$  mJ/(mol K<sup>2</sup>)

and lattice parameters  $\beta_1 = 0.163(1)$  mJ/(molK<sup>4</sup>) and  $\beta_2 = -5.4(5) \times 10^{-5}$  mJ/(molK<sup>6</sup>). For Sr<sub>0.73</sub>CuO<sub>2</sub> we find  $\alpha = 18(2)$  mJ/(molK<sup>2</sup>),  $\beta_1 = 0.288(2)$  mJ/(molK<sup>4</sup>), and  $\beta_2 = -8.0(1) \times 10^{-5}$  mJ/(molK<sup>6</sup>). Using [111]

$$\beta_1 = \frac{12\pi^4}{5} N_A k_B \frac{1}{\Theta_D^3}, \quad (5.3)$$

the Debye temperature  $\Theta_D$  for Sr<sub>0.73</sub>CuO<sub>2</sub> and Ca<sub>0.83</sub>CuO<sub>2</sub> are found to be  $\Theta_D \sim 300$  K and 360 K, respectively. From the  $\alpha$  value we find the exchange interaction  $J/k_B$  to be 67(1) K for Ca<sub>0.83</sub>CuO<sub>2</sub> and 210(20) K for Sr<sub>0.73</sub>CuO<sub>2</sub>. The value of  $J$  obtained for Ca<sub>0.83</sub>CuO<sub>2</sub> is consistent with previous susceptibility measurements, where the exchange interaction was found to be  $J/k_B = 62(3)$  K (Chapter 4). This contrasts with Sr<sub>0.73</sub>CuO<sub>2</sub>, for which only the correct order of magnitude is found. Evidently, the fact that Sr<sub>0.73</sub>CuO<sub>2</sub> is not a homogeneous chain, in the sense that all couplings along the chain are identical, causes a large deficiency from the approximation of the specific heat with a linear temperature dependence. The more reliable susceptibility measurements yielded  $J/k_B = 174(8)$  K for Sr<sub>0.73</sub>CuO<sub>2</sub> (Chapter 3). As a consequence the maximum of the chain specific heat is expected to occur at a temperature at which the lattice contribution is about 50 times larger, so that one can scarcely hope to be able to separate the magnetic part for accurate fitting.

### 5.3 Neutron diffraction

To decide whether the magnetically ordered state at  $T < T_{AF}$  is of long-range 3D character, elastic neutron scattering is a most valuable tool. Part of the neutron diffraction pattern measured on the cold neutron powder spectrometer DMC, PSI Villigen, Switzerland, is shown in Figs. 5.2(a) and (b) for the Ca<sub>0.83</sub>CuO<sub>2</sub> and Sr<sub>0.73</sub>CuO<sub>2</sub> samples. The neutron diffraction patterns above and below the ordering temperature  $T_{AF}$  are shown together with their difference. In the difference patterns a peak can be identified for each sample. Considering the sample mass and measuring time, the peak intensity in Ca<sub>0.83</sub>CuO<sub>2</sub> is about one order of magnitude larger than that in Sr<sub>0.73</sub>CuO<sub>2</sub>. The observed increase in intensity upon cooling is too large to be attributed simply to the Debye–Waller factor. For the indexing of the observed peaks, the notation of the Cu–O unit cell defined in Fig. 5.3 is used. The indicated low-temperature lattice parameters for Ca<sub>0.83</sub>CuO<sub>2</sub> were determined at the diffractometer DMC at the PSI and for Sr<sub>0.73</sub>CuO<sub>2</sub> on the diffractometer D1A at the ILL. The position of the two peaks that show the temperature dependence can then be indexed as (0 1/2 1) in Ca<sub>0.83</sub>CuO<sub>2</sub> and

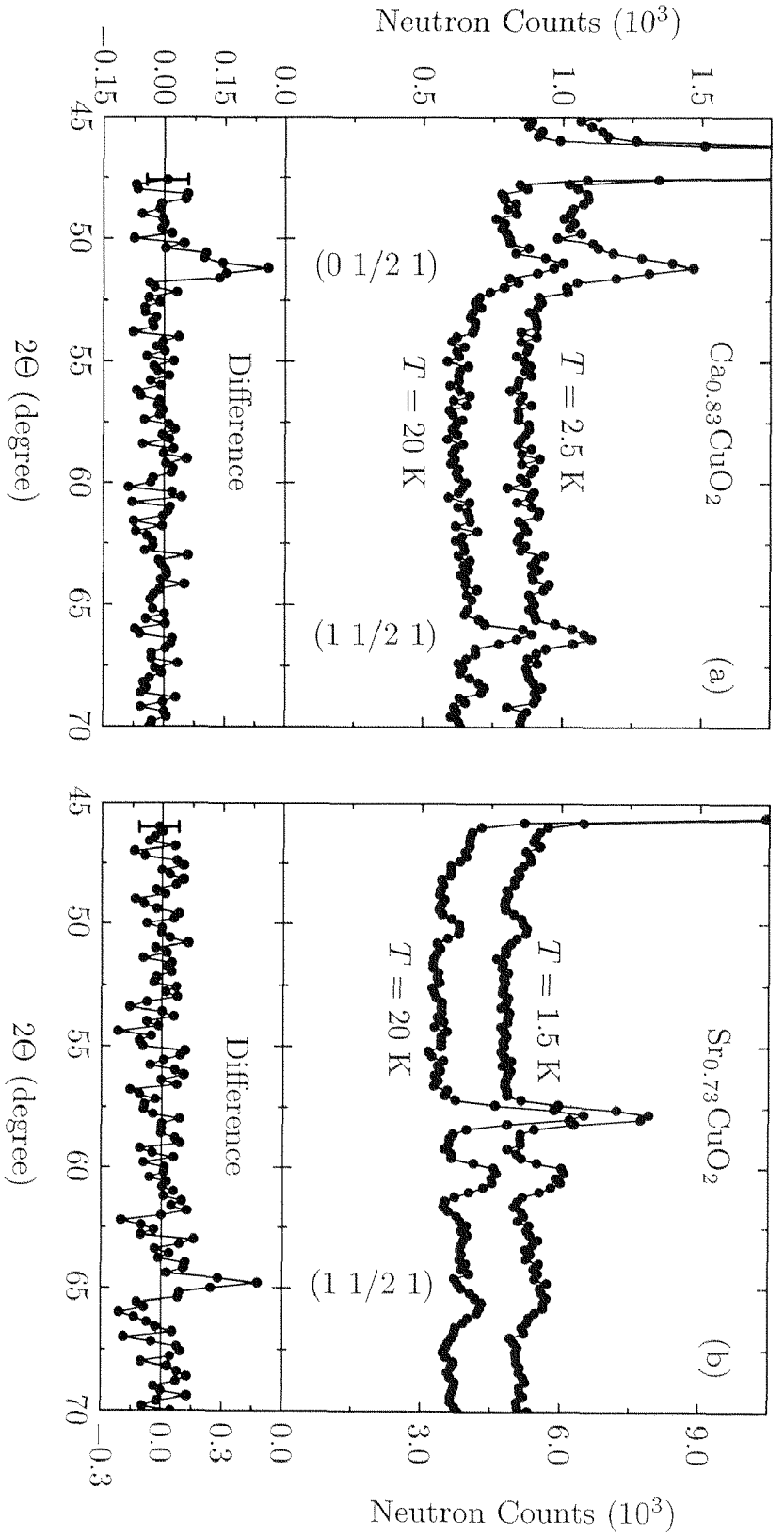


Figure 5.2: Part of the neutron diffraction pattern above and below  $T_{\text{AF}}$  measured on the diffractometer DMC with  $\lambda = 4.209$  Å for (a)  $\text{Ca}_{0.83}\text{CuO}_2$  and (b)  $\text{Sr}_{0.73}\text{CuO}_2$ . The low-temperature spectrum is offset for clarity. Also displayed is the difference between the low- and high-temperature patterns. The size of the error bar is indicated at the first data point and is representative of the entire spectrum shown.

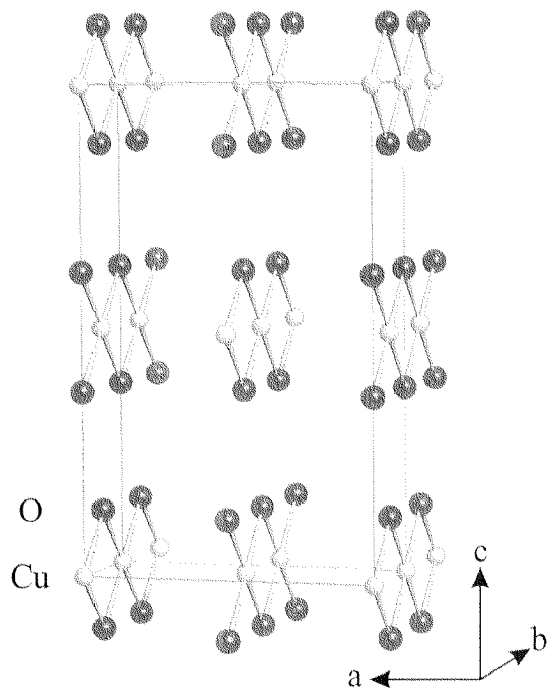


Figure 5.3: Schematic representation of the  $\text{CuO}_2$  sublattice of  $\text{Ca}_{0.83}\text{CuO}_2$  and  $\text{Sr}_{0.73}\text{CuO}_2$  with the face-centred orthorhombic unit cell. Unit cell parameters for the  $\text{CuO}_2$  sublattice in  $\text{Ca}_{0.83}\text{CuO}_2$  are  $a = 6.311(2) \text{ \AA}$ ,  $b = 2.742(1) \text{ \AA}$ , and  $c = 10.593(5) \text{ \AA}$  (measured on diffractometer DMC at  $T = 2.5 \text{ K}$  with wavelength of  $\lambda = 4.209 \text{ \AA}$ ). For  $\text{Sr}_{0.73}\text{CuO}_2$ ,  $a = 6.797(1) \text{ \AA}$ ,  $b = 2.7209(4) \text{ \AA}$ , and  $c = 10.998(2) \text{ \AA}$  (measured on diffractometer D1A at  $T = 1.5 \text{ K}$  with  $\lambda = 1.908 \text{ \AA}$ ). In this crystallographic notation, the  $a$  and  $b$  axes are interchanged compared to Figs. 3.1 and 4.1.



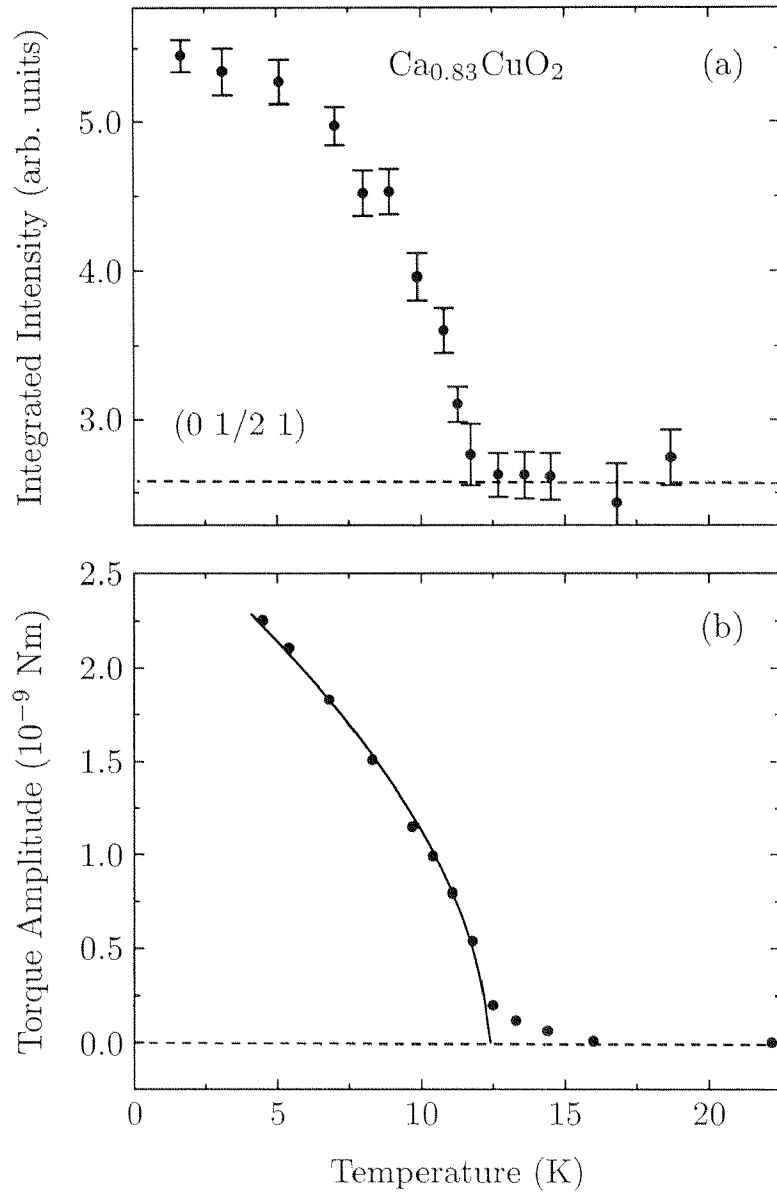


Figure 5.4: (a) Temperature dependence of the  $(0\ 1/2\ 1)$  neutron peak intensity of  $\text{Ca}_{0.83}\text{CuO}_2$  measured on the diffractometer D1B with  $\lambda = 2.52\ \text{\AA}$ . (b) Temperature dependence of the torque amplitude of  $\text{Ca}_{0.83}\text{CuO}_2$  ( $\mu_0 H = 1.5\ \text{T}$ ). Also shown is  $\tau(T) \propto (1 - T/T_c)^\beta$ , with  $T_c = 12.3(1)\ \text{K}$  and exponent  $\beta = 0.54(2)$ .

(1 1/2 1) in  $\text{Sr}_{0.73}\text{CuO}_2$ . In both cases a twofold increase in periodicity along the  $\text{CuO}_2$  chain axis is found. The temperature dependence of the integrated intensity of the (0 1/2 1) peak of  $\text{Ca}_{0.83}\text{CuO}_2$  measured on the spectrometer D1B at the ILL is shown in Fig. 5.4(a). A clear increase of the neutron intensity is observed at  $T \lesssim 12$  K. Note that in the neutron spectrum of  $\text{Sr}_{0.73}\text{CuO}_2$  a small amount ( $\sim 5\%$ ) of the impurity phase  $\text{SrCO}_3$  is visible. However, this nonmagnetic phase, which yields scattering at  $2\Theta \sim 57.8^\circ$  and  $60.2^\circ$ , does not influence the magnetic properties discussed here.

## 5.4 Torque $\text{Sr}_{0.73}\text{CuO}_2$

Angle-dependent torque measurements were performed on a twinned single crystal of  $\text{Sr}_{0.73}\text{CuO}_2$  (volume  $V \sim 120 \times 90 \times 8 \mu\text{m}^3$ ) with a highly sensitive torquemeter based on the piezoresistive cantilever (resolution  $\sim 10^{-13}$  Nm) [29]. Measurements on an untwinned single crystal of  $\text{Ca}_{0.83}\text{CuO}_2$  have been shown in Chapter 4. The torquemeter is used for this investigation because the sensitivity of a SQUID magnetometer would not be sufficient. For comparison, a SQUID magnetometer has a typical sensitivity of  $\Delta m \sim 10^{-7}$  emu, whereas one achieves  $\Delta m \sim 10^{-10}$  emu in  $B = 1$  T with the torquemeter.

The torque is given by  $\boldsymbol{\tau} = \mathbf{m} \times \mathbf{B}$ , where  $\mathbf{m}$  is the sample magnetic moment and  $\mathbf{B}$  is the magnetic field (see Chapters 2 and 4 for an extended description on torque). A finite torque is expected if the sample possesses a finite moment  $\mathbf{m}$ . This condition is fulfilled in the magnetically ordered state. For  $\text{Sr}_{0.73}\text{CuO}_2$  a series of  $\tau(\Theta)$  curves for rotation of the magnetic field  $\mu_0 H = 0.05$  T about the crystallographic  $b$  axis (and its twin  $a$  axis) measured at different temperatures is presented in Fig. 5.5(a). The angular dependence shows a  $2\theta$  periodicity typical for antiferromagnets as in the case of  $\text{Ca}_{0.83}\text{CuO}_2$ . The temperature dependence of the torque amplitude is shown in Fig. 5.5(b). The torque amplitude is diminished at  $T \gtrsim 10.0(5)$  K, indicating that the compound turned paramagnetic. The ordering temperature  $T_{\text{AF}} = 10.0(5)$  K is consistent with susceptibility measurements discussed in Chapter 3 and the specific heat measurements presented in this chapter.

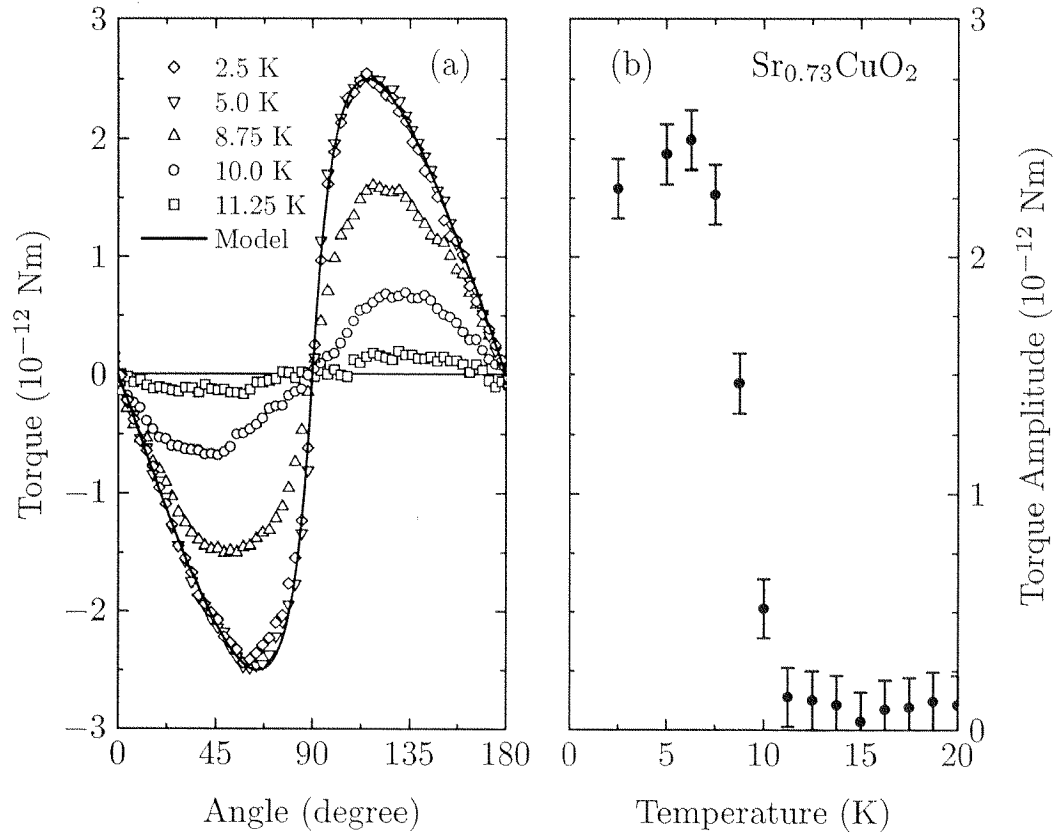


Figure 5.5: (a) Angle-dependent torque  $\tau(\Theta)$  of  $\text{Sr}_{0.73}\text{CuO}_2$  at different temperatures upon field rotation ( $\mu_0 H = 0.05$  T). A theoretical  $\tau(\Theta)$  curve is shown for  $T = 5$  K (model described in Chapter 4). (b) Temperature dependence of the torque amplitude.

## 5.5 Discussion

The experimental results presented above give clear evidence of long-range 3D magnetic order. The observed enhancement in neutron intensity below  $T_{AF}$  of the  $(0\ 1/2\ 1)$  and  $(1\ 1/2\ 1)$  peak in  $\text{Ca}_{0.83}\text{CuO}_2$  and  $\text{Sr}_{0.73}\text{CuO}_2$ , respectively, is consistent with AF ordering. A small structural reorientation of the atoms in the Cu–O subcell could, however, also account for additional neutron intensity at these positions. To differentiate between these two possibilities, it is of great interest that the torque signal is sensitive only to the magnetic moment. A structural reorientation would not contribute to a torque signal. With this argument, a structural transition at  $T \sim 10$  K resulting in an increased neutron intensity can be excluded. The finding of additional neutron intensity at half-integer indices together with the appearance of torque, therefore, provides conclusive evidence of long-range AF order in  $\text{Ca}_{0.83}\text{CuO}_2$  and  $\text{Sr}_{0.73}\text{CuO}_2$ . The resolution-limited peak width indicates that this order is 3D with a correlation length of several hundred angstroms. The neutron intensity at  $(0\ 1/2\ 1)$  in  $\text{Ca}_{0.83}\text{CuO}_2$  for  $T > T_{AF}$  is due to a deviation from the simplified structure shown in Fig. 5.3. A structural dimerisation of nearest-neighbour Cu atoms would be consistent with our observation. Low-temperature synchrotron x-ray diffraction experiments would be very welcome to substantiate this. Note that similar superlattice peaks were recently reported in  $\text{Sr}_{14}\text{Cu}_{24}\text{O}_{41}$  [112].

A qualitative argument allows us to clarify why the magnetic peak intensity of  $\text{Sr}_{0.73}\text{CuO}_2$  is much smaller than the peak in  $\text{Ca}_{0.83}\text{CuO}_2$ . The ordered moment  $m_0 = gS\mu_B \sim 1.04\mu_B$  is strongly renormalised as the result of quantum fluctuations, which are particularly large in low dimensions for spin  $S = 1/2$  ions such as  $\text{Cu}^{2+}$ . It is, for example, known that the ordered moment for the spin  $S = 1/2$  Heisenberg antiferromagnet on a 2D lattice is  $m_0 = 0.606gS\mu_B$ , i.e., 61% of its classical values, as the result of these zero-point spin deviations [113, 114]. The effect of fluctuations grows as one-dimensionality is approached, i.e., it is known that the magnitude of the ordered moment in long-range ordered quasi-1D antiferromagnets decreases as the ratio  $T_N/J$  decreases [81, 115]. Using a model that takes the solution of an isotropic Heisenberg quantum spin chain and describes the loose inter-chain coupling in a mean-field approach, Schulz showed that the staggered magnetisation is given by

$$m_0 \sim \mu_B \sqrt{\frac{J_{\perp}}{J}}, \quad (5.4)$$

where  $J_{\perp}$  is the coupling between the spins of different chains [81]. The magnitude of  $J_{\perp}$  can be determined from the nearest-neighbour intrachain

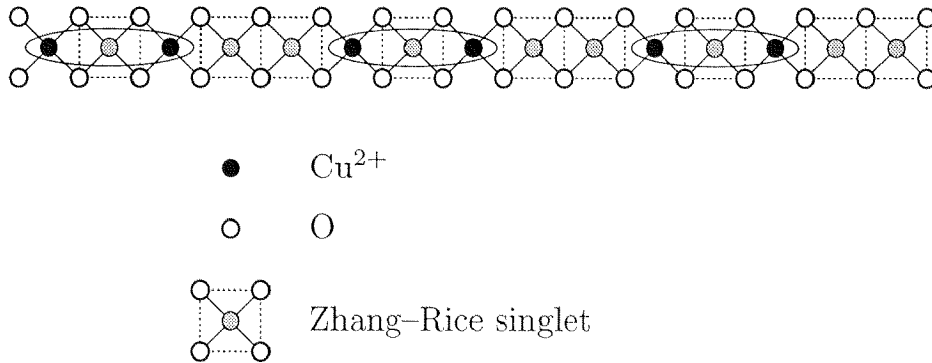


Figure 5.6: Model for the dimerised state and the ordering of  $\text{Cu}^{2+}$  and Zhang-Rice singlets in the  $\text{CuO}_2$  chains of  $\text{Sr}_{14}\text{Cu}_{24}\text{O}_{41}$ .

interaction  $J$  and the ordering temperature  $T_N$ ,

$$J_{\perp} = \frac{k_B T_N}{4A\sqrt{\ln(\Lambda J/k_B T_N)}}, \quad (5.5)$$

where  $A = 0.32$  and  $\Lambda = 5.8$  are determined numerically [81]. For previously investigated 1D systems such as  $\text{Cu}_{1-x}\text{Zn}_x\text{GeO}_3$ ,  $\text{Sr}_2\text{CuO}_3$ ,  $\text{Ca}_2\text{CuO}_3$ , or  $\text{KCuF}_3$  this model is found to describe the reduction of the ordered moment very well [116]. Within the framework of this theory, the ordered moment of  $\text{Ca}_{0.83}\text{CuO}_2$  with  $J_{\perp}/J \sim 5.0/60 = 0.09$  is estimated to be  $m_0 \sim 0.3 \mu_B$ . For  $\text{Sr}_{0.73}\text{CuO}_2$ , with  $J_{\perp}/J \sim 3.6/174 = 0.02$ , an ordered moment size of  $m_0 \sim 0.14 \mu_B$  is expected. This would yield a factor of four difference in magnetic neutron scattering between  $\text{Ca}_{0.83}\text{CuO}_2$  and  $\text{Sr}_{0.73}\text{CuO}_2$ .

As Zhang-Rice singlets are known to repel each other [82], a more or less uniform modulation of the density of holes along the chains is expected. For  $\text{Sr}_{14}\text{Cu}_{24}\text{O}_{41}$ , which has a comparable doping as  $\text{Sr}_{0.73}\text{CuO}_2$ , recent inelastic neutron scattering experiments showed that this is indeed the case [104, 105, 106]. The spin structure is such that the chains are made up of dimers of next-nearest-neighbour  $\text{Cu}^{2+}$  ions separated by two nonmagnetic  $\text{Cu}^{3+}$  ions (Fig. 5.6). This leads to the alternating Heisenberg chain behaviour as inferred by the susceptibility of  $\text{Sr}_{14}\text{Cu}_{24}\text{O}_{41}$  [51] and is eventually also of relevance for  $\text{Sr}_{0.73}\text{CuO}_2$  and  $\text{Ca}_{0.83}\text{CuO}_2$ . On the other hand, however, one expects that a sufficiently high degree of disorder, which disturbs the magnetic correlations within the chain, would prevent the formation of a magnetically ordered state. A spin-glass phase could then be stabilised. Nonetheless, the results presented in this chapter showed rigorously that the magnetic order in  $\text{Ca}_{0.83}\text{CuO}_2$  and  $\text{Sr}_{0.73}\text{CuO}_2$  not only takes place locally,

but that a long-range 3D ordered state is established throughout the sample.

In summary, from the discussion in this chapter it can be gathered that the AF ordered state of  $\text{Ca}_{0.83}\text{CuO}_2$  and  $\text{Sr}_{0.73}\text{CuO}_2$  at  $T \sim 10$  K is of long-range 3D character [34]. Whether this state coexists at low temperatures with a dimerised phase as in doped  $\text{CuGeO}_3$  cannot be clarified with the experiments illustrated hitherto. Inelastic neutron scattering experiments discussed in the next chapter will prove indispensable in this context.

Seite Leer /  
Blank leaf

# Chapter 6

## Spin dynamics $\text{Sr}_{0.73}\text{CuO}_2$

### 6.1 Introduction

This chapter presents the perhaps most exciting part of this thesis: the magnetic excitation spectrum of  $\text{Sr}_{0.73}\text{CuO}_2$ . Susceptibility measurements on  $\text{Sr}_{0.73}\text{CuO}_2$  discussed in Chapter 3 gave a first indication of an alternating Heisenberg chain behaviour. The importance of this observation is its implication that a spin excitation gap will exist at low temperatures. If we adhere to the fitting parameters of the static susceptibility, a spin excitation gap of  $\Delta \sim 10$  meV is expected. However, we have seen in Chapter 5 that long-range 3D AF order with a small ferromagnetic component due to spin canting was established in  $\text{Sr}_{0.73}\text{CuO}_2$  at  $T_{\text{AF}} \sim 10$  K [34]. This led to speculation about the possible coexistence of a dimerised and an AF ordered state in  $\text{Sr}_{0.73}\text{CuO}_2$ . The analysis of the static susceptibility, however, was controversial because the typical precipitous drop in susceptibility at low temperatures for a system with a spin gap was masked by a large Curie-type “impurity term,” which hampered an unambiguous interpretation of the low-temperature data. Whereas the energy scale was fixed reliably with the position of the maximum in  $\chi(T)$ , a reasonable fit was obtained for a broad range of the alternation parameter  $\alpha$  [compare Figs. 3.5(a), (b), and (c)]. To confirm the existence of dimerised spins and to achieve a detailed understanding of the spin correlations in  $\text{Sr}_{0.73}\text{CuO}_2$ , it is necessary to study the magnetic excitations using inelastic neutron scattering.

This chapter reports the spin dynamics of polycrystalline  $\text{Sr}_{0.73}\text{CuO}_2$  measured by inelastic neutron scattering. Well-defined excitations at  $E = 10$  and 17.5 meV are observed in the spectrum. Additional magnetic scattering remains present up to  $E \sim 25$  meV [36]. This magnetic response is attributed



to excitations of dimerised spin chains. The two peaks are associated with a well-defined triplet magnon branch separated from the singlet ground state by an excitation gap of  $\Delta \sim 10$  meV, whereas the scattering in the region up to  $E \sim 25$  meV is consistent with an excitation continuum. The wave-vector dependence of the scattering intensity yields evidence that the dimers are formed between next-nearest-neighbour Cu atoms. We will show that the dimerised phase coexists with the AF ordered state below  $T_{\text{AF}} \sim 10$  K, indicating coexistence of the quantum-mechanical singlet ground state and the classical Néel ordered state. This result shows that such coexistence is not restricted to the doped spin–Peierls system  $\text{CuGeO}_3$ .

Neutron time-of-flight scattering data were collected using the high-energy transfer chopper spectrometer (HET) at the ISIS pulsed neutron facility at the Rutherford Appleton Laboratory, Chilton, Oxfordshire, United Kingdom [44]. Additional experiments have been performed at the cold neutron multichopper spectrometer IN5 installed at the high-neutron-flux reactor of the Institute Laue Langevin, Grenoble, France [45]. Approximately 15 g of  $\text{Sr}_{0.73}\text{CuO}_2$  powder was sealed in a flat aluminium plate and mounted in a closed-cycle refrigerator and in a helium cryostat for the experiment on HET and IN5, respectively.

## 6.2 Excitation spectrum

Figure 6.1 shows a contour plot of the inelastic neutron scattering spectrum of polycrystalline  $\text{Sr}_{0.73}\text{CuO}_2$  at  $T = 30$  K collected at the spectrometer HET with an incident energy of  $E_i = 40$  meV. Two clear excitations are visible as horizontal red “stripes.” Figure 6.2(a) displays the excitation spectrum summed over the low-angle detector banks (angular range  $9^\circ \leq \phi \leq 29^\circ$ ). The nonmagnetic background due to nuclear and phonon scattering estimated from the high- $Q$  data [magnetic form factor  $F(Q = 9 \text{ \AA}^{-1}) \sim 0$ ] is indicated by the dashed line. Figure 6.2(b) illustrates the scattering intensity after subtraction of this term. The spin excitation gap of  $\Delta \sim 10$  meV is immediately apparent in all these figures. Two peaks at energy transfers of  $E = 10$  and 17.5 meV are resolved in the magnetic response of  $\text{Sr}_{0.73}\text{CuO}_2$ . Moreover a region with magnetic scattering remains present up to  $E \sim 25$  meV.

Let us consider for the analysis of our data again the 1D Heisenberg model with alternating exchange coupling:

$$H = J \sum_i (\mathbf{S}_{2i} \cdot \mathbf{S}_{2i+1} + \alpha \mathbf{S}_{2i} \cdot \mathbf{S}_{2i-1}), \quad (6.1)$$

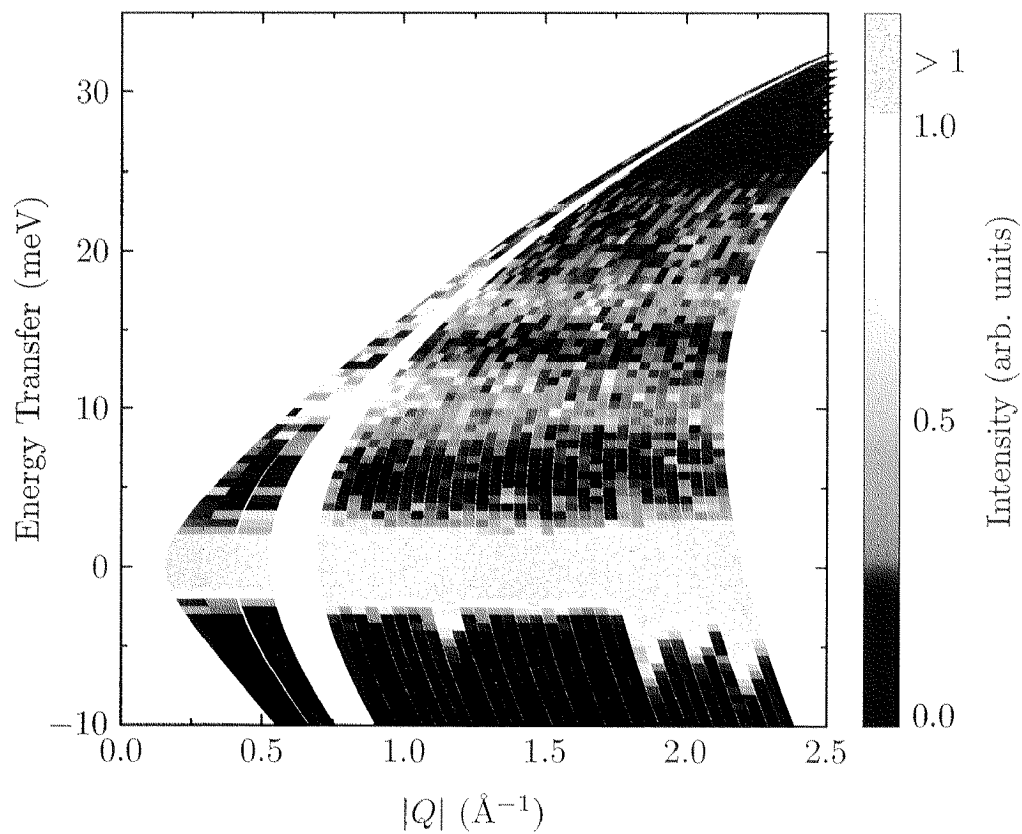


Figure 6.1: Contour plot of the neutron scattering intensity from  $\text{Sr}_{0.73}\text{CuO}_2$  at  $T = 30$  K measured on HET with an incident energy of  $E_i = 40$  meV. Scattering intensity runs from 0 to 1 (arbitrary units). The blank region is the consequence of a small scattering angle not covered by the detectors.

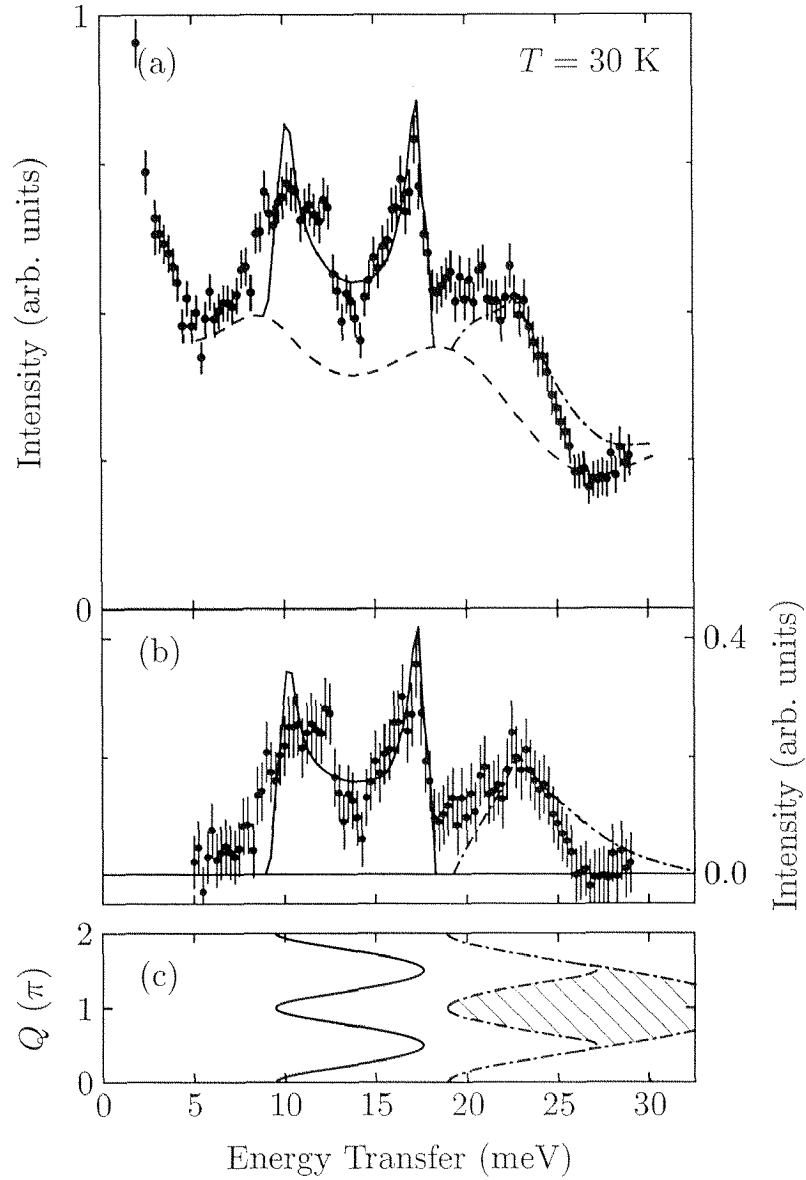


Figure 6.2: (a) Excitation spectrum of  $\text{Sr}_{0.73}\text{CuO}_2$  at  $T = 30$  K for the angular range  $9^\circ \leq \phi \leq 29^\circ$  on HET with  $E_i = 40$  meV. The dashed line represents the non-magnetic scattering. The solid and dash-dotted lines are fits to the density of states of the magnon band and spin excitation continuum, respectively. (b) Scattering intensity after subtraction of the non-magnetic background. Fitting curves as in (a). (c) Calculated excitation spectrum for  $J = 14$  meV and  $\alpha = 0.47$  [117, 118]. The solid line represents the magnon branch. The dash-dotted lines delimit the spin excitation continuum (hatched area).

where  $J$  is the exchange coupling between the spins forming a dimer, and  $\alpha J$  is the coupling between dimers. This model Hamiltonian was previously shown to be adequate for the static magnetic susceptibility of  $\text{Sr}_{0.73}\text{CuO}_2$  (Chapter 3).

In the limit  $\alpha = 1$ , the Hamiltonian corresponds to the isotropic Heisenberg chain. The properties of this model is reasonably well understood, mainly thanks to Bethe's exact solution [3, 119, 120, 121, 122]. The elementary excitations are spinons or domain walls with  $S = 1/2$ , which interpolate between the two ground states [123]. The lowest-lying excitation branch follows  $E = (\pi/2)J|\sin Q|$  [124], i.e., the lowest spinon-pair excitation is gapless. This branch forms the lower boundary of a spin excitation continuum [125]. The upper limit of this continuum is given by  $E = \pi J|\sin(Q/2)|$ . This situation is illustrated in Fig. 6.3(a), which shows the excitation spectrum of a homogeneous Heisenberg chain. This behaviour was recently confirmed experimentally [126]. For  $\alpha < 1$ , the AF chains dimerise and the ground state consists of singlet pairs between spins at  $S_{2i}$  and  $S_{2i+1}$  [123]. The elementary excitations in the case of  $\alpha = 0$  are localised triplets with an excitation gap of  $\Delta = J$ , where one of the spin pairs  $(S_{2i}, S_{2i+1})$  is excited to a triplet. These triplet excitations (magnons) develop a dispersion for  $0 < \alpha < 1$  with an excitation gap of  $\Delta < J$  at the zone centre  $Q = 0$  [127, 128]. This magnon branch is separated from the continuum by a second gap, i.e., the continuum onset at  $Q = 0$  and  $\pi$  is  $2\Delta$  [117, 129]. The excitation spectrum shown in Figs. 6.3(b)–(f) is obtained from the exact results of Bougourzi *et al.* [130] and the numerical approximations of Uhrig and Schulz [117] and Barnes *et al.* [118] with the same convention of  $J$  and  $\alpha$  used here.

In the first approach let us disregard scattering from the excitation continuum. The scattering law powder-averaged over all  $Q$  values is then proportional to the density of states corresponding to the lowest-lying magnon branch. The magnon dispersion relation  $\omega(k)$  is determined analytically using perturbation theory about the isolated dimer limit by Harris to  $O(\alpha^3)$  [76]

$$\begin{aligned} \hbar\omega/J = & 1 - \frac{1}{16}\alpha^2 + \frac{3}{64}\alpha^3 - \left(\frac{1}{2}\alpha + \frac{1}{4}\alpha^2 - \frac{1}{32}\alpha^3\right) \cos(2Q) \\ & - \left(\frac{1}{16}\alpha^2 + \frac{1}{32}\alpha^3\right) \cos(4Q) - \frac{1}{64}\alpha^3 \cos(6Q). \end{aligned} \quad (6.2)$$

This was recently confirmed and extended by Barnes *et al.* to  $O(\alpha^5)$  [118]. A peak in the scattering intensity occurs at the band maximum and minimum due to the Van Hove singularity in the density of states. Using this argument, a contribution to the scattering intensity over the band width  $(1 - \alpha/2) \lesssim E/J \lesssim (1 + \alpha/2)$ , with a large scattering intensity at the two singularities in the density of states at  $E/J \sim (1 \pm \alpha/2)$ , is expected. The solid line in

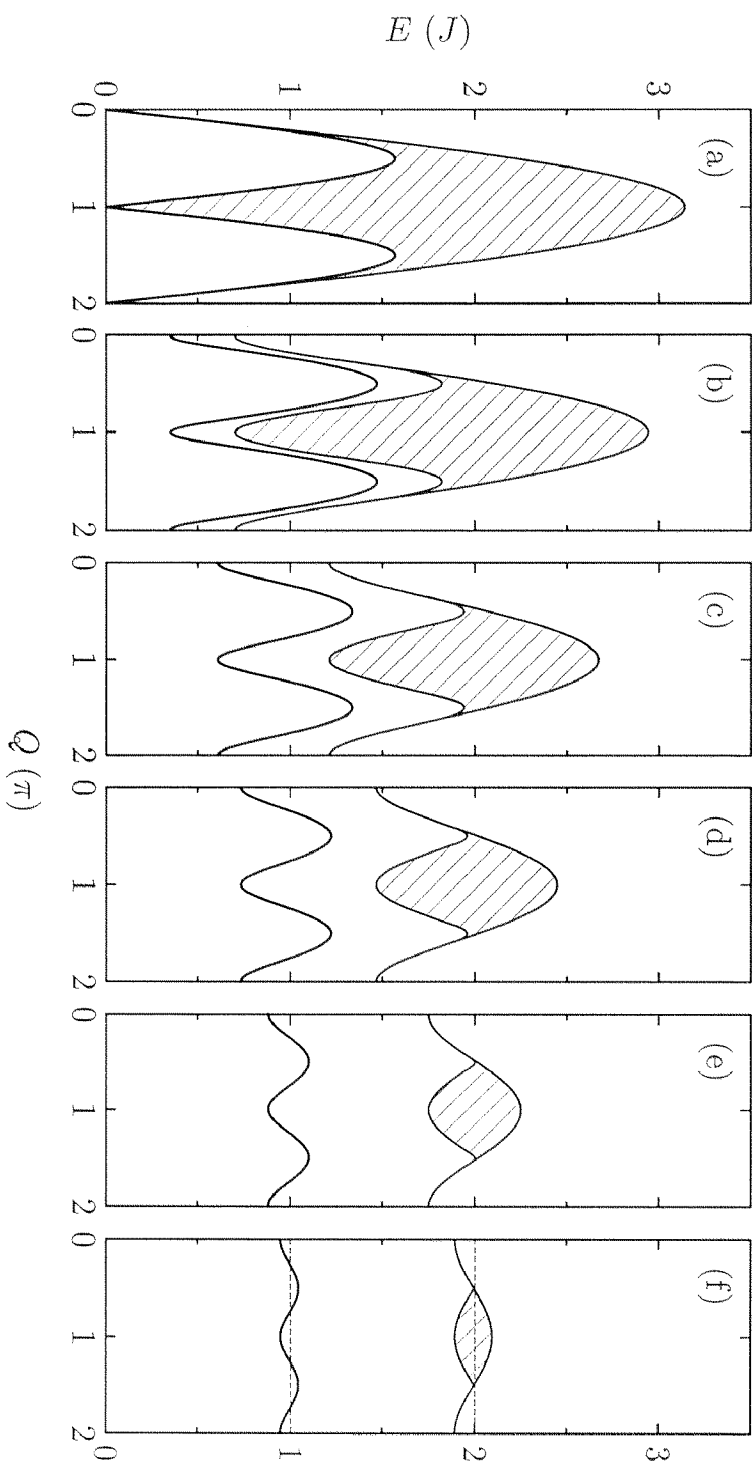


Figure 6.3: Normalised excitation spectrum for alternating Heisenberg chain  $\mathcal{H} = J \sum_i (\mathbf{S}_{2i} \cdot \mathbf{S}_{2i+1} + \alpha \mathbf{S}_{2i} \cdot \mathbf{S}_{2i-1})$ . Alternation  $\alpha = 1, 0.8, 0.6, 0.4, 0.2$ , and  $0.1$  in (a), (b), (c), (d), (e), and (f), respectively. The isolated dimer limit ( $\alpha = 0$ ) is indicated by the dashed lines in (f). Hatched areas are the spin excitation continua.

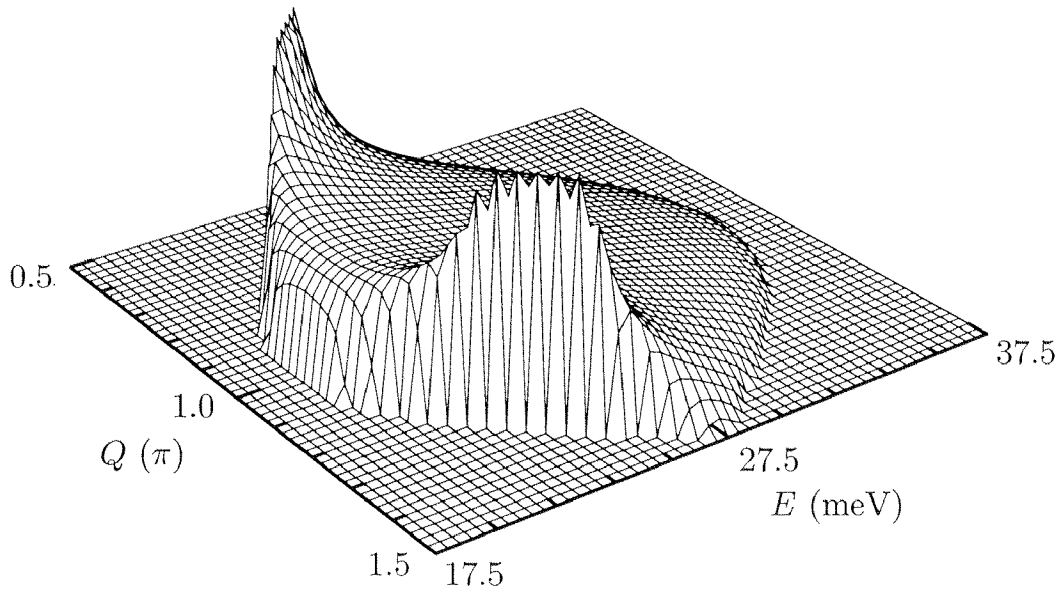


Figure 6.4: Intensity of the excitation continuum (arb. units) as function of  $Q$  and  $E$  for  $J = 14$  meV and  $\alpha = 0.47$ . Intensity is zero for  $0 \leq Q/\pi \leq 0.5$  and  $1.5 \leq Q/\pi \leq 2$  [117].

Figs. 6.2(a) and (b) is a fit to the data where the experimental resolution function has been included. The fit with the aid of Eq. (6.2) yields  $J = 14.0(6)$  meV and  $\alpha = 0.47(2)$ , in accordance with the values deduced from susceptibility measurements discussed in Chapter 3 [ $J/k_B = 174(8)$  K  $\Leftrightarrow J = 15.0(7)$  meV and  $\alpha = 0.5(1)$ ]. We adhere to the fitting parameters obtained by neutron scattering, in view of the uncertainties involved in the determination of, especially,  $\alpha$  from the susceptibility. There is still some magnetic scattering outside the region modelled with this elementary magnon band. This scattering might originate from the continuum of excitations. The theoretical spectrum for the parameters  $J = 14$  meV and  $\alpha = 0.47$ , in the spirit of the calculation by Uhrig and Schulz [117], is displayed in Fig. 6.2(c). The solid line represents the lowest-lying triplet branch [identical to the dispersion Eq. (6.2)]. The continuum is indicated by the hatched area. Using the weakly coupled dimer limit an approximation to  $O(\alpha)$  of the spectral density was devised in Ref. [117]. If we assume that the weak coupling approximation is adequate even for  $\text{Sr}_{0.73}\text{CuO}_2$  (with  $\alpha \sim 0.5$ ), the main characteristics of the continuum illustrated in Fig. 6.4 would remain preserved. The density of states of the continuum therefore has a sharp maximum at  $E/J \sim (2 - \alpha/2)$ , which diminishes at  $E/J \sim (2 - \alpha)$  and

$E/J \sim (2 + \alpha)$ . The fit displayed in Figs. 6.2(a) and (b) (dash-dotted lines) shows that the scattering intensity near  $E = 22.5$  meV can be accounted for by the continuum density of states. Admittedly, it is evident that only a qualitative comparison should be made as  $\alpha \sim 0.5$  in  $\text{Sr}_{0.73}\text{CuO}_2$ .

### 6.3 $Q$ dependence scattering intensity

We have seen above that the alternating chain Heisenberg Hamiltonian Eq. (6.1) can account for the observed energy-transfer dependence of the scattering intensity. Additional evidence of the dimer picture can be obtained from the  $Q$  dependence of the scattering intensity. A maximum in  $S(Q)$ , the Fourier transform of the spin-spin correlation function, is expected corresponding to the distance  $R$  between the spins forming the dimer. In order to obtain  $R$  we take recourse to the relation for the powder average of the structure factor for dimers (Refs. [131, 132] and Appendix 6.5)

$$I(Q) \propto [F(Q)]^2 \left( 1 - \frac{\sin(QR)}{QR} \right), \quad (6.3)$$

where  $F(Q)$  is the magnetic form factor of  $\text{Cu}^{2+}$  and  $R$  is the separation between the spins that form the dimers. The use of the dimer limit ( $\alpha = 0$ ) might seem fallacious. However, only a minor deviation from Eq. (6.3) is expected for coupled dimers ( $\alpha \neq 0$ ). The proof of this is presented in Section 6.5.2, in which the powder average structure factor for coupled dimers is derived to  $O(\alpha^3)$ .

The  $Q$  dependence of the neutron intensity integrated between  $E = 8$  and 20 meV is displayed in Fig. 6.5. A broad maximum in the scattering intensity is observed at  $Q = 0.7(1) \text{ \AA}^{-1}$ . The solid line in Fig. 6.5 is a fit of Eq. (6.3) to the data. A quadratic term has been included to account for the phonon contribution, which increases with  $Q$ . The fit yields a spin separation  $R = 5.4(1) \text{ \AA}$ . As the nearest-neighbour Cu–Cu distance in the chain is  $2.72 \text{ \AA}$  [27],  $R = 5.4(1) \text{ \AA}$  shows that the dimers are formed between next-nearest-neighbour Cu ions. Alternatively, nearest-neighbour Cu dimers would have caused maximum scattering at  $Q \sim 1.7 \text{ \AA}^{-1}$ , which is clearly at odds with our data. The exchange  $J$  between the spins forming a dimer is thus mediated over a nonmagnetic hole along the Cu–O–O–Cu bonds. It is interesting to note that this picture resembles the situation in  $\text{Sr}_{14}\text{Cu}_{24}\text{O}_{41}$ , where dimers are formed between next-nearest-neighbour Cu ions too [104, 105, 106].

Concerning the spin/charge density waves in diluted spin chains with localised holes, they may be understood in a qualitative way by considering a system with competing nearest-neighbour and next-nearest-neighbour

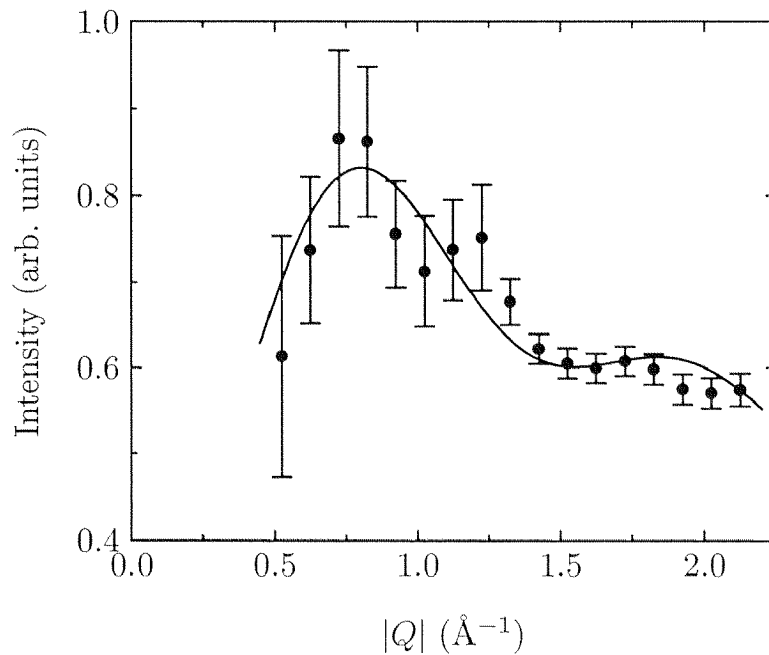


Figure 6.5:  $Q$  dependence of the neutron intensity integrated between  $E = 8$  and 20 meV. The solid line is a fit using the dimer structure factor.

exchange couplings

$$\mathcal{H} = J_1 \sum_i \mathbf{S}_i \cdot \mathbf{S}_{i+1} + J_2 \sum_i \mathbf{S}_i \cdot \mathbf{S}_{i+2}. \quad (6.4)$$

This model has various magnetic phases depending on the relative magnitudes of  $J_1$  and  $J_2$ : see, for example, Refs. [133, 134]. In Chapter 4, p. 41, we saw that in  $\text{CuO}_2$  chains with a Cu–O–Cu bond angle  $\theta$  of about  $90^\circ$ , the next-nearest-neighbour coupling  $J_2$  is AF and typically larger than the nearest-neighbour coupling  $J_1$ . Moreover,  $J_1$  is ferromagnetic for  $90^\circ \lesssim \theta \lesssim 94^\circ$  and AF for  $94^\circ \lesssim \theta < 180^\circ$  [83]. Accordingly, Fig. 6.6(a) displays the classical ground state when all Cu sites are occupied with a spin (spontaneous dimerisation present in some frustrated quantum spin chains is neglected [133, 134]). As  $|J_2| > |J_1|$ , the system may lower its energy by aligning all next-nearest-neighbour spins antiparallel [depicted in Fig. 6.6(a)]. Consequently, half of the nearest-neighbour bonds is frustrated. Upon hole doping or, naively speaking, removing spins from the system, it is energetically most favourable to “remove” these frustrated bonds. For a doping of  $1/2$  holes/Cu, the situation illustrated in Fig. 6.6(b) is reached, where all frustrated bonds are eliminated and an antiparallel spin arrangement is favoured. Denoting the nearest-neighbour  $\text{Cu}^{2+}$  coupling by  $J$ , a resemblance with the homo-



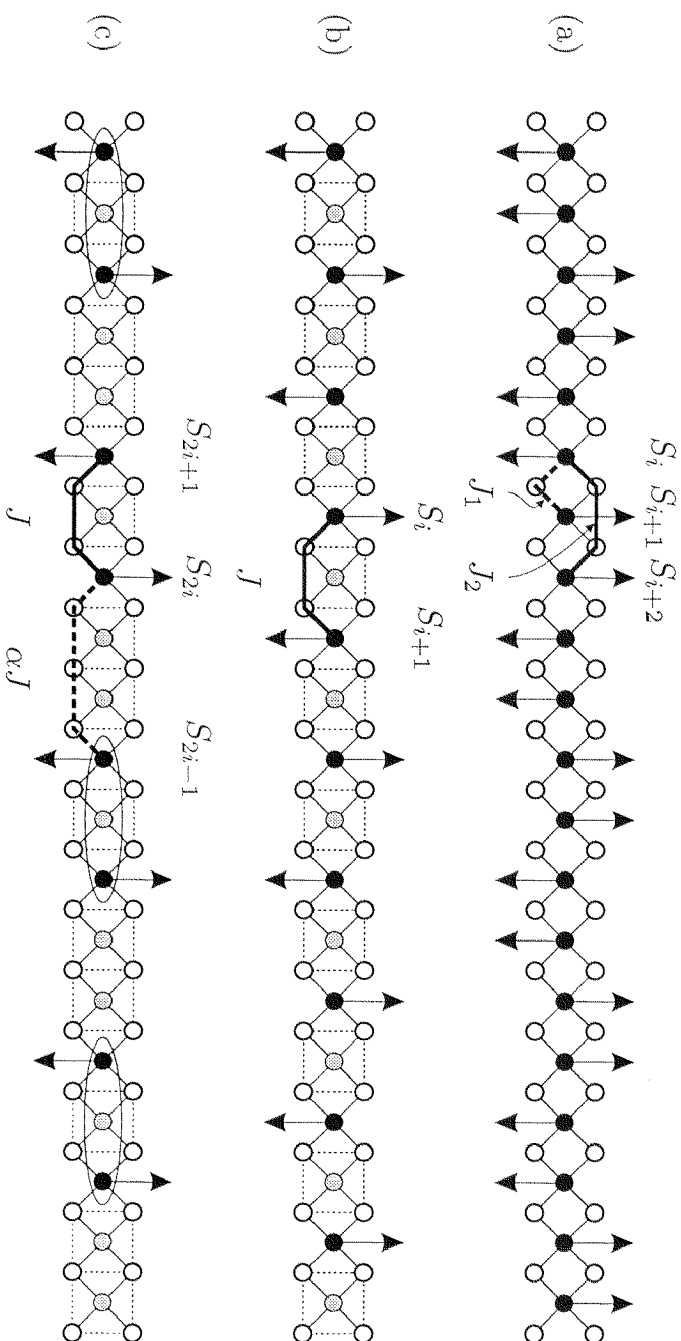


Figure 6.6: (a) Competing nearest-neighbour  $J_1$  and AF next-nearest-neighbour  $J_2$  exchange couplings with  $|J_1| < |J_2|$ ,  $\mathcal{H} = J_1 \sum_i \mathbf{S}_i \cdot \mathbf{S}_{i+1} + J_2 \sum_i \mathbf{S}_i \cdot \mathbf{S}_{i+2}$ . Coupling  $J_1$  is frustrated. (b) Hypothesised picture for doping 1/2 holes/Cu; frustration is eliminated and an effective “homogeneous” Heisenberg chain  $\mathcal{H} = J \sum_i \mathbf{S}_i \cdot \mathbf{S}_{i+1}$  is obtained, where  $i$  is summed only over  $\text{Cu}^{2+}$  sites. (c) Doping 3/5 holes/Cu. Owing to the topological distribution of  $\text{Cu}^{2+}$ , alternating exchange coupling is obtained  $\mathcal{H} = J \sum_i (\mathbf{S}_{2i} \cdot \mathbf{S}_{2i+1} + \alpha \mathbf{S}_{2i} \cdot \mathbf{S}_{2i-1})$ ,  $i$  being summed only over  $\text{Cu}^{2+}$  sites. This picture is valid for  $\text{Sr}_{14}\text{Cu}_{24}\text{O}_{41}$  [104].

geneous chain  $\mathcal{H} = J \sum_i \mathbf{S}_i \cdot \mathbf{S}_{i+1}$  is found. If more holes are introduced a situation depicted in Fig. 6.6(c), which illustrates the case for 3/5 holes/Cu (valid for  $\text{Sr}_{14}\text{Cu}_{24}\text{O}_{41}$  [104] and probably akin to  $\text{Sr}_{0.73}\text{CuO}_2$ ), might be energetically favourable. For this topological distribution of spins there are two unequal exchange constants, which alternate along the chain, i.e., an alternating Heisenberg chain  $\mathcal{H} = J \sum_i (\mathbf{S}_{2i} \cdot \mathbf{S}_{2i+1} + \alpha \mathbf{S}_{2i} \cdot \mathbf{S}_{2i-1})$  is formed, with  $J$  and  $\alpha J$  as indicated in the figure. Moreover, the experimental finding that the dimers in  $\text{Sr}_{0.73}\text{CuO}_2$  are formed between next-nearest-neighbour Cu ions appears in a straightforward way.

## 6.4 Low-temperature spectrum

Having gained confidence in the dimer picture, one could expect that the excitation gap  $\Delta$  is suppressed when a long-range 3D AF ordered phase is formed at  $T \lesssim 10$  K. To check this, let us examine the excitation spectrum at  $T = 1.5$  K on the spectrometer IN5. With this cold neutron instrument one is limited to energy transfers of  $E \lesssim 14$  meV.

Figures 6.7(a) and (b) show the neutron intensity summed over the low-angle banks ( $2^\circ \leq \phi \leq 42^\circ$ ) at  $T = 1.5$  and 20 K, respectively. The data have been corrected for background and detector efficiency. For comparison the data at  $T = 30$  K from HET are displayed in Fig. 6.7(c). A Gaussian fit to the peak at  $E \sim 10$  meV is shown as a guide to the eye. The spin gap  $\Delta = 10(2)$  meV is resolved for  $T = 1.5$  and 20 K as well. No change in the excitation spectrum is observed when crossing the magnetic ordering temperature at  $T_{\text{AF}} \sim 10$  K. This corroborates that the dimer state coexists with the Néel ordered state in  $\text{Sr}_{0.73}\text{CuO}_2$  at  $T < T_{\text{AF}}$ . These two different ground states are generally mutually exclusive with only one exception known up to now: the doped spin–Peierls system  $\text{CuGeO}_3$ . Our finding shows that such a fascinating coexistence is not restricted to a spin–Peierls system.

A physical picture put forward to describe such a coexistence in the Zn-doped  $\text{CuGeO}_3$  assumes that a Zn impurity breaks up one dimer, leaving behind a  $S = 1/2$  local moment [illustrated in Figs. 6.8(a) and (b)]. It was predicted that these moments can strongly enhance long-range AF fluctuations [25, 26], which coexist with the underlying dimerisation at an energy scale lower than the spin–Peierls gap energy. These fluctuations may induce a magnetic ordering via the interchain coupling at  $T_N < T_{\text{SP}}$  [24].

Is this picture also applicable to  $\text{Sr}_{0.73}\text{CuO}_2$ , where the dimerisation is due to the ordering of Zhang–Rice singlets (resulting in a combined spin-charge density wave), and not to a spin–Peierls transition? We have seen above that dimers are formed between next-nearest-neighbour  $\text{Cu}^{2+}$  spins separated by

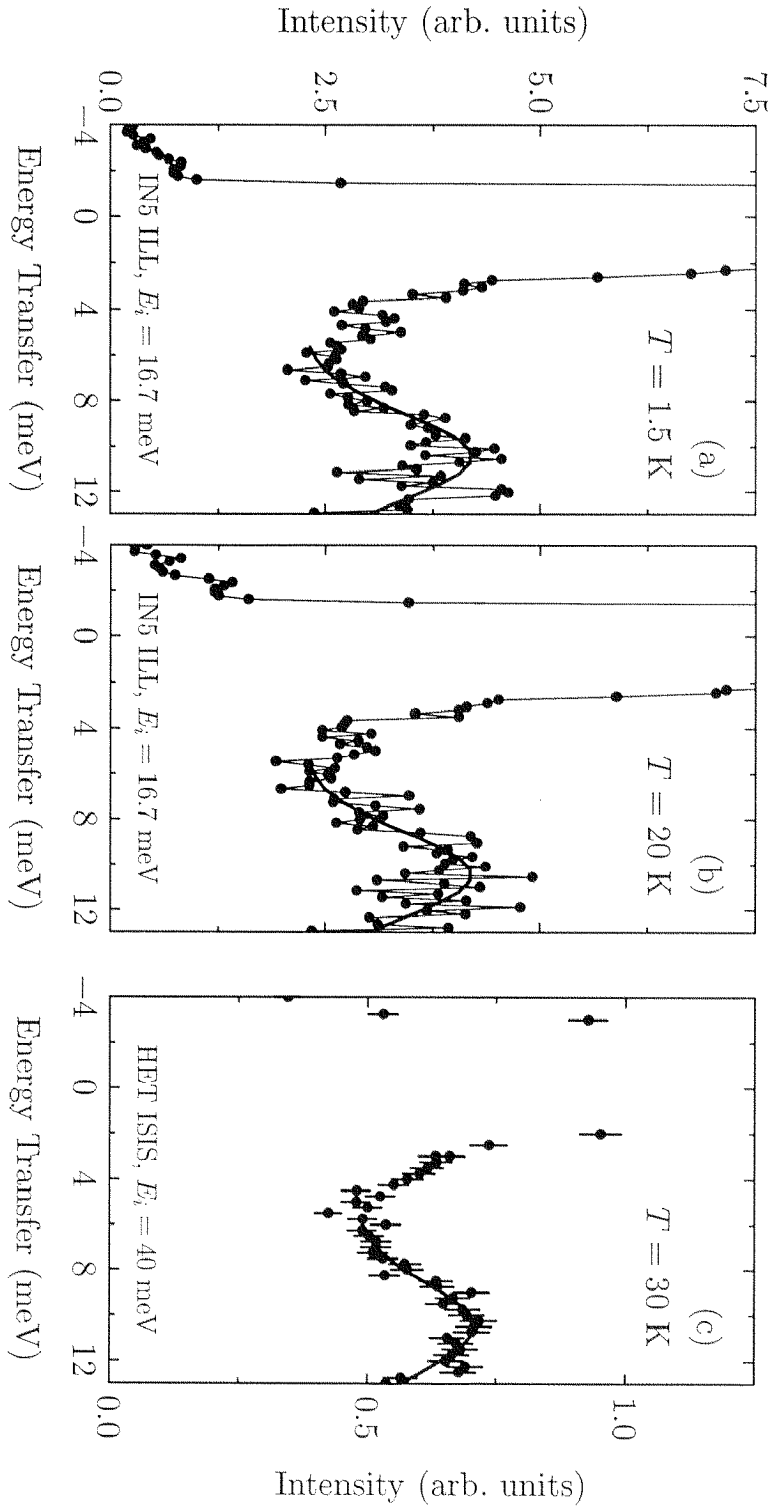


Figure 6.7: Scattering intensity from  $\text{Sr}_{0.73}\text{CuO}_2$  at (a)  $T = 1.5$  K and (b)  $T = 20$  K measured on IN5 with  $E_i = 16.7$  meV. (c) The scattering intensity measured on HET at  $T = 30$  K is shown for comparison. The Gaussian curves are guides to the eye.

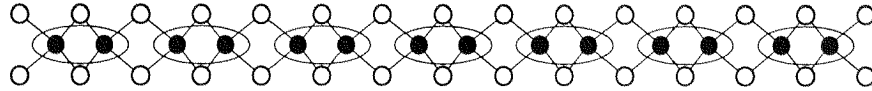
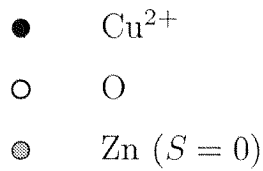
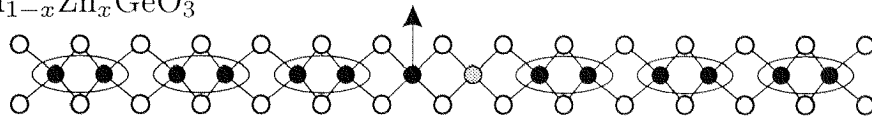
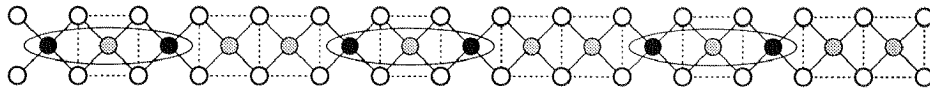
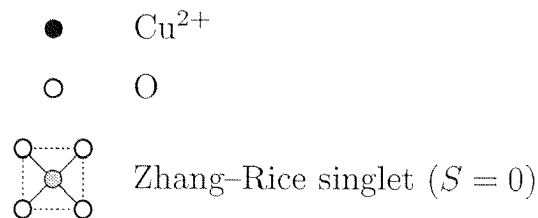
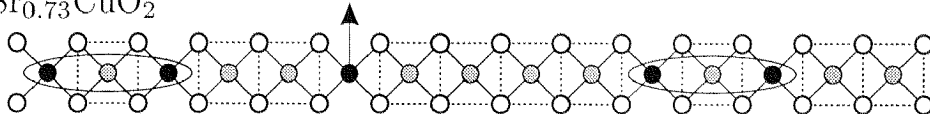
(a)  $\text{CuGeO}_3$ (b)  $\text{Cu}_{1-x}\text{Zn}_x\text{GeO}_3$ (c)  $\text{Sr}_{0.73}\text{CuO}_2$ (d)  $\text{Sr}_{0.73}\text{CuO}_2$ 

Figure 6.8: (a) Dimerised state in  $\text{CuGeO}_3$ . (b) Zn doping in  $\text{CuGeO}_3$  breaks up a dimer, leaving behind a free  $\text{Cu}^{2+}$  spin. (c) Model for the dimerised state in  $\text{Sr}_{0.73}\text{CuO}_2$  requiring *exactly* 0.6 holes/Cu. (d) Model for  $\text{Sr}_{0.73}\text{CuO}_2$  with *approximately* 0.6 holes/Cu.

a nonmagnetic hole. If we assume a dimer–dimer separation of three Cu–Cu distances [135], this corresponds to a doping of *exactly* 0.6 holes/Cu, basically the value we expect in  $\text{Sr}_{0.73}\text{CuO}_2$ . The topological spin distribution for this case is illustrated in Fig. 6.8(c). The remaining holes (spins) not taking part in the dimerisation might act as nonmagnetic (magnetic) impurities [Fig. 6.8(d)], resembling the situation in doped  $\text{CuGeO}_3$ . Moreover, the “free” spins would cause a strong increase of the static susceptibility at low temperatures, in agreement with previous measurements discussed in Chapter 3 [32]. Model calculations would be very welcome to substantiate this microscopic picture for  $\text{Sr}_{0.73}\text{CuO}_2$ .

Alternatively, it was proposed that a Néel state can be stabilised by perturbations to the lattice (Si doping on the Ge site) [23]. For  $\text{Ca}_{0.83}\text{CuO}_2$  and  $\text{Sr}_{0.73}\text{CuO}_2$  this argument might also hold, as the incommensurability between the Cu–O and the Ca/Sr sublattice deforms the idealised structure and generates a structural wave modulation of the Cu–O chains [27]. Consistent with preliminary muon spin resonance measurements [136], one expects in both cases a spatially inhomogeneity of the ordered moment size [58].

Some questions about the interpretation of the inelastic neutron scattering spectrum of  $\text{Sr}_{0.73}\text{CuO}_2$  remain. First, the slight broadening of the peak at  $E = 10$  meV is not explained within the model discussed here. A possible explanation is that a given distribution of the dimer–dimer separation contributes to the broadening of the singularities at  $E/J \sim (1 \pm \alpha/2)$ . Moreover, there appears to be a contribution to the scattering under the elastic peak, whose origin is not yet fully understood. A possible explanation for this contribution is that it originates from quasi-elastic paramagnetic scattering from free spins.

In summary, the quantum spin dynamics of polycrystalline  $\text{Sr}_{0.73}\text{CuO}_2$  is successfully investigated by inelastic neutron scattering. An excitation mode with two distinct peaks at  $E = 10$  and 17.5 meV and additional magnetic scattering up to  $E \sim 25$  meV is observed in the spectrum [36]. I assert that this magnetic response arises from excitations of dimerised AF chains. The two peaks are argued to be due to the dispersive magnon branch with a spin excitation gap of  $\Delta \sim 10$  meV. The scattering near  $E = 22.5$  meV is consistent with an excitation continuum. Further support for the dimer model is found in the  $Q$  dependence of the integrated intensity, i.e., the dimers are formed between next-nearest-neighbour Cu ions separated by a nonmagnetic hole. The present measurements indicate that the spin dimer phase coexist with long-range AF order in  $\text{Sr}_{0.73}\text{CuO}_2$  below  $T \sim 10$  K. This exciting finding shows that such coexistence is not restricted to the doped spin–Peierls system  $\text{CuGeO}_3$ .

## 6.5 Appendix: Structure factor of dimers

### 6.5.1 Structure factor of isolated dimers

Identification of the magnetic excitations predicted by the alternating Heisenberg chain model will be facilitated by estimates of their couplings to external probes, such as neutrons (for  $S = 1$  states). Here, we will derive the wave-vector dependence of the powder-averaged scattering intensity of isolated dimers following Ref. [131].

A system of two  $S = 1/2$  spins with isotropic interaction  $J$  has a nondegenerate ground state with  $S = 0$ ,

$$|\Psi_A\rangle = \frac{1}{\sqrt{2}} (|\uparrow\downarrow\rangle - |\downarrow\uparrow\rangle), \quad (6.5)$$

and a triplet excited state with  $S = 1$ ,

$$\begin{aligned} S_z = 0: & \quad |\Psi_B\rangle = \frac{1}{\sqrt{2}} (|\uparrow\downarrow\rangle + |\downarrow\uparrow\rangle), \\ S_z = 1: & \quad |\Psi_C\rangle = |\uparrow\uparrow\rangle, \\ S_z = -1: & \quad |\Psi_D\rangle = |\downarrow\downarrow\rangle. \end{aligned} \quad (6.6)$$

Recall that in general the differential inelastic scattering cross section for unpolarised neutrons is given by Eqs. (2.12) and (2.13) [39, 40]

$$\frac{d^2\sigma}{d\Omega_f dE_f} = r_0^2 \frac{k_f}{k_i} S(\mathbf{Q}, \omega), \quad (6.7)$$

where

$$S(\mathbf{Q}, \omega) = \sum_{\lambda_i, \lambda_f} p_{\lambda_i} \langle \lambda_i | \hat{\mathbf{Q}}_{\perp}^+ | \lambda_f \rangle \langle \lambda_f | \hat{\mathbf{Q}}_{\perp} | \lambda_i \rangle \delta(\hbar\omega + E_{\lambda_i} - E_{\lambda_f}). \quad (6.8)$$

Here  $k_i$  and  $k_f$  are the incident and scattered neutron wave numbers and  $r_0 = \gamma e^2 / m_e c^2 = -0.54 \times 10^{-14}$  m. The sums are taken over initial and final states of the scattering system  $\lambda_i$  and  $\lambda_f$  with energies  $E_{\lambda_i}$  and  $E_{\lambda_f}$ , respectively,  $p_{\lambda_i}$  is the thermal population factor for the initial state, and  $\hat{\mathbf{Q}}$  is the operator form for the magnetic structure factor of the individual dimer

$$\hat{\mathbf{Q}} = F(Q) \left[ \exp(i \frac{1}{2} \mathbf{Q} \cdot \mathbf{d}) \hat{\mathbf{S}}_2 + \exp(-i \frac{1}{2} \mathbf{Q} \cdot \mathbf{d}) \hat{\mathbf{S}}_1 \right], \quad (6.9)$$

where  $d$  is the interdimer spin separation, and  $F(Q)$  is the atomic magnetic form factor. The subscript  $\perp$  indicates a projection onto a plane perpendicular to the scattering vector. The evaluation of the matrix elements leads to the following form for the energy-loss part of  $S(\mathbf{Q}, \omega)$  at  $T = 0$ :

$$S(\mathbf{Q}, \omega) = S_{\Psi_A \rightarrow \Psi_B} + S_{\Psi_A \rightarrow \Psi_C} + S_{\Psi_A \rightarrow \Psi_D}, \quad (6.10)$$

with

$$S_{\Psi_A \rightarrow \Psi_C} = S_{\Psi_A \rightarrow \Psi_D} = \frac{1}{2} S_{\Psi_A \rightarrow \Psi_B} = \frac{1}{2} [F(Q)]^2 \sin^2\left(\frac{1}{2} \mathbf{Q} \cdot \mathbf{d}\right) \delta(\hbar\omega - \Delta), \quad (6.11)$$

where  $\Delta = J$  is the singlet-triplet energy gap.

To obtain the intensity measured in a powder experiment we perform an average of the scattering law over the relative orientation of  $\mathbf{Q}$  and  $\mathbf{d}$ . The powder average of the structure factor is given by

$$S(Q, \omega) = [F(Q)]^2 \frac{1}{4\pi Q^2} \iint_{\substack{\mathbf{q}=\mathbf{q}_{\parallel}+\mathbf{q}_{\perp} \\ q=Q}} S(\mathbf{q}_{\parallel}, \omega) d\mathbf{q}, \quad (6.12)$$

where  $\mathbf{q}_{\parallel}$  and  $\mathbf{q}_{\perp}$  are the parallel and perpendicular projections of the total momentum transfer  $\mathbf{q}$  relative to the chain axis [137]. For any given  $Q$  all values of  $|\mathbf{q}_{\parallel}| \leq Q$  will contribute to the scattering spectrum. Taking spherical coordinates (with Jacobian determinant  $Q^2 \sin \phi$ ) and the appropriate integration limits to get a one-to-one mapping, the integral in Eq. (6.12) reads [131, 132]

$$\begin{aligned} S(Q) &= [F(Q)]^2 \frac{1}{4\pi Q^2} \int_{\theta=0}^{2\pi} d\theta \int_{\phi=0}^{\pi} d\phi 2Q^2 \sin \phi \sin^2\left(\frac{1}{2} Qd \cos \phi\right) \\ &= [F(Q)]^2 \left(1 - \frac{\sin(Qd)}{Qd}\right). \end{aligned} \quad (6.13)$$

And finally

$$\frac{d^2\sigma}{d\Omega_f dE_f} = r_0^2 \frac{k_f}{k_i} N [F(Q)]^2 \left(1 - \frac{\sin(Qd)}{Qd}\right) \delta(\hbar\omega - \Delta), \quad (6.14)$$

where  $N$  is the number of dimers in the sample. The cross section has a maximum at  $Q = 1.50\pi/d$ . The powder average of the structure factor for dimers causes a  $Q$  dependence of the scattering intensity [131, 132]

$$I(Q) \propto [F(Q)]^2 \left(1 - \frac{\sin(Qd)}{Qd}\right). \quad (6.15)$$

This makes the  $Q$  dependence of the magnetic excitation especially interesting in that it allows the separation  $d$  of the magnetic ions forming the dimer pair to be determined.

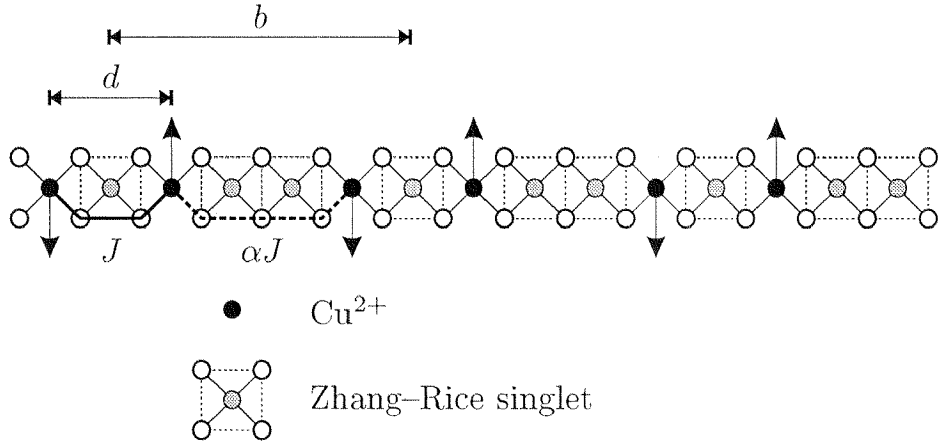


Figure 6.9: Geometry of an alternating chain. The exchange coupling between the two spins forming a dimer is  $J$  (solid line) and the dimer extent is  $d$ . The coupling between dimers is  $\alpha J$  (dashed line). The spacing between dimer centres is  $b$ .

### 6.5.2 Structure factor for coupled dimers

The geometry of the chain with alternating exchange coupling is shown in Fig. 6.9. The internal dimer spin-spin interaction is  $J$ , and the coupling between dimers is  $\alpha J$ . The structure factor for such a dimer chain is calculated to  $O(\alpha^3)$  by Barnes *et al.* [118],

$$\begin{aligned}
 S(\mathbf{Q}) &= [F(Q)]^2 [1 - \cos(\mathbf{Q} \cdot \mathbf{d})] \\
 &\times \left[ 1 - \frac{5}{16}\alpha^2 - \frac{3}{32}\alpha^3 + \left( \frac{1}{2}\alpha - \frac{1}{8}\alpha^2 - \frac{5}{192}\alpha^3 \right) \cos(\mathbf{Q} \cdot \mathbf{b}) \right. \\
 &\quad \left. + \left( \frac{3}{16}\alpha^2 + \frac{7}{48}\alpha^3 \right) \cos(2\mathbf{Q} \cdot \mathbf{b}) + \frac{5}{64}\alpha^3 \cos(3\mathbf{Q} \cdot \mathbf{b}) \right], \quad (6.16)
 \end{aligned}$$

where  $d$  is the intradimer distance and  $b$  is the interdimer distance. The term  $1 - \cos(\mathbf{Q} \cdot \mathbf{d})$  [which equals  $2 \sin^2(\frac{1}{2}\mathbf{Q} \cdot \mathbf{d})$ ] describes the isolated dimer contribution. This yields the basic intensity “envelope” that measures the separation between the spins that form a dimer. The separation between dimer centres  $b$  enters as a more rapid modulation  $1 + (\alpha/2) \cos(\mathbf{Q} \cdot \mathbf{b})$  to



$O(\alpha)$ . The powder average structure factor to  $O(\alpha)$  yields

$$\begin{aligned}
 S(Q) &= [F(Q)]^2 \frac{1}{4\pi Q^2} \int_{\theta=0}^{2\pi} d\theta \int_{\phi=0}^{\pi} d\phi Q^2 \sin \phi [1 - \cos(Qd \cos \phi)] \\
 &\quad \times \left[ 1 + \frac{1}{2}\alpha \cos(Qb \cos \phi) \right] \\
 &= [F(Q)]^2 \left[ 1 - \frac{\sin(Qd)}{Qd} \right. \\
 &\quad \left. + \frac{\alpha}{2} \left( \frac{\sin(Qb)}{Qb} - \frac{\sin[Q(d-b)]}{2Q(d-b)} + \frac{\sin[Q(d+b)]}{2Q(d+b)} \right) \right].
 \end{aligned} \tag{6.17}$$

Figure 6.10 illustrates the powder average of  $S(Q)/[F(Q)]^2$  for different values of  $\alpha$  in various scenarios calculated to  $O(\alpha^3)$  to reach a higher degree of accuracy. The most probable model for the spacial distribution of the spins in  $\text{Sr}_{0.73}\text{CuO}_2$ , i.e.,  $b = 2.5d$ , is represented in Fig. 6.10(b). Furthermore, several curves calculated assuming different values of  $b$  are plotted to give a sense of the sensitivity of the structure factor to this parameter. It is in this respect noteworthy that the powder averaged structure factor is determined almost entirely by the distance between the spins forming the dimers  $d$  and is basically independent of the interdimer separation  $b$  and/or interaction  $\alpha$ . Hence, in the case of polycrystalline  $\text{Sr}_{0.73}\text{CuO}_2$ , it is clearly expedient to use the isolated dimer description [Eq. (6.3)] for the wave-vector dependence of the scattering intensity.

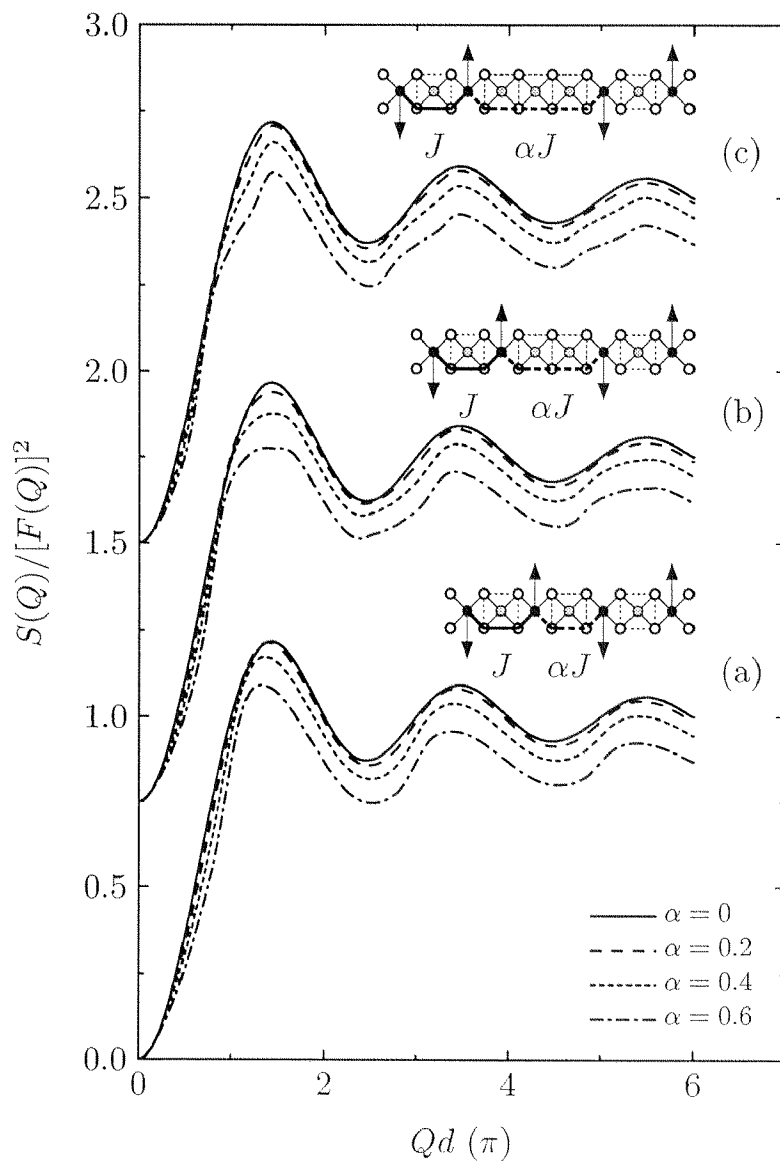


Figure 6.10: Powder average structure factor of dimers. The separation between the spins forming a dimer is  $d$ . The separation between dimer centres is (a)  $b = 2d$ , (b)  $b = 2.5d$ , and (c)  $b = 3d$ . Structure factor  $S(Q)$  is indicated for isolated dimers by the solid line [identical in (a), (b), and (c)]; interacting dimers for  $\alpha = 0.2, 0.4$ , and  $0.6$  by dashed lines, dotted lines, dashed-dotted lines, respectively. Curves in (b) and (c) are offset by  $0.75$  and  $1.5$ , respectively.

Seite Leer /  
Blank leaf

# Chapter 7

## LaTiO<sub>3+δ</sub> upon band filling

### 7.1 Introduction

In the remainder of this thesis I discuss the magnetic properties of the three-dimensional correlated electron system LaTiO<sub>3+δ</sub> ( $0 < \delta \lesssim 0.1$ ). The orthorhombically distorted perovskite LaTiO<sub>3</sub> is a Mott–Hubbard insulator with a small charge gap ( $\sim 0.2$  eV) between the correlated Ti  $3d$  states of the Coulomb-split lower and upper Hubbard band [138, 139, 140]. The nominal valence of Ti in LaTiO<sub>3</sub> is  $3+$  with  $3d^1$  ( $S = 1/2$ ) configuration. Increasing the average valence of Ti leads to the formation of a strongly correlated metal as the gap becomes filled with carriers. This can be realised for example in LaTiO<sub>3+δ</sub> or La<sub>1-x</sub>A<sub>x</sub>TiO<sub>3</sub> ( $A$  is a divalent alkaline earth). A critical enhancement of the effective electron mass was found upon approaching the Mott–Hubbard insulator phase from the metallic side [141, 142]. For low carrier doping, i.e., in LaTiO<sub>3+δ</sub> with off-stoichiometric oxygen  $0 \leq \delta \lesssim 0.08$  [143, 144, 145, 146] or La<sub>1-x</sub>A<sub>x</sub>TiO<sub>3</sub> with  $0 \leq x \lesssim 0.05$  [146, 147], a metal-to-insulator transition occurs at low temperatures. This transition is accompanied by antiferromagnetic (AF) ordering of Ti<sup>3+</sup> moments, with a weak-ferromagnetic component due to spin canting.

The dependence of the electronic and magnetic properties of LaTiO<sub>3</sub> on doping resembles to a certain degree the situation of the high- $T_c$  cuprates [1, 148, 149] and colossal magnetoresistance manganese perovskites [150, 151, 152]. The undoped insulating so-called “parent” compounds of the cuprates and manganates are charge-transfer insulators with the gap formed between the occupied oxygen  $2p$  states and the unoccupied Cu or Mn  $3d$  states of the upper Hubbard band. On changing the effective valence of Cu, i.e., by controlling the filling of the Cu–O related band, the cuprates exhibit a phase

transition from an AF insulator to an unconventional metal through the high- $T_c$  superconductor state. In manganese perovskites based on the AF insulator  $\text{LaMnO}_3$ , an insulator-to-metal transition occurs for some values of hole doping and at a certain temperature, generally associated with the ferromagnetic Curie temperature.

For all these  $3d$  electron systems the band filling control of the parent Mott insulators has been widely recognised as one of the most important aspects of the insulator-to-metal transition [149, 153]. Moreover, it is believed that magnetism strongly affects the electronic system. Therefore, a detailed knowledge of the magnetic properties of the doped Mott-Hubbard insulator  $\text{LaTiO}_{3+\delta}$  might contribute to a better understanding of the insulator-to-metal transition in strongly correlated electron systems.

Moreover, this Mott-Hubbard insulator might serve as a valuable comparison for the previously discussed doped quasi-one-dimensional cuprates with respect to the doping level that can be sustained in a 3D model system. In addition, the  $\text{LaTiO}_{3+\delta}$  system has attracted interest at IBM ZRL as it provides the possibility of tailoring the structure by intercalation of oxygen to obtain artificial insulator-semiconductor superlattices in  $\text{LaTiO}_{3.4}$  to  $\text{LaTiO}_{3.5}$ . These superlattices might create properties that have the functionality needed for future device applications (this subject is not covered in my work). For an elucidating review, see Bednorz in Ref. [154].

This chapter presents neutron-diffraction and magnetic-susceptibility measurements on a series of single crystals of  $\text{LaTiO}_{3+\delta}$  ( $0 < \delta \lesssim 0.08$ ). A significant reduction of the ordered moment size of Ti is observed upon filling the narrow  $d$ -electron band of  $\text{LaTiO}_3$ , i.e., upon increasing  $\delta$  from 0 to  $\sim 0.07(1)$  [35]. This gives further evidence that the spin-ordered phase collapses upon approaching the Mott-Hubbard transition boundary. In the immediate vicinity of the insulator-to-metal transition, i.e., in  $\text{LaTiO}_{3.07}$ , a peculiar magnetisation behaviour is observed. The weak-ferromagnetic saturation moment is reached via a series of steps in the magnetisation curve.

All the  $\text{LaTiO}_{3+\delta}$  single crystals were prepared by floating-zone melting of sintered ceramic bars in a reducing atmosphere. The ceramics were prepared using a mixture of  $\text{La}_2\text{O}_3$ ,  $\text{TiO}$ , and  $\text{TiO}_2$  sintered at  $1350^\circ\text{C}$ . Special attention was paid to the synthesis of samples with  $\delta = 0$ . The oxygen content of the crystals was measured with a thermogravimetric analyser (SETARAM). Only crystals with a homogeneous oxygen content were used in this investigation. Neutron diffraction was performed at the thermal neutron single-crystal diffractometer D15 at the high-neutron-flux reactor of the Institute Laue Langevin, Grenoble, France [46]. The wavelength used was  $\lambda = 1.17 \text{ \AA}$ . The magnetisation was measured with a commercial supercon-

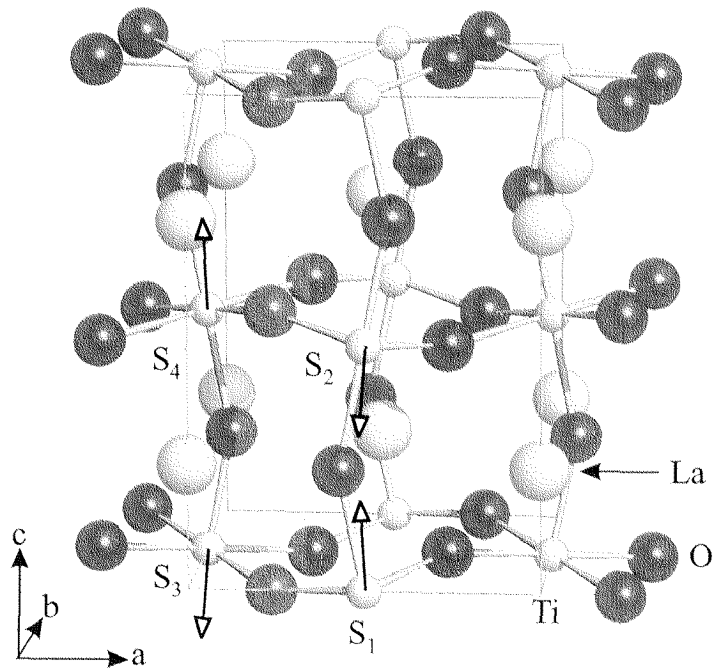


Figure 7.1: Orthorhombic  $Pbnm$  space group of  $\text{LaTiO}_3$  with four distorted perovskite units in the crystallographic unit cell. Unit cell parameters at  $T = 100$  K are  $a = 5.626$  Å,  $b = 5.590$  Å, and  $c = 7.904$  Å. The positions of the Ti spins in the unit cell are labelled  $S_1, \dots, S_4$ . The  $G_z F_x$  magnetic structure is indicated by arrows.

$h k l$	$[I(5 \text{ K}) - I(190 \text{ K})]/I(5 \text{ K})$
1 0 0	$\sim 0$
0 1 0	$\sim 0$
1 0 1	$0.60 \pm 0.09$
0 1 1	$0.59 \pm 0.10$
1 1 1	$\sim 0$

Table 7.1: Relative increase in neutron intensity due to magnetic ordering of  $\text{LaTiO}_{3.000(5)}$  for selected reflections.

ducting quantum interference device (SQUID) magnetometer (Biomagnetic Technologies Inc).

## 7.2 Structure of ordered moment

Let us commence with the investigation of the magnetic structure of  $\text{LaTiO}_{3+\delta}$ . The intensity of 198 Bragg reflections is measured at different temperatures of three twinned single crystals of  $\text{LaTiO}_{3+\delta}$  with  $\delta = 0.000(5)$ ,  $\delta = 0.030(5)$ , and  $\delta = 0.07(1)$ . These crystals are located in that part of the magnetic phase diagram where AF magnetic ordering of the Ti moments is expected.  $\text{LaTiO}_{3+\delta}$  belongs to the orthorhombic space group  $D_{2h}^{16} Pbnm$  with four distorted perovskite units in the crystallographic unit cell, Fig. 7.1. In this space group, a gain in neutron intensity superposed on structural Bragg peaks is expected for AF ordering of Ti moments. For all crystals with  $0 \leq \delta \lesssim 0.08$  we observed magnetic scattering at the same positions. The magnetic contribution to these Bragg peaks decreases with band filling, i.e., with increasing off-stoichiometric oxygen  $\delta$ . For  $\text{LaTiO}_{3.000(5)}$ , the relative increase due to magnetic ordering of Ti moments for some principal reflections is listed in Table 7.1.

The only four magnetic structures with zero propagation vectors that are compatible with  $\text{LaTiO}_{3+\delta}$  crystal symmetry are listed in Table 7.2. In this table, the position of the Ti spins in the crystallographic unit cell are labelled  $S_1(x, y, z) = (1/2, 0, 0)$ ,  $S_2(x, y, z) = (1/2, 0, 1/2)$ ,  $S_3(x, y, z) = (0, 1/2, 0)$ , and  $S_4(x, y, z) = (0, 1/2, 1/2)$ , Fig. 7.1. The position and orientation of these spins are coupled with the symmetry operators  $2z$ ,  $ax$ , and  $ny$ , which relate the Ti spin  $S_1$  to  $S_2$ ,  $S_3$ , and  $S_4$ , respectively. The two orientations of the spins along the indicated  $x$ ,  $y$ , and  $z$  axes are denoted with a plus or minus sign. The three magnetic structures in Table 7.2 with a ferromagnetic

1			$G_x$	$A_y$	$F_z$	2			$A_x$	$G_y$	$C_z$
$I$	$S_1$		+	+	+	$I$	$S_1$		+	+	+
$2z$	$S_2$		-	-	+	$2z$	$S_2$		-	-	+
$ax^\dagger$	$S_3$		-	+	+	$ax$	$S_3$		+	-	-
$ny^\dagger$	$S_4$		+	-	+	$ny$	$S_4$		-	+	-

3			$C_x$	$F_y$	$A_z$	4			$F_x$	$C_y$	$G_z$
$I$	$S_1$		+	+	+	$I$	$S_1$		+	+	+
$2z^\dagger$	$S_2$		+	+	-	$2z^\dagger$	$S_2$		+	+	-
$ax^\dagger$	$S_3$		-	+	+	$ax$	$S_3$		+	-	-
$ny$	$S_4$		-	+	-	$ny^\dagger$	$S_4$		+	-	+

Table 7.2: The four possible magnetic structures for the  $Pbnm$  space group. The symmetry operators  $2z$ ,  $ax$ , and  $ny$  relate the position and orientation of spin  $S_1$  to  $S_2$ ,  $S_3$ , and  $S_4$ , respectively. The orientation of the spins along the indicated  $x$ ,  $y$ , and  $z$  axes are denoted  $+$  or  $-$ .

component  $F$  can account for the weak-ferromagnetic moment previously observed in magnetisation measurements [143, 144, 145, 146]. To distinguish among these three structures, we consider the magnetic structure factors for certain reflections listed in Table 7.3. The significant magnetic intensity observed at the  $(1\ 0\ 1)$  and  $(0\ 1\ 1)$  reflection is compatible with the AF type- $G$  structure. We have essentially zero intensity in the  $(1\ 0\ 0)$ ,  $(0\ 1\ 0)$ , and  $(1\ 1\ 1)$  reflections. This leads to the conclusion that no AF type- $A$  and type- $C$  components are present in the magnetic structure of  $\text{LaTiO}_{3+\delta}$ . The magnetic structure is therefore either  $G_x F_z$  or  $G_z F_x$ , Fig. 7.1. This means that all nearest-neighbour Ti moments are oriented antiparallel in the long-range three-dimensional (3D) ordered phase below the Néel temperature  $T_N$ , in agreement with previous neutron powder-diffraction measurements on  $\text{LaTiO}_{\sim 3.0}$  [155]. Because of the twinning of the crystals we cannot distinguish between  $G_x F_z$  and  $G_z F_x$ .

### 7.3 Temperature dependence of the ordered moment

It is interesting to investigate the evolution of the ordered moment size  $m_{\text{AF}}$  of Ti and its temperature dependence upon band filling. Considering the observed magnetic intensities, we find for  $\text{LaTiO}_{3.000(5)}$  an ordered moment on



$h k l$	Structure factor	Order type	
1 0 1	$-S_1 + S_2 + S_3 - S_4$	$G$	$h + k$ odd, $l$ odd
0 1 1	$S_1 - S_2 - S_3 + S_4$	$G$	
0 0 1	$S_1 - S_2 + S_3 - S_4$	$A$	$h + k$ even, $l$ odd
1 1 1	$-S_1 + S_2 - S_3 + S_4$	$A$	
1 0 0	$-S_1 - S_2 + S_3 + S_4$	$C$	$h + k$ odd, $l$ even
0 1 0	$S_1 + S_2 - S_3 - S_4$	$C$	
1 1 0	$-S_1 - S_2 - S_3 - S_4$	$F$	$h + k$ even, $l$ even

Table 7.3: Magnetic structure factor for selected reflections.

Ti of  $m_{\text{AF}} = 0.46(2)\mu_B$ , where  $\mu_B$  is the Bohr magneton. Upon hole doping, the ordered moment decreases rapidly. For  $\text{LaTiO}_{3.030(5)}$  and  $\text{LaTiO}_{3.07(1)}$ , a moment on Ti of  $0.32(2)\mu_B$  and  $0.09(3)\mu_B$ , respectively, is obtained. The temperature dependence of the ordered moment  $m_{\text{AF}}(T)$  in the three crystals is shown in Fig. 7.2(a). A fit with  $m_{\text{AF}} \propto (1 - T/T_N)^\beta$  in the vicinity of  $T_N$  leads to the respective critical exponents  $\beta = 0.35(3)$  and  $\beta = 0.36(4)$ , for  $\text{LaTiO}_{3.000(5)}$  and  $\text{LaTiO}_{3.030(5)}$ , consistent with the 3D Heisenberg picture.

Generally, an ion with spin  $S$  in a 3D magnetically ordered lattice has an ordered moment of  $g\mu_B S$ , which yields  $\sim 1\mu_B$  for  $S = 1/2$  when  $g \sim 2$ . The smaller ordered moment of  $\sim 0.5\mu_B$  found in  $\text{LaTiO}_3$  is not due to quantum fluctuations. These are known to reduce the ordered moment significantly, e.g., in the cuprates because of a reduced dimensionality [113, 156]. In fact, the ordered moment of  $0.46(2)\mu_B/\text{Ti}$  in the 3D correlated  $\text{LaTiO}_3$  can be explained with an unquenched orbital momentum. In the ionic picture without crystal distortion the orbital magnetisation induced by spin-orbit interaction on the  $t_{2g}$  states is  $1\mu_B$ . The crystal field in  $\text{LaTiO}_3$  splits the degenerate  $t_{2g}$  orbitals and partly quenches the orbital moment. This remaining orbital momentum reduces the total magnetic moment on the Ti sites, in accordance with Hund's third rule. Roughly speaking, the result of this is a strongly reduced "effective"  $g$  factor ( $g \sim 1$ ) [157].

The macroscopic weak-ferromagnetic moment found in the spin-ordered state is due to canting of the AF ordered Ti moments. The canting is driven by the  $\text{GdFeO}_3$ -type distortion [158] of the perovskite lattice. This rotation of the Ti- $\text{O}_6$  octahedra in the orthorhombic phase allows the antisymmetric Dzyaloshinski-Moriya superexchange term

$$\mathcal{H}_{\text{DM}} = \sum_{\langle i,j \rangle} \mathbf{D}_{ij} \cdot (\mathbf{S}_i \times \mathbf{S}_j) \quad (7.1)$$

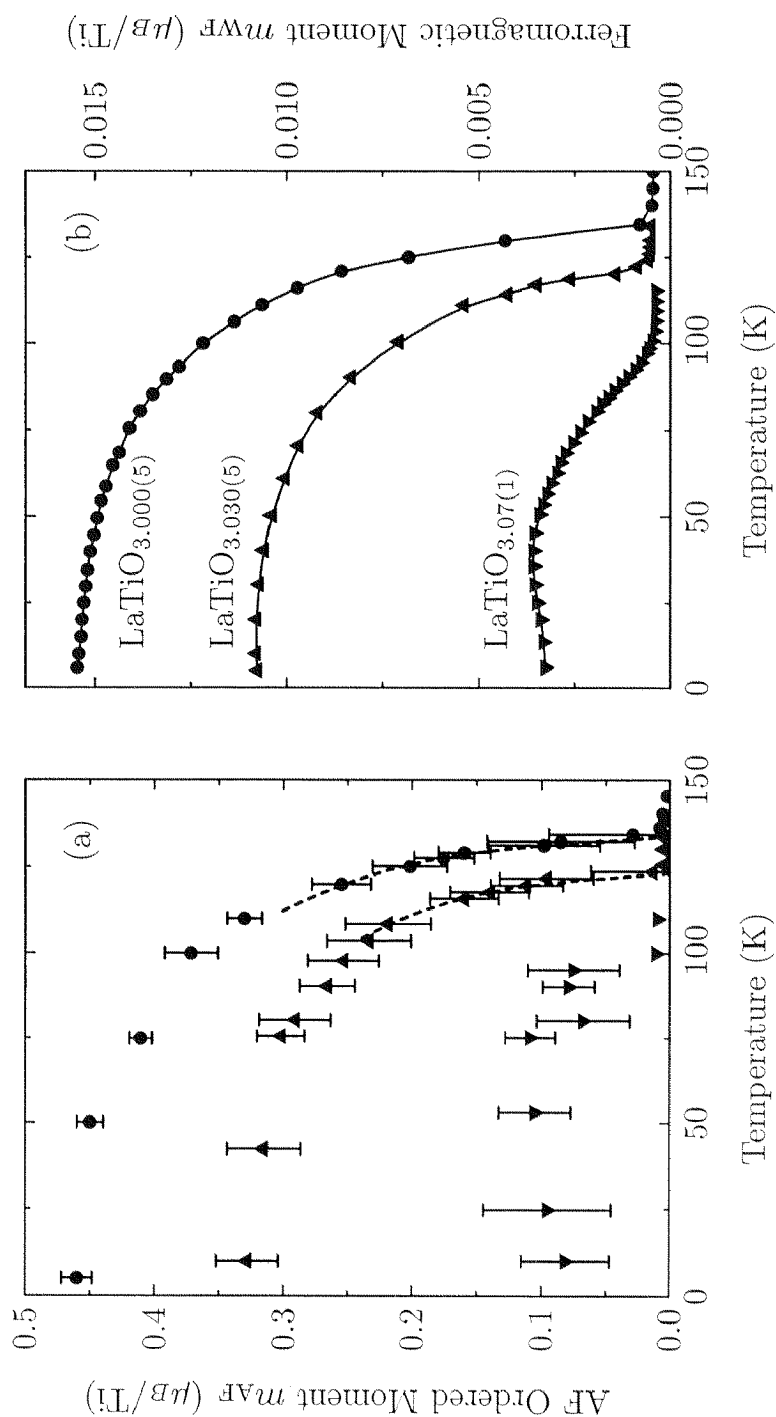


Figure 7.2: (a) Temperature dependence of the AF ordered moment on Ti  $m_{AF}(T)$  of LaTiO<sub>3.000(5)</sub>, LaTiO<sub>3.030(5)</sub>, and LaTiO<sub>3.07(1)</sub>. The dotted lines are fits to  $m_{AF} \propto (1 - T/T_N)^\beta$  with  $\beta = 0.35(3)$  and  $\beta = 0.36(4)$  for LaTiO<sub>3.000(5)</sub> and LaTiO<sub>3.030(5)</sub>, respectively. (b) Temperature dependence of the macroscopic weak-ferromagnetic moment  $m_{WF}(T)$  measured by SQUID magnetometry.

in the spin Hamiltonian. Figure 7.2(b) shows the temperature dependence of the weak-ferromagnetic moment  $m_{\text{WF}}$  for the three  $\text{LaTiO}_{3+\delta}$  crystals as measured by SQUID magnetometry. The AF ordered moment size  $m_{\text{AF}}$ , Fig. 7.2(a), and the weak-ferromagnetic moment  $m_{\text{WF}}$ , Fig. 7.2(b), decrease by the same fraction with an increasing amount of nonstoichiometric oxygen  $0 \leq \delta \lesssim 0.08$ . This indicates that, within the error, the reduction of the macroscopic weak-ferromagnetic moment can be understood in terms of a decreased moment on Ti without a change in canting angle ( $\sim 1.7^\circ$ ).

Figure 7.3 shows the dependence of the ordered moment  $m_{\text{AF}}$  versus Néel temperature  $T_N$ . Data on the weak-ferromagnetic moment  $m_{\text{WF}}$  of several additional  $\text{LaTiO}_{3+\delta}$  crystals with  $0 \leq \delta \lesssim 0.08$ , which was shown to be a good measure of  $m_{\text{AF}}$  (see above), is included. The size of the ordered moment of Ti reaches a maximum of  $0.46(2)\mu_B$  for  $\text{LaTiO}_{3.000(5)}$ . With increasing band filling, the moment decreases rapidly and long-range 3D order is suppressed for  $\delta \gtrsim 0.08$ , i.e., for more than  $\sim 0.16$  holes/Ti. Surprisingly,  $T_N(m_{\text{AF}})$  does not extrapolate to zero, which prompted us to speculate about a collapse of  $T_N$  as  $m_{\text{AF}} \rightarrow 0$  in the vicinity of the Mott–Hubbard transition. It is interesting to compare this behaviour with the situation found in cuprates and manganates. The ordered moment size in the AF ordered phase of  $\text{YBa}_2\text{Cu}_3\text{O}_{6+\delta}$  or  $\text{La}_2\text{CuO}_{4+\delta}$  as determined by magnetic neutron scattering has a maximum of  $m_{\text{AF}} \sim 0.6\mu_B$  for  $\delta \sim 0$  [156, 159]. This limit is in agreement with the theoretical prediction for a  $S = 1/2$  2D Heisenberg AF [113]. With increasing  $\delta$ , i.e., by controlling the filling of the Cu–O related band, the ordered moment size of  $\text{Cu}^{2+}$  is reduced, accompanied by a strong decrease in  $T_N$ . Contrary to the situation in  $\text{LaTiO}_{3+\delta}$ , the Néel temperature in these cuprates is found to be proportional to the ordered moment [148]. Long-range AF order in  $\text{YBa}_2\text{Cu}_3\text{O}_{6+\delta}$  and  $\text{La}_2\text{CuO}_{4+\delta}$  cannot develop above a critical hole concentration of  $\sim 0.02$  holes/Cu. The AF ordered moment on Mn in  $\text{LaMnO}_3$  (AF type-*A* structure,  $3.49\mu_B$  with  $T_N = 140$  K) is, like for the titanates and cuprates, strongly reduced upon hole doping. Ordered moments of  $2.52\mu_B$  and  $0.25\mu_B$  are reported for  $\text{LaMnO}_{3.025}$  and  $\text{LaMnO}_{3.07}$ , respectively [152]. In  $\text{LaMnO}_{3+\delta}$ , filling the Mn–O band leads to a decrease in AF moment and a gradual formation of ferromagnetic order, which makes it difficult to make a statement concerning the doping dependence of the Néel temperature. Note the similarity in hole doping above which AF order in  $\text{LaTiO}_{3+\delta}$  and  $\text{LaMnO}_{3+\delta}$  is suppressed. In the ionic picture, this critical doping of  $\sim 0.14$  to  $0.16$  holes/site corresponds to  $M^{4+}/M^{3+} \sim 1/6$ , i.e., every spin ( $M^{3+}$ ) has on average about one hole ( $M^{4+}$ ) as its nearest neighbour. This is consistent with the model proposed by Aharony *et al.* [160], that the effect of hole doping is not to dilute the spin

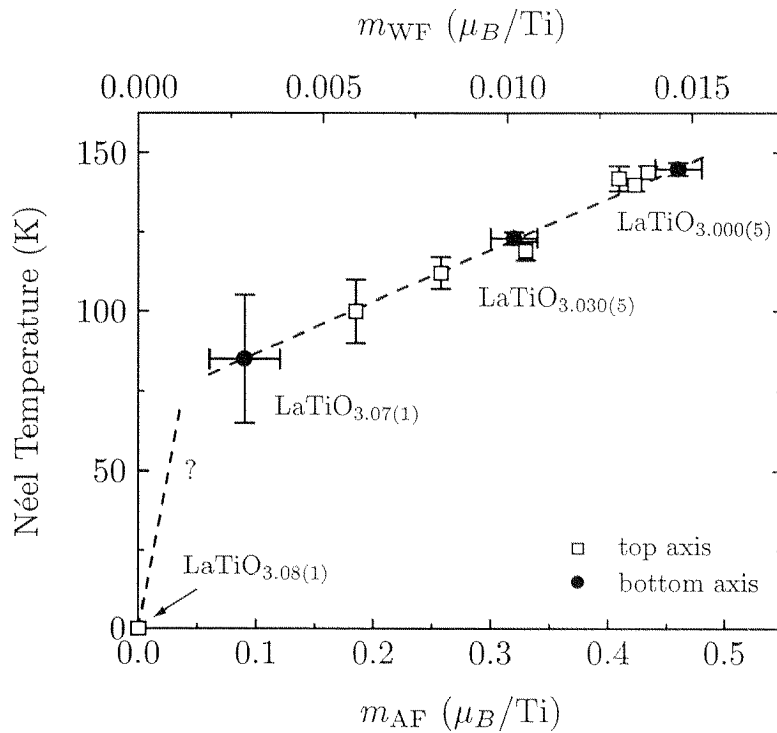


Figure 7.3: Néel temperature  $T_N$  versus the AF ordered moment  $m_{AF}$  on Ti (bottom axis) for  $LaTiO_{3.000(5)}$ ,  $LaTiO_{3.030(5)}$ , and  $LaTiO_{3.07(1)}$ . The weak-ferromagnetic moment  $m_{WF}$  for an additional series of crystals is included (top axis). The  $m_{WF}$  (top axis) is scaled to  $m_{AF}$  for  $LaTiO_{3.000(5)}$ . The dashed lines are guides to the eye.

system, but to introduce frustration. The holes in rare-earth oxides reside primarily on oxygen atoms. The exchange interaction between the hole on the oxygen and each of its two nearest-neighbouring  $M$  ( $M$  is Ti, Mn, or Cu) holes requires that the  $M$  spins be parallel. Frustration occurs because the  $M$ -O- $M$  superexchange interaction is antiferromagnetic. If the O- $M$  exchange is large enough, AF order will be disrupted.

How does this compare with the quasi-one-dimensional cuprates discussed previously? This chapter stresses this once again how remarkable the observed 3D magnetic order in the highly doped quasi-one-dimensional cuprates  $\text{Sr}_{0.73}\text{CuO}_2$  and  $\text{Ca}_{0.83}\text{CuO}_2$  is [34]. We saw from the discussion of  $\text{LaTiO}_3$  that this titanate is to a certain extent a “usual” 3D magnetic system, exhibiting, consequently, magnetic ordering at low temperatures [35]. The crystal symmetry is low enough to contribute to a magnetic anisotropy by allowing an antisymmetric exchange to occur. The observed weak-ferromagnetic moment is due to this Dzyaloshinski–Moriya interaction. The  $\text{LaTiO}_{3+\delta}$  spin system cannot sustain a spontaneous magnetisation when the hole doping exceeds about 0.16 holes/site ( $\delta \sim 0.08$ ). Similar bounds for the doping level are found in quasi-2D spin systems (compare this with the 2D Cu–O layers present in high- $T_c$  cuprates, which show magnetic order up to  $\sim 0.04$ – $0.125$  holes/Cu [75]). This indicates a new origin of the physical mechanism responsible for stabilising the spins of localised electrons into an ordered array in highly doped  $\text{Sr}_{0.73}\text{CuO}_2$  (0.5–0.6 holes/Cu) and  $\text{Ca}_{0.83}\text{CuO}_2$  (0.3 holes/Cu). Although microscopically not yet fully understood, preliminary ideas were presented in Section 6.4.

## 7.4 Magnetisation of $\text{LaTiO}_{3.07(1)}$

The magnetisation curves  $m(H)$  of  $\text{LaTiO}_{3+\delta}$  crystals were measured to study the behaviour of the weak-ferromagnetic component in the ordered moment. The crystals have been cooled to  $T < T_N$  in a  $\mu$ -metal shielded environment to ensure true zero-field cooling prior to the measurement. Whereas  $\text{LaTiO}_3$  shows the typical  $m(H)$  behaviour of a weak ferromagnet, a peculiar magnetisation behaviour is found for hole-doped samples on the verge of the Mott–Hubbard transition boundary. Figure 7.4 shows the magnetisation curves  $m(H)$  of  $\text{LaTiO}_{3.07(1)}$  for three different temperatures. Pronounced steps in the magnetisation curve upon reaching the saturation moment are observed. These steps are basically equally spaced in the applied field. With increasing temperature, the separation between the steps decreases. It is interesting to note that the magnetisation curve  $m(H)$  at  $T = 5$  K of the related Mott–Hubbard insulator  $\text{PrTiO}_3$  was also shown to have a large hys-

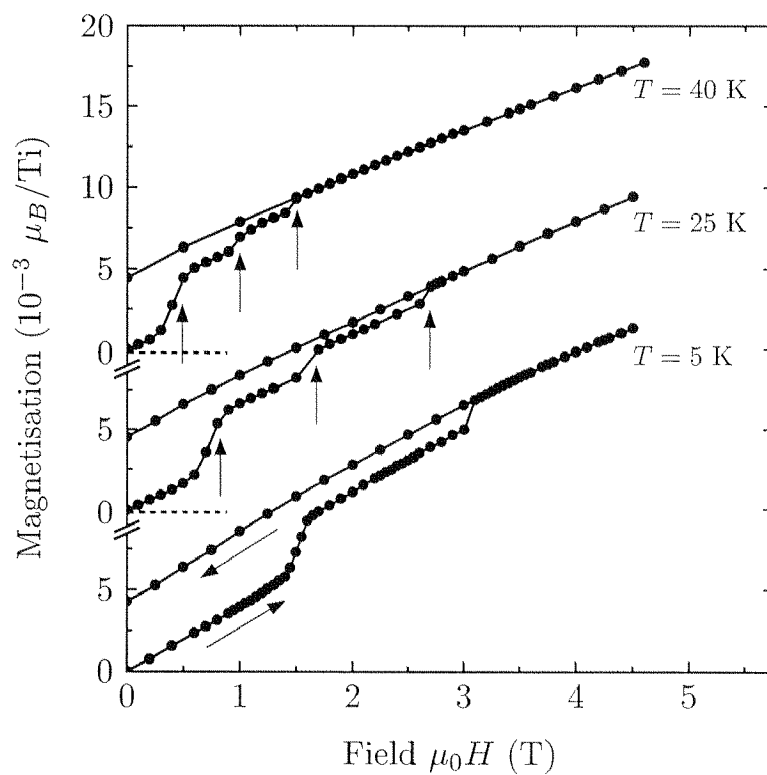


Figure 7.4: Magnetisation of  $\text{LaTiO}_{3.07(1)}$  versus applied field  $m(H)$  for temperatures indicated. The  $m(H)$  curves for  $T = 25$  K and  $T = 40$  K are offset for clarity. The sample is cooled in a  $\mu$ -metal shielded environment to ensure zero-field cooling. The series of steps in  $m(H)$  are indicated by an arrow.

teresis, with one clear step at  $\mu_0 H \sim 3.5$  T [147]. One might speculate that an applied field is able to switch one twin domain into another with a more favourable ferromagnetic direction, generating steps in the magnetisation curve. This could also explain qualitatively its temperature dependence as being a balance between the thermal energy and the energy introduced by the field. It remains surprising, however, that the steps are regularly spaced in the applied field. Further information on the field dependence of the ferromagnetic component in the ordered state could be obtained by polarised neutron scattering experiments.

In summary, neutron diffraction and magnetic susceptibility of single crystals of the doped Mott–Hubbard insulator  $\text{LaTiO}_{3+\delta}$  are presented. The  $\text{Ti}^{3+}$  moment,  $0.46(2)\mu_B$  in  $\text{LaTiO}_{3.000(5)}$ , is very sensitive to the departure from the exact stoichiometry, i.e., it is shown to decrease rapidly with increasing nonstoichiometric oxygen  $0 < \delta \lesssim 0.08$  [35]. The hole doping of about 0.16 holes/site ( $\delta \sim 0.08$ ) is the upper boundary for long-range 3D magnetic order to occur in the  $\text{LaTiO}_{3+\delta}$  spin system. Near the insulator–to–metal transition, i.e., in  $\text{LaTiO}_{3.07(1)}$ , the weak-ferromagnetic saturation moment is reached via a series of well-defined steps in the magnetisation curve.

# Chapter 8

## Conclusions

In this thesis, I have presented various aspects of magnetism in the quasi-one-dimensional quantum magnets  $\text{Sr}_{0.73}\text{CuO}_2$  and  $\text{Ca}_{0.83}\text{CuO}_2$  and in the Mott–Hubbard system  $\text{LaTiO}_3$ . A series of complimentary experimental techniques were successfully applied to reveal the magnetic behaviour of these strongly correlated transition metal oxides.

The first aim of this investigation was to study quantum magnetism in low-dimensional spin systems, in particular quasi-one-dimensional compounds. This field, initiated by the famous conjecture of Haldane,<sup>1</sup> has emerged as a central problem in condensed-matter physics, especially since the discovery of high- $T_c$  superconductivity in 1986. A reason for the current work was to contribute to a detailed understanding of magnetism in 1D. This might generate a more comprehensive picture of the properties of 2D systems, which are also dominated by quantum fluctuations. Moreover, the previous exciting discoveries in these low-dimensional materials warranted the assumption that new surprising phenomena might be discovered by undertaking such studies.

The major part of this manuscript concentrated on the two nearly isomorphous hole-doped cuprates  $\text{Sr}_{0.73}\text{CuO}_2$  and  $\text{Ca}_{0.83}\text{CuO}_2$ . These two quasi-1D cuprates offered the unique opportunity to study the physical properties of highly hole-doped  $\text{CuO}_2$  chains. At the end of the manuscript a brief excursion was taken to the strongly correlated  $\text{LaTiO}_3$  system (distorted Perovskite).

The complexity of all these magnetic oxides required many different ex-

---

<sup>1</sup>The basic properties of the  $S = 1/2$  chain are shared only by chains with half-odd-integer  $S$ , and integer  $S$  chains behave fundamentally differently.



perimental techniques to resolve their magnetic properties. In the course of this thesis SQUID measurements, magnetic torque experiments, specific heat measurements, neutron diffraction, and inelastic neutron scattering techniques were applied for this purpose.

Concerning the quasi-1D cuprate  $\text{Sr}_{0.73}\text{CuO}_2$ , we examined the static magnetic susceptibility. One might expect that for this highly hole-doped cuprate the propensity of spins to order is greatly reduced due to the huge dilution of the spin system ( $\sim 0.6$  nonmagnetic holes per Cu). Thus the discovery of antiferromagnetic (AF) order at  $T \sim 10$  K discussed in Chapter 3 was a surprise; in fact, there are no other cuprates known that exhibit magnetic ordering at such a doping level. At higher temperatures we find evidence of singlet pairing of spins in the  $\text{CuO}_2$  chains. The manifestation of this behaviour reflected a dominant 1D behaviour, with a relatively weak interchain coupling. (Obviously, nature can provide only approximations of the ideal 1D magnetic structure.) The residual interchain coupling in turn leads to the 3D ordering observed at sufficiently low temperatures. The conclusion that the chains are dimerised was at that point, however, controversial because the typical precipitous drop in susceptibility at low temperatures for a system with a spin gap was masked by a large Curie-type term.

Turning next to  $\text{Ca}_{0.83}\text{CuO}_2$  ( $\sim 0.34$  holes per Cu), we have witnessed in Chapter 4 based on susceptibility and torque measurements that this compound also exhibits AF order at  $T \sim 12$  K. Contrary to the situation in  $\text{Sr}_{0.73}\text{CuO}_2$ , however, no spin canting resulting in a weak-ferromagnetic moment is found in  $\text{Ca}_{0.83}\text{CuO}_2$ . The torque analysis demonstrated the existence of an easy axis in this ordered state. Above  $T \sim 12$  K, the static susceptibility can be described with a model of a 3D assembly of loosely coupled alternating Heisenberg chains. Also for  $\text{Ca}_{0.83}\text{CuO}_2$ , susceptibility measurements gave some indication of dimerisation of the spin chains, similar to  $\text{Sr}_{0.73}\text{CuO}_2$ .

The initial evidence in Chapters 3 and 4 of an AF ordered phase below  $T \sim 10$  K has been consolidated in Chapter 5. Specific heat experiments, neutron powder diffraction, and torque measurements provided additional insight into the magnetically ordered phase below  $T \sim 10$  K. All these techniques produced at the same result: that the AF ordered state of  $\text{Ca}_{0.83}\text{CuO}_2$  and  $\text{Sr}_{0.73}\text{CuO}_2$  at  $T \sim 10$  K is of long-range 3D character.

This evokes an apparent paradox. The susceptibility of  $\text{Sr}_{0.73}\text{CuO}_2$  and  $\text{Ca}_{0.83}\text{CuO}_2$  was interpreted in terms of coupled dimers, which implies a nonmagnetic ground state. We have, as the reader will agree, established in Chapter 5 that  $\text{Ca}_{0.83}\text{CuO}_2$  and  $\text{Sr}_{0.73}\text{CuO}_2$  exhibit long-range 3D order. Intuition might lead us to expect that those two ground states are exclusive.

Therefore, a possible conclusion could have been that the interpretation of the susceptibility of  $\text{Sr}_{0.73}\text{CuO}_2$  was indeed hampered to too great an extent by the low-temperature Curie term and that an attribution of the observed behaviour to any type of dimer model would be fallacious. This is not the case, however.

The key to this problem lay in the study of the magnetic excitations of this compound, discussed in Chapter 6. The quantum spin dynamics of polycrystalline  $\text{Sr}_{0.73}\text{CuO}_2$  was investigated by inelastic neutron scattering. An excitation mode with two distinct peaks at  $E = 10$  and  $17.5$  meV and additional magnetic scattering up to  $E \sim 25$  meV was observed in the neutron spectrum. I asserted that this magnetic response arises from excitations of dimerised spin chains. The two peaks were argued to be due to the dispersive magnon branch with a spin excitation gap of  $\Delta \sim 10$  meV. The scattering near  $E = 22.5$  meV is consistent with an excitation continuum. It was very gratifying to observe how close the agreement was between the predicted value (based on susceptibility measurements) and neutron scattering data. Further support of the dimer model was found in the wave-vector dependence of the integrated intensity, i.e., that dimers are formed between next-nearest-neighbour Cu ions separated by a nonmagnetic hole. Our measurements indicate that the spin dimer phase coexists with long-range AF order in  $\text{Sr}_{0.73}\text{CuO}_2$  below  $T \sim 10$  K. I wish to emphasise the importance of this finding as it shows that such coexistence is not restricted to the doped spin-Peierls system  $\text{CuGeO}_3$ .

In Chapter 7, neutron diffraction and magnetic susceptibility of single crystals of the doped Mott-Hubbard insulator  $\text{LaTiO}_{3+\delta}$  were presented.  $\text{LaTiO}_3$  is to a certain extent an “ordinary” 3D magnetic system with Perovskite structure. Consequently, it exhibits magnetic ordering at low temperatures. The  $\text{Ti}^{3+}$  moment,  $0.46(2)\mu_B$  in  $\text{LaTiO}_{3.000(5)}$ , was shown to decrease rapidly with increasing nonstoichiometric oxygen  $0 < \delta \lesssim 0.08$ . The hole doping of about 0.16 holes/site ( $\delta \sim 0.08$ ) is the upper boundary for long-range 3D magnetic order to occur in the  $\text{LaTiO}_{3+\delta}$  spin system. If we compare this doping level to that of the previously discussed quasi-one-dimensional  $\text{Sr}_{0.73}\text{CuO}_2$  (0.54 holes/site) and  $\text{Ca}_{0.83}\text{CuO}_2$  (0.34 holes/site), we see once more how remarkable the observed 3D magnetic order in those two compounds is.

Although there certainly remains a number of problems to be solved, a considerable progress in understanding the physics of the low-dimensional cuprates  $\text{Sr}_{0.73}\text{CuO}_2$  and  $\text{Ca}_{0.83}\text{CuO}_2$  has been made. Undoubtedly, these two systems provide valuable new information for our understanding of low-dimensional magnetic systems and the various possibilities they offer for

novel quantum ground states. Their exciting magnetic behaviour made these compounds fascinating to investigate, and I hope this manuscript was able to express this sense of excitement. I would like to conclude with a general statement that doped transition metal oxides, particularly in low dimensions, present fascinating and rich phenomena to be studied for decades and to come.

# Bibliography

- [1] J. G. Bednorz and K. A. Müller, *Z. Phys. B* **64**, 189 (1986).
- [2] E. Manousakis, *Rev. Mod. Phys.* **63**, 1 (1991).
- [3] H. Bethe, *Z. Phys.* **71**, 205 (1931).
- [4] P. W. Anderson, *Phys. Rev.* **86**, 694 (1952).
- [5] N. D. Mernin and H. Wagner, *Phys. Rev. Lett.* **17**, 1133 (1966).
- [6] A. Luther and I. Peschel, *Phys. Rev. B* **9**, 2911 (1974).
- [7] R. E. Peierls, *Quantum Theory of Solids* (Clarendon, Oxford, 1955).
- [8] M. C. Cross and D. S. Fisher, *Phys. Rev. B* **19**, 402 (1979).
- [9] For a review of the spin–Peierls compound  $\text{CuGeO}_3$ , see, for example, J. P. Boucher and L. P. Regnault, *J. Phys. I* **6**, 1939 (1996).
- [10] M. Isobe and Y. Ueda, *J. Phys. Soc. Jpn.* **65**, 1178 (1996).
- [11] F. D. M. Haldane, *Phys. Rev. Lett.* **50**, 1153 (1983).
- [12] J. P. Renard, M. Verdaguer, L. P. Regnault, W. A. C. Erkelens, J. Rossat-Mignod, and W. G. Stirling, *Europhys. Lett.* **3**, 945 (1987).
- [13] W. J. L. Buyers, R. M. Morra, R. L. Armstrong, M. J. Hogan, P. Gerlach, and K. Hirakawa, *Phys. Rev. Lett.* **56**, 371 (1986).
- [14] J. F. DiTusa, S-W. Cheong, J.-H. Park, G. Aeppli, C. Broholm, and C. T. Chen, *Phys. Rev. Lett.* **73**, 1857 (1994).
- [15] For a review of ladder materials, see, for example, E. Dagotto and T. M. Rice, *Science* **271**, 618 (1996).
- [16] Z. Hiroi and M. Takano, *Nature (London)* **377**, 41 (1995).

- [17] F. Zhang and T. M. Rice, *Phys. Rev. B* **37**, 3759 (1988).
- [18] P. Wachter and L. Degiorgi, *Solid State Commun.* **66**, 211 (1988).
- [19] T. M. Rice, S. Gopalan, and M. Sigrist, *Europhys. Lett.* **23**, 445 (1993).
- [20] M. Uehara, T. Nagata, J. Akimitsu, H. Takahashi, N. Môri, and K. Kinoshita, *J. Phys. Soc. Jpn.* **65**, 2764 (1996).
- [21] T. Nagata, M. Uehara, J. Goto, J. Akimitsu, N. Motoyama, H. Eisaki, S. Uchida, H. Takahashi, T. Nakanishi, and N. Môri, *Phys. Rev. Lett.* **81**, 1090 (1998).
- [22] For a recent comparison of doped  $\text{CuGeO}_3$ , see, for example, B. Grenier, J.-P. Renard, P. Veillet, C. Paulsen, G. Dhahlenne, and A. Revcolevschi, *Phys. Rev. B* **58**, 8202 (1998), and references therein.
- [23] H. Fukujama, T. Tanimoto, and M. Saito, *J. Phys. Soc. Jpn.* **65**, 1182 (1996).
- [24] M. Fabrizio and R. Mélin, *Phys. Rev. Lett.* **78**, 3382 (1997).
- [25] G. B. Martins, M. Laukamp, J. Riera, and E. Dagotto, *Phys. Rev. Lett.* **78**, 3563 (1997).
- [26] C. Pépin and P. A. Lee, *Phys. Rev. Lett.* **81**, 2779 (1998).
- [27] J. Karpinski, H. Schwer, G. I. Meijer, K. Conder, E. M. Kopnin, and C. Rossel, *Physica C* **274**, 99 (1997).
- [28] C. Rossel, P. Bauer, D. Zech, J. Hofer, M. Willemin, and H. Keller, *J. Appl. Phys.* **79**, 8166 (1996).
- [29] M. Willemin, C. Rossel, J. Brugger, M. H. Despont, H. Rothuizen, P. Vettiger, J. Hofer, and H. Keller, *J. Appl. Phys.* **83**, 1163 (1998).
- [30] C. Rossel, M. Willemin, A. Gasser, H. Rothuizen, G. I. Meijer, and H. Keller, *Rev. Sci. Instrum.* **69**, 3199 (1998).
- [31] G. I. Meijer, *Science* **281**, 1571a (1998).
- [32] A. Shengelaya, G. I. Meijer, J. Karpinski, G.-M. Zhao, H. Schwer, E. M. Kopnin, C. Rossel, and H. Keller, *Phys. Rev. Lett.* **80**, 3626 (1998).
- [33] G. I. Meijer, C. Rossel, E. M. Kopnin, M. Willemin, J. Karpinski, H. Schwer, K. Conder, and P. Wachter, *Europhys. Lett.* **42**, 339 (1998).

- [34] G. I. Meijer, C. Rossel, W. Henggeler, L. Keller, F. Fauth, J. Karpinski, H. Schwer, E. M. Kopnin, P. Wachter, R. C. Black, and J. Diederichs, *Phys. Rev. B* **58**, 14 452 (1998).
- [35] G. I. Meijer, W. Henggeler, J. Brown, O.-S. Becker, J. G. Bednorz, C. Rossel, and P. Wachter, *Phys. Rev. B* **59**, 11 832 (1999).
- [36] G. I. Meijer, R. S. Eccleston, H. Mutka, C. Rossel, J. Karpinski, S. Kazakov, and P. Wachter, submitted for publication in *Phys. Rev. B*.
- [37] M. Willemin, Ph.D. thesis, University of Zurich, 1999, and references therein.
- [38] R. F. Penoyer, *Rev. Sci. Instrum.* **30**, 711 (1959).
- [39] G. L. Squires, *Introduction to the Theory of Thermal Neutron Scattering* (Cambridge University Press, Cambridge, 1978).
- [40] S. W. Lovesey, *Theory of Neutron Scattering from Condensed Matter* (Clarendon Press, Oxford, 1984).
- [41] [http://www1.psi.ch/www\\_sinq\\_hn/SINQ/instr/DMC.html](http://www1.psi.ch/www_sinq_hn/SINQ/instr/DMC.html)
- [42] <http://www.ill.fr/YellowBook/D1A>
- [43] <http://www.ill.fr/YellowBook/D1B>
- [44] <http://www.isis.rl.ac.uk/excitations/HET/HET.HTM>
- [45] <http://www.ill.fr/YellowBook/IN5>
- [46] <http://www.ill.fr/YellowBook/D15>
- [47] M. Hase, I. Terasaki, and K. Uchinokura, *Phys. Rev. Lett.* **70**, 3651 (1993).
- [48] M. Azuma, Z. Hiroi, M. Takano, K. Ishida, and Y. Kitaoka, *Phys. Rev. Lett.* **73**, 3463 (1994).
- [49] E. Dagotto, J. Riera, and D. Scalapino, *Phys. Rev. B* **45**, 5744 (1992).
- [50] M. Matsuda and K. Katsumata, *Phys. Rev. B* **53**, 12 201 (1996).
- [51] S. A. Carter, B. Batlogg, R. J. Cava, J. J. Krajewski, W. F. Peck Jr., and T. M. Rice, *Phys. Rev. Lett.* **77**, 1378 (1996).
- [52] E. M. McCarron, M. A. Subramanian, J. C. Calabrese, and R. L. Harlow, *Mater. Res. Bull.* **23**, 1355 (1988).

- [53] T. Siegrist, L. F. Schneemeyer, S. A. Sunshine, J. V. Waszczak, and R. S. Roth, *Mater. Res. Bull.* **23**, 1429 (1988).
- [54] R. S. Eccleston, M. Azuma, and M. Takano, *Phys. Rev. B* **53**, 14 721 (1996).
- [55] N. Motoyama, T. Osafune, T. Kakeshita, H. Eisaki, and S. Uchida, *Phys. Rev. B* **55**, 3386 (1997).
- [56] For a review of high-pressure syntheses, see, for example, J. Karpinski *et al.*, in *Recent Developments in High Temperature Superconductivity*, edited by J. Klamut *et al.*, Lecture Notes in Physics, Vol. 475 (Springer, Berlin, 1996), p. 83.
- [57] K. Conder, S. Rusiecki, and E. Kaldis, *Mat. Res. Bull.* **24**, 581 (1989).
- [58] K. M. Kojima, Y. Fudamoto, M. Larkin, G. M. Luke, J. Merrin, B. Nachumi, Y. J. Uemura, M. Hase, Y. Sasago, K. Uchinokura, Y. Ajiro, A. Revcolevschi, and J.-P. Renard, *Phys. Rev. Lett.* **79**, 503 (1997).
- [59] T. Thio, T. R. Thurston, N. W. Preyer, P. J. Picone, and M. A. Kastner, *Phys. Rev. B* **38**, 905 (1988).
- [60] J. D. Thompson, S-W. Cheong, S. E. Brown, Z. Fisk, S. B. Oseroff, M. Tovar, D. C. Vier, and S. Schultz, *Phys. Rev. B* **39**, 6660 (1989).
- [61] I. Dzyaloshinski, *J. Phys. Chem. Solids* **4**, 241 (1958).
- [62] T. Moriya, *Phys. Rev.* **120**, 91 (1960).
- [63] Z. Hiroi, S. Amelinckx, G. Van Tendeloo, and N. Kobayashi, *Phys. Rev. B* **54**, 15 849 (1996).
- [64] J. C. Bonner and M. E. Fisher, *Phys. Rev.* **135**, A640 (1964).
- [65] L. N. Bulaevskiĭ, *JETP* **44**, 1008 (1963); *Soviet Phys. JETP* **17**, 684 (1963).
- [66] J. C. Bonner, H. W. J. Blöte, J. W. Bray, and I. S. Jacobs, *J. Appl. Phys.* **50**, 1810 (1979).
- [67] L. N. Bulaevskiĭ, *JETP* **43**, 968 (1962); *Soviet Phys. JETP* **16**, 685 (1963).
- [68] S. Eggert, I. Affleck, and M. Takahashi, *Phys. Rev. Lett.* **73**, 332 (1994).

- [69] B. Frischmuth, B. Ammon, and M. Troyer, *Phys. Rev. B* **54**, 3714 (1996).
- [70] A. Abragam and B. Bleaney, *Electron Paramagnetic Resonance of Transition Ions* (Clarendon, Oxford, 1970).
- [71] W. E. Estes, D. P. Gavel, W. E. Hatfield, and D. J. Godjson, *Inorg. Chem.* **17**, 1415 (1978).
- [72] J. W. Hall *et al.*, *Inorg. Chem.* **20**, 1033 (1981).
- [73] T. Barnes and J. Riera, *Phys. Rev. B* **50**, 6817 (1994).
- [74] S. Moukouri and L. G. Caron, *Phys. Rev. Lett.* **77**, 4640 (1996).
- [75] J. M. Tranquada, B. J. Sternlieb, J. D. Axe, Y. Nakamura, and S. Uchida, *Nature (London)* **375**, 561 (1995).
- [76] A. B. Harris, *Phys. Rev. B* **7**, 3166 (1973).
- [77] T. Siegrist, R. S. Roth, C. J. Rawn, and J. J. Ritter, *Chem. Mat.* **2**, 192 (1990).
- [78] O. Milat, G. van Tenderloo, S. Amelinckx, T. G. N. Babu, and C. Greaves, *J. Solid State Chem.* **97**, 405 (1992).
- [79] J. G. Thompson, J. D. Fitz Gerald, R. L. Withers, P. J. Barlow, and J. S. Anderson, *Mat. Res. Bull.* **24**, 505 (1989).
- [80] J. Dolinšek, D. Arčon, P. Cevc, O. Milat, M. Miljak, and I. Aviani, *Phys. Rev. B* **57**, 7798 (1998).
- [81] H. J. Schulz, *Phys. Rev. Lett.* **77**, 2790 (1996).
- [82] F. Barriquand and G. A. Sawatzky, *Phys. Rev. B* **50**, 16 649 (1994).
- [83] Y. Mizuno, T. Tohyama, S. Maekawa, T. Osafune, N. Motoyama, H. Eisaki, and S. Uchida, *Phys. Rev. B* **57**, 5326 (1998).
- [84] R. Weht and W. E. Pickett, *Phys. Rev. Lett.* **81**, 2502 (1998).
- [85] J. Riera and A. Dobry, *Phys. Rev. B* **51**, 16 098 (1995).
- [86] G. Castilla, S. Chakravarty, and V. J. Emery, *Phys. Rev. Lett.* **75**, 1823 (1995).
- [87] W. Geertsma and D. Khomskii, *Phys. Rev. B* **54**, 3011 (1996).



- [88] J. B. Goodenough, *Phys. Rev.* **100**, 564 (1955).
- [89] J. Kanamori, *J. Phys. Chem. Solids* **10**, 87 (1959).
- [90] P. W. Anderson, *Solid State Phys.* **14**, 99 (1963).
- [91] Z. R. Wang, D. C. Johnston, L. L. Miller, and D. Vaknin, *Phys. Rev. B* **52**, 7384 (1995).
- [92] M. Matsuda, K. Katsumata, T. Yokoo, S. M. Shapiro, and G. Shirane, *Phys. Rev. B* **54**, 15 626 (1996).
- [93] D. Coffey, T. M. Rice, and F. C. Zhang, *Phys. Rev. B* **44**, 10 112 (1991), and references therein.
- [94] O. Entin-Wohlman, A. B. Harris, and A. Aharony, *Phys. Rev. B* **53**, 11 661 (1996).
- [95] J. P. Pouget, L.-P. Regnault, M. Ain, B. Hennion, J.-P. Renard, P. Veillet, G. Dhahlenne, and A. Revcolevschi, *Phys. Rev. Lett.* **72**, 4037 (1994).
- [96] K. Hirota, D. E. Cox, J. E. Lorenzo, G. Shirane, J. M. Tranquada, M. Hase, and K. Uchinokura, *Phys. Rev. Lett.* **73**, 736 (1994).
- [97] M. C. Martin, G. Shirane, Y. Fujii, M. Nishi, O. Fujita, J. Akimitsu, M. Hase, and K. Uchinokura, *Phys. Rev. B* **53**, 14 713 (1996).
- [98] M. Arai, M. Fujita, M. Motokawa, J. Akimitsu, and S. M. Bennington, *Phys. Rev. Lett.* **77**, 3649 (1996).
- [99] J.-P. Renard, K. Le Dang, P. Veillet, G. Dhahlenne, A. Revcolevschi, and L.-P. Regnault, *Europhys. Lett.* **30**, 475 (1995).
- [100] S. B. Oseroff, S-W. Cheong, B. Aktas, M. F. Hundley, Z. Fisk, and L. W. Rupp Jr., *Phys. Rev. Lett.* **74**, 1450 (1995).
- [101] L. P. Regnault, J.-P. Renard, G. Dhahlenne, and A. Revcolevschi, *Europhys. Lett.* **32**, 579 (1995).
- [102] M. Hase, K. Uchinokura, R. J. Birgeneau, K. Hirota, and G. Shirane, *J. Phys. Soc. Jpn.* **65**, 1392 (1996).
- [103] M. Matsuda, K. Katsumata, H. Eisaki, N. Motoyama, S. Uchida, S. M. Shapiro, and G. Shirane, *Phys. Rev. B* **54**, 12 199 (1996).

- [104] R. S. Eccleston, M. Uehara, J. Akimitsu, H. Eisaki, N. Motoyama, and S. Uchida, *Phys. Rev. Lett.* **81**, 1702 (1998).
- [105] M. Matsuda, T. Yoshihama, K. Kakurai, and G. Shirane, *Phys. Rev. B* **59**, 1060 (1999).
- [106] L. P. Regnault, J. P. Boucher, H. Moudden, J. E. Lorenzo, A. Hiess, U. Ammerahl, G. Dhalenne, and A. Revcolevschi, *Phys. Rev. B* **59**, 1055 (1999).
- [107] M. Matsuda, K. M. Kojima, Y. J. Uemura, J. L. Zarestky, K. Nakajima, K. Kakurai, T. Yokoo, S. M. Shapiro, and G. Shirane, *Phys. Rev. B* **57**, 11 467 (1998).
- [108] R. C. Black and J. Diederichs, Quantum Design, San Diego, California 92121.
- [109] K. Takeda, S. Matsukawa, and T. Haseda, *J. Phys. Soc. Jpn.* **30**, 1330 (1971).
- [110] L. J. de Jongh and A. R. Miedema, *Adv. Phys.* **23**, 1 (1974).
- [111] N. W. Ashcroft and N. D. Mermin, *Solid State Physics* (Saunders Company, 1976), p. 459.
- [112] D. E. Cox, T. Iglesias, K. Hirota, G. Shirane, M. Matsuda, N. Motoyama, H. Eisaki, and S. Uchida, *Phys. Rev. B* **57**, 10 750 (1998).
- [113] J. D. Reger and A. P. Young, *Phys. Rev. B* **37**, 5978 (1988).
- [114] S. Liang, *Phys. Rev. B* **42**, 6555 (1990), and references therein.
- [115] T. Oguch, *Phys. Rev.* **133**, A1098 (1964).
- [116] K. M. Kojima, Y. Fudamoto, M. Larkin, G. M. Luke, J. Merrin, B. Nachumi, Y. J. Uemura, N. Motoyama, H. Eisaki, S. Uchida, K. Yamada, Y. Endoh, S. Hosoya, B. J. Sternlieb, and G. Shirane, *Phys. Rev. Lett.* **78**, 1787 (1997).
- [117] G. S. Uhrig and H. J. Schulz, *Phys. Rev. B* **54**, 9624 (1996); **58**, 2900(E) (1998).
- [118] T. Barnes, J. Riera, and D. A. Tennant, *Phys. Rev. B* **59**, 11 384 (1999).
- [119] C. K. Majumdar and D. K. Ghosh, *J. Math. Phys.* **10**, 1388 (1969).

- [120] A. Luther and I. Peschel, Phys. Rev. B **12**, 3908 (1975).
- [121] F. D. M. Haldane, Phys. Rev. Lett. **45**, 1358 (1980).
- [122] L. D. Faddeev and L. A. Takhtajan, Phys. Lett. A **85**, 375 (1981).
- [123] B. S. Shastry and B. Sutherland, Phys. Rev. Lett. **47**, 964 (1981).
- [124] J. des Cloizeaux and J. J. Pearson, Phys. Rev. **128**, 2131 (1962).
- [125] G. Müller, H. Beck, and J. C. Bonner, Phys. Rev. Lett. **43**, 75 (1979).
- [126] See, for example, D. A. Tennant, R. A. Cowley, S. E. Nagler, and A. M. Tsvelik, Phys. Rev. B **52**, 13 368 (1995).
- [127] W. Duffy, Jr., and K. P. Barr, Phys. Rev. **165**, 647 (1968).
- [128] J. C. Bonner and H. W. J. Blöte, Phys. Rev. B **25**, 6959 (1982).
- [129] G. Bouzerar, A. P. Kampf, and G. I. Japaridze, Phys. Rev. B **58**, 3117 (1998).
- [130] A. H. Bougourzi, M. Karbach, and G. Müller, Phys. Rev. B **57**, 11 429 (1998).
- [131] A. Furrer and H. U. Güdel, Phys. Rev. Lett. **39**, 657 (1977).
- [132] H. Güdel, A. Stebler, and A. Furrer, Inorg. Chem. **18**, 1021 (1979).
- [133] F. D. M. Haldane, Phys. Rev. B **25**, 4925 (1982).
- [134] S. R. White and I. Affleck, Phys. Rev. B **54**, 9862 (1996).
- [135] This dimer–dimer separation was found in the  $\text{CuO}_2$  chains of  $\text{Sr}_{14}\text{Cu}_{24}\text{O}_{41}$  (Refs. [104, 92, 106]), which has a structure and doping similar to  $\text{Sr}_{0.73}\text{CuO}_2$ .
- [136] A. Shengelaya (private communication).
- [137] H. Mutka, C. Payen, P. Molinie, J. L. Soubeyroux, P. Colombet, and A. D. Taylor, Phys. Rev. Lett. **67**, 497 (1991), and references cited therein.
- [138] J. Zaanen, G. A. Sawatzky, and J. W. Allen, Phys. Rev. Lett. **55**, 418 (1985).

- [139] The variation of the gap in  $\text{LaMO}_3$  has been studied for all  $3d$  transition elements  $M$  by T. Arima, Y. Tokura, and J. B. Torrance, *Phys. Rev. B* **48**, 17 006 (1993).
- [140] Y. Okimoto, T. Katsufuji, Y. Okada, T. Arima, and Y. Tokura, *Phys. Rev. B* **51**, 9581 (1995).
- [141] Y. Tokura, T. Taguchi, Y. Okada, Y. Fujishima, T. Arima, K. Kumagai, and Y. Iye, *Phys. Rev. Lett.* **70**, 2126 (1993).
- [142] T. Katsufuji and Y. Tokura, *Phys. Rev. B* **50**, 2704 (1994).
- [143] F. Lichtenberg, T. Williams, A. Reller, D. Widmer, and J. G. Bednorz, *Z. Phys. B* **84**, 369 (1991).
- [144] Y. Okada, T. Arima, Y. Tokura, C. Murayama, and N. Mōri, *Phys. Rev. B* **48**, 9677 (1993).
- [145] D. A. Crandles, T. Timusk, J. D. Garrett, and J. E. Greedan, *Phys. Rev. B* **49**, 16 207 (1994).
- [146] T. Katsufuji, Y. Taguchi, and Y. Tokura, *Phys. Rev. B* **56**, 10 145 (1997).
- [147] T. Katsufuji, T. Okimoto, and Y. Tokura, *Phys. Rev. Lett.* **75**, 3497 (1995).
- [148] D. C. Johnston, *J. Magn. Magn. Mater.* **100**, 218 (1991), and references therein.
- [149] M. A. Karstner, R. J. Birgeneau, G. Shirane, and Y. Endoy, *Rev. Mod. Phys.* **70**, 897 (1998), and references therein.
- [150] R. von Helmolt, J. Wecker, B. Holzapfel, L. Schultz, and K. Samwer, *Phys. Rev. Lett.* **71**, 2331 (1993).
- [151] A. Urushibara, Y. Moritomo, T. Arima, A. Asamitsu, G. Kido, and Y. Tokura, *Phys. Rev. B* **51**, 14 103 (1995).
- [152] C. Ritter, M. R. Ibarra, J. M. De Teresa, P. A. Algarabel, C. Marquina, J. Blasco, J. García, S. Oseroff, and S.-W. Cheong, *Phys. Rev. B* **56**, 8902 (1997).
- [153] M. Imada, A. Fujimori, and Y. Tokura, *Rev. Mod. Phys.* **70**, 1039 (1998), and references therein.

- [154] J. G. Bednorz, in *Proceedings of the 5th Int'l Conf. on Materials and Mechanisms of Superconductivity, High-Temperature Superconductors, Beijing, China, 1997*, Physica C **282-287**, 37 (1997), and references therein.
- [155] J. P. Goral and J. E. Greedan, J. Magn. Magn. Mater. **37**, 315 (1983).
- [156] J. M. Tranquada, A. H. Moudden, A. I. Goldman, P. Zolliker, D. E. Cox, G. Shirane, S. K. Sinha, D. Vaknin, D. C. Johnston, M. S. Alvarez, A. J. Jacobson, J. T. Lewandowski, and J. M. Newsam, Phys. Rev. B **38**, 2477 (1988).
- [157] A strongly reduced spectroscopic splitting factor  $g$  is common to  $\text{Ti}^{3+}$  compounds.  $\text{Ti}^{3+}$  has been studied by electron paramagnetic resonance thoroughly in alum lattices. Typically,  $g$  values of  $\sim 1$  are found. See, for example, R. L. Carlin, *Magnetochemistry* (Springer, Berlin, 1986), and references therein.
- [158] D. A. Crandles, T. Timusk, J. D. Garrett, and J. E. Greedan, Physica C **201**, 407 (1992).
- [159] D. Vaknin, S. K. Sinha, D. E. Moncton, D. C. Johnston, J. M. Newsam, C. R. Safinya, and H. E. King, Jr., Phys. Rev. Lett. **58**, 2802 (1987).
- [160] A. Aharony, R. J. Birgeneau, A. Coniglio, M. A. Karstner, and H. E. Stanley, Phys. Rev. Lett. **60**, 1330 (1988).

## Curriculum Vitae

Name Gerhard Ingmar MEIJER  
Date of Birth 26th September 1972  
Nationality The Netherlands

1978 — 1984

Primary school in Hoogezand, the Netherlands.

1984 — 1990

High school Dr. Aletta Jacobs in Hoogezand, the Netherlands.

1990 — 1995

University of Groningen, the Netherlands.

Degree in Applied Physics (*cum laude*) on *Magneto-Transport and Point-contact Measurements in InAs-AlSb Quantumwells*; Supervisors: Prof. Dr. Ir. T. M. Klapwijk and Dr. Ir. B. J. van Wees.

Kamerlingh-Onnes Prize 1996, University of Groningen.

1994

Summer student at IBM Research Division, Zurich Research Laboratory. High-Speed Network Technology; Supervisor: Dr. A. P. J. Engbersen.

1995 — 1999

Swiss Federal Institute of Technology Zurich (ETH), Laboratory for Solid State Physics and IBM Research Division, Zurich Research Laboratory.

Thesis on *Magnetic Correlations in the One-Dimensional Quantum Magnets  $Sr_{0.73}CuO_2$  and  $Ca_{0.83}CuO_2$  and the Mott-Hubbard System  $LaTiO_3$* ;

Examiner: Prof. Dr. P. Wachter. Co-examiners: Dr. C. Rossel, Dr. J. Karpinski, and Prof. Dr. A. Furrer.